NASA/CR—2005-213327

Damage Prediction Models for Advanced Materials and Composites

Ming Xie
AdTech Systems Research, Inc., Beavercreek, Ohio

Jalees Ahmad
Research Applications, Inc., Centerville, Ohio

January 2005

The NASA STI Program Office . . . in Profile

Since its founding, NASA has been dedicated to the advancement of aeronautics and space science. The NASA Scientific and Technical Information (STI) Program Office plays a key part in helping NASA maintain this important role.

The NASA STI Program Office is operated by Langley Research Center, the Lead Center for NASA's scientific and technical information. The NASA STI Program Office provides access to the NASA STI Database, the largest collection of aeronautical and space science STI in the world. The Program Office is also NASA's institutional mechanism for disseminating the results of its research and development activities. These results are published by NASA in the NASA STI Report Series, which includes the following report types:

- TECHNICAL PUBLICATION. Reports of completed research or a major significant phase of research that present the results of NASA programs and include extensive data or theoretical analysis. Includes compilations of significant scientific and technical data and information deemed to be of continuing reference value. NASA's counterpart of peer-reviewed formal professional papers but has less stringent limitations on manuscript length and extent of graphic presentations.

- TECHNICAL MEMORANDUM. Scientific and technical findings that are preliminary or of specialized interest, e.g., quick release reports, working papers, and bibliographies that contain minimal annotation. Does not contain extensive analysis.

- CONTRACTOR REPORT. Scientific and technical findings by NASA-sponsored contractors and grantees.

- CONFERENCE PUBLICATION. Collected papers from scientific and technical conferences, symposia, seminars, or other meetings sponsored or cosponsored by NASA.

- SPECIAL PUBLICATION. Scientific, technical, or historical information from NASA programs, projects, and missions, often concerned with subjects having substantial public interest.

- TECHNICAL TRANSLATION. English-language translations of foreign scientific and technical material pertinent to NASA's mission.

Specialized services that complement the STI Program Office's diverse offerings include creating custom thesauri, building customized databases, organizing and publishing research results . . . even providing videos.

For more information about the NASA STI Program Office, see the following:

- Access the NASA STI Program Home Page at ***http://www.sti.nasa.gov***

- E-mail your question via the Internet to help@sti.nasa.gov

- Fax your question to the NASA Access Help Desk at 301–621–0134

- Telephone the NASA Access Help Desk at 301–621–0390

- Write to:
  NASA Access Help Desk
  NASA Center for AeroSpace Information
  7121 Standard Drive
  Hanover, MD 21076

NASA/CR—2005-213327

Damage Prediction Models for Advanced Materials and Composites

Ming Xie
AdTech Systems Research, Inc., Beavercreek, Ohio

Jalees Ahmad
Research Applications, Inc., Centerville, Ohio

Prepared under Contract NAS3–27152

National Aeronautics and
Space Administration

Glenn Research Center

January 2005

Document History

This research was originally published internally as HSR058 in August 1997.

Note that at the time of writing, the NASA Lewis Research Center was undergoing a name change to the NASA John H. Glenn Research Center at Lewis Field. Both names may appear in this report.

Available from

NASA Center for Aerospace Information
7121 Standard Drive
Hanover, MD 21076

National Technical Information Service
5285 Port Royal Road
Springfield, VA 22100

Available electronically at http://gltrs.grc.nasa.gov

DAMAGE PREDICTION MODELS FOR ADVANCED MATERIALS AND COMPOSITES

1.0 INTRODUCTION

This report covers a three year performance period from November 1993 to November 1996. The research work in this report were sponsored by NASA Lewis Research Center, conducted under the direction of Dr. Joseph E. Grady who served as the program monitor.

During the first year effort, Dr. Jalees Ahmad of AdTech Systems Research Inc. was principal investigator. Dr. Ming Xie of AdTech assumed the role of principal investigator in the second and third years, while part of the program was subcontracted to Research Application Inc..

The objective of the present program was to study and establish deformation and damage prediction models for advanced materials and composites. Acoustic liner concepts has been developed by NASA, that is, using high temperature resistant acoustic tiles lining the surface of components such as the divergent flaps and nozzle side-walls. These tiles are expected to be fabricated using advanced ceramic composites, and require a dedicated effort to determine their optimum size and attachment concepts while meeting the low noise, low weight, and long life goals.

In this report, several approaches to this objective will be documented. The assessment and evaluation of various acoustic tile designs were conducted using three-dimensional finite element analysis, which included static analysis, thermal analysis and modal analysis of integral and non-integral tile design options. Various benchmark specimens for acoustic tile designs, including CMC integral T-joint and notched CMC plate, were tested in both room and elevated temperature environment. Various candidate ceramic matrix composite materials were used in the numerical modeling and experimental study.

The research effort in this program evolved from numerical modeling and concept design to a combined numerical analysis and experimental study. Many subjects associated with the design and performance of the acoustic tile in jet engine exhaust nozzle have been investigated. All the research work in this program will be summarized in the following. The assessment and evaluation of acoustic tile design will be presented first, followed by the analysis and testing of benchmark specimens.

2.0 ASSESSMENT AND EVALUATION OF ACOUSTIC TILE DESIGNS

This section contains the evaluation of design options for ceramic matrix composites (CMC) acoustic tile liner being considered by the NASA/Pratt&Whitney (P&W)/GEAE Integrated Product Development (IPD) team for the HSCT exhaust nozzle within the EPM program.

2.1 Static Load Analyses

In the initial phases of acoustic tile design activity, one of the IPD team's main concern was regarding tile integrity under the weight of a person standing on the tile. Therefore, the early part of AdTech effort on acoustic tile design evaluation was conducted with the primary purpose of ensuring tile structural integrity under the static load caused by a 250 pound person standing on the tile at room temperature. This work involved a series of three dimensional finite element stress analysis of both an integral and a non-integral initial tile designs (both with egg crate cores) provided to AdTech by NASA. Additionally, analyses were performed to determine critical buckling load of the egg crate walls. In these early analyses nominal 2-D oxide-oxide CMC mechanical properties were used and both the face sheet and egg crate wall thickness were taken to be 0.09 inch. The 250 pound weight was uniformly distributed over a 3.5 "x 3.5 " surface area of the face sheet to simulate a person supporting all his/her weight on one shoe heel.

Based on the static load analyses, the IPD team concluded that both the integral and non-integral tile designs with egg crate cores would be able to withstand the static weight of a 250 pound person. The results provided in Figures 1 to 3 support this conclusion. At this point, NASA directed AdTech to perform a preliminary evaluation of thermal stresses. This activity is discussed next.

2.2 Preliminary Thermal Analyses

AdTech was assigned the responsibility of performing a preliminary assessment of thermal stresses in both integral and non-integral tile designs (both with egg crate cores) when subjected to a global thermal gradient. For this preliminary assessment, AdTech was directed to consider the face sheet temperature of 1800 F and (metallic) substructure temperature to be 1000 F. Again, due to lack of actual data at that time, nominal CMC and metal substructure properties were provided to AdTech by NASA.

The work involved a series of three dimensional finite element analyses of both integral and non-integral tile designs (both with egg crate cores) and with a variety of attachment types (boundary conditions). The purpose was to obtain estimates of global thermal stresses (not considering the details of actual thermal gradients, attachment design details, and the T or + shaped joint details between face sheet and egg-crate walls), mainly due to thermal property mismatch between face sheet and core, and between the tile and the

metallic substructure. Several fixed and sliding contact boundary conditions were investigated to simulate the various tile-substructure attachment types suggested by the IPD team.

The main conclusion based on the preliminary thermal analysis effort was that the use of only fixed tile-substructure attachments causes excessive thermal stresses and, therefore, should be dropped from further consideration. Based on this conclusion, a recommendation was made by NASA to the IPD team to develop alternative attachment concepts. The results provided in Figure 4 support these conclusions. At this point in time, based on IPD team discussions, NASA requested AdTech to focus on the following two issues which were considered critical at that time:

(a) detailed thermal stress analysis of the T shaped and + shaped connections between the face sheet and a stiffening rib and between face sheet and the egg crate, respectively, and
(b) modal and additional global thermal stress analyses of integral and non-integral tiles with various boundary conditions.

AdTech activities addressing (a) and (b) are summarized next.

2.3 Detailed Thermal Analysis of the Face Sheet-Rib/Egg Crate Connection

The desire for detailed thermal stress analyses of the T shaped and + shaped connections was instigated by the fact that past work by P&W for NASP had shown the critical failure location to be within these types of connections, and primarily due to Interlaminar stresses.

In preparation for these type of analyses, AdTech generated detailed three-dimensional finite element meshes designed to perform parametric study of joint stresses by varying the T-section radius, face sheet and egg crate wall thickness, the tile materials, and thermal gradients across the tile thickness.

The IPD team subsequently decided not to pursue these analyses at that time. Instead, it was decided that an investigation of the fundamental frequency of vibration of the tile was of more urgent importance.

The finite element mesh generated as part of this activity is available for future use. Detailed thermal analysis of the face sheet-rib/egg crate connection will, of course, be needed at some point in the tile design evaluation effort.

2.4 Modal and Thermal Stress Analyses of Various Tile Design Options

The IPD team recommended that in order for the tile to properly perform its acoustic attenuation function, its first fundamental frequency had to be larger than approximately

5 kHz. (Some other higher estimates of the minimum required frequency were also offered. But, as discussed later in this report, the actual number turned out to be inconsequential). Consequently, NASA requested AdTech to perform a series of modal analyses of integral tiles with egg crate core, non-integral tiles with egg crate core, and non-integral tiles with rib stiffened face sheet-- each with a variety of boundary conditions, overall tile dimensions, and for a wide range of material properties ranging from low modulus oxide/oxide CMCs to relatively high modulus SiC-SiC CMCs.

The work was performed using a series of three dimensional finite element analyses and, where feasible, using the Ritz method. The main finding after this series of extensive computational effort was that none of the design options (tile types, sizes, wall thickness, materials, and boundary condition combinations) satisfied the minimum 5 kHz frequency requirement. All options were found to have first fundamental frequency at least an order of magnitude lower than required. Local analyses of individual egg crate cells showed that the first fundamental frequency of the face sheet itself was orders of magnitude higher than the 5 kHz requirement. But this secondary vibration was considered less significant by the IPD team.

The discouraging result that none of the tile design options could meet the minimum frequency criterion was later found to be inconsequential. After receiving new information from acoustic experts in the Contractor Team, the IPD team decided that there is no minimum frequency requirement. Instead, what was decided to be relevant is the tiles' structural integrity under acoustic fatigue loading.

While later considered to be inconsequential, the extensive computational effort performed by AdTech under this activity of modal analyses of various tile design options resulted in the conclusion that none of the design options which were evaluated (tile types, sizes, wall thickness, materials, and boundary condition combinations) satisfied the minimum 5 kHz frequency requirement. Some of the key results are provided in Figures 5 to 7 and Tables 2 to 3.

The additional thermal stress analyses performed during this activity were similar to those performed in the activity described in Section 2.3 except that in the present activity, more realistic thermal gradients (supplied by P&W) and mechanical properties (provided by GEAE and P&W) were used. The results of a series of three-dimensional finite element analyses again showed the need for a sliding attachment scheme. Furthermore, being based on more realistic thermal gradient information and material properties, the results played an important role in the material down selection by the IPD team. Specifically, the results (plotted as stress/strength ratio) for a wide range of materials were used by NASA and other IPD members as part of the information based on which the number of candidate ti4e materials was reduced from thirteen (seven 2-D & six 3-D weaves) down to seven (four 2-D & three 3-D weaves). Some of the key results are given in Figures 8 to 9.

Towards the end of the period over which this modal analysis effort was performed, P&W (Dr. Ramon Mayor) developed a plan for further work in acoustic tile design evaluation. Essentially, this plan was developed in response to the NASA recommendation to the IPD team based on the conclusions discussed earlier under Section 2.2. The details of this plan and AdTech's work since then are discussed in the next section.

2.5 Further Analysis Plan

The two basically different CMC tile types considered in the CMC acoustic tile design evaluation plan provided to AdTech are:

(a) tiles with integral face sheet and egg crate; and (b) tiles with separate (non-integral) rib stiffened face sheet with inserts.

Figure 10 shows the various 'design concepts' developed by the HSCT Contractor Team - mainly within the integral tile category, but also some with non-integral core. Note that concept H involves both integral and non-integral core cases.

As seen in Figure 10, the 'concepts' primarily refer to the location of attachment locations. Out of the concepts shown in Figure 10, NASA selected concepts B, C, D, and H1 (concept H with integral egg crate) for initial analyses by AdTech.

Initially, the twelve different CMC material systems shown in Table 4 were proposed by the Contractor Team. as candidates for tile fabrication. AdTech was given the responsibility to perform the necessary analyses whose results would be used by the IPD team to:

(a) down select from the large number of proposed possible boundary condition combinations within each concept to a smaller set based on thermal stress analysis;

(b) rank tile types and concepts on the basis of fundamental frequencies of vibration (Initially the primary criterion for rejecting tile types and concepts proposed by the Contractor Team was 5 kHz minimum frequency);

(c) down select material systems from the initial list in Table 4 to four (two 3-D and two 2-D weaves) based on relative stress to strength ratios;

(d) down select from the initially proposed eight design concepts for integral tile to a single concept based on stress, acoustic fatigue life and weight considerations; and

(e) select the design concepts within each design type for detailed optimization, attachment design and material selection.

2.6 Summary of Analysis Results

In interpreting the results presented in this section it is important to emphasize the following comments and assumptions made in the analyses:

(1) The analyses were performed with the goal of obtaining global stress and deformation estimates rather than performing a detailed stress analysis of any particular tile design. The objective was to obtain a relative assessment of the various design options and attachment types. A detailed analysis would be performed later once concepts and materials have been down selected to a more manageable number of combinations. It is expected that a detailed analysis, which would include such details as the T or + shaped connections between the face sheet and egg crate, would give more accurate and higher stress estimates than those obtained in the present global analyses.

(2) Consistent with the goal of obtaining global estimates, the finite element analyses were performed using smeared composite face sheet and egg crate properties. Thus, the 3-D brick finite element model contained the following three material regions: Face sheet, egg crate, and metal (back structure). The model allows relative displacement between the tile and the back structure through the use of contact elements in ABAQUS finite element code.

(3) It was assumed (based on previous studies at P&W) that there is negligible pressure differential between top and bottom of the tile. The main effect of the pressure is to bend the back structure. Therefore, the effect of pressure can be modeled by applying a given displacement to the metal back structure. The difficulty of not presently having a definitive back structure deflection estimate was circumvented by applying a 1.0 inch (unit) deflection per 100 inch of back structure length. Since the analyses are more or less linear (except for the possible effect of nonlinear contact between tile and back structure). These unit displacement solutions can be later scaled to correspond to the actual back structure deflections once those estimates become available. However, it is expected that overall 1.0 inch per 100 inch deflection is not unrealistic.

(4) Thermal stress analyses were performed by imposing a thermal gradient across the tile height and back structure based on estimates provided by P&W. Again, consistent with the goal of obtaining global stress estimates, local temperature variations through the face sheet and egg crate cell wall were ignored. Instead a global thermal gradient shown in Figure 11 was used.

(5) CMC ply properties were assumed to be linear elastic and orthotropic. The material properties were provided by GEAE and P&W. These properties were updated several times during the course of the present work. With NASA's concurrence, analyses were performed always using the latest update, but not repeating previously completed

analyses. Since the updated properties were usually not drastically different than previous estimates, this aspect may not be very significant in interpreting the present global stress analysis results.

(6) The three concepts thus far included in the analyses have various attachment arrangements. In the finite element analyses, the boundary conditions were applied at appropriately located nodes at the interface of the tile and the back structure.

2.6.1 Stresses Due to Back Structure Deflection

The finite element analysis results given in Figures 12 to 22 show that the maximum stress values due to applied back structure deflection in concepts B and D are essentially the same. This occurs because in both cases the tile and the back structure stay in contact and, therefore, the central attachment in concept D does not have much effect on the deformation profile of the tile. In all concepts, face sheet thickness has significant effect on maximum stress, but doubling the thickness from 0.07 inch to 0. 15 inch does not quite reduce the maximum stress to half its value at the smaller thickness. The Maximum stress in concept C is approximately half of the corresponding value for concepts B and D. The egg crate wall thickness (varied from 0.03 to 0.08 inch) has insignificant effect on maximum stress as indicated in Figure 21.

The maximum stress values in all cases rise sharply as tile length L increase beyond 12 inches to 20 inches for all tile widths (W). The width W has minimal effect on the maximum stress magnitude.

Changing from type 1 boundary conditions to type 2 boundary conditions has minimal effect on maximum stress magnitude as indicated in Figure 22.

The above observations approximately hold true throughout the tile size ranges (W=6 to 48 inches and L=6 to 60 inches) and face sheet thickness range (tf = 0.07 to o. 15 inch) considered in the analyses of concepts B, C and D for the SiC/SiC material (BFG 3-D) material. There is no reason to expect that the observations will not hold true for other material systems as well.

Based on previous analysis results it can be expected that analysis of concept HI (see Figure 10) under back structure deflection loading will yield maximum stress values higher than or comparable to concept B because of higher constraint along the edges. Moreover, in actual nozzle, the back structure will deflect in both x and z directions. This fact will make the use of concept HI extremely difficult.

Overall, the maximum stress due to back structure deflection is the lowest in concept C (approximately half of the corresponding values in concepts B and D; all else being the

same). Also, egg crate wall thickness and attachment have minimal effect on global stresses and displacements.

2.6.2 Stresses Due to Thermal Loading

The finite element analysis results given in Figures 23 to 36 show that the maximum stress values due to transient thermal loading at take off in concepts B, C and D are not significantly different from each other. In all concepts, face sheet thickness has a much less significant effect on maximum stress than in the back structure loading cases. The egg crate wall thickness (varied from 0.03 to 0.08 inch) has insignificant effect on maximum stress as indicated in Figure 35. But this trend may be a consequence of using a global rather than a more precise thermal gradient as input.

The maximum stress values in all cases do not rise as sharply as in the applied back structure deflection cases. Recall that the prescribed temperatures in the tile do not vary in the plane of the tile. The width (W) has some effect on the maximum stress magnitude, especially for concept D for which maximum stress rises significantly with increasing W. The maximum displacement in z direction (δz) increases sharply with overall tile dimensions, but its magnitude remains small (<0.08 inch) within the parameter ranges considered in the analyses

Changing from type I boundary conditions to type 2 boundary conditions has minimal effect on maximum stress magnitude as indicated in Figure 36.

The above observations approximately hold true throughout the tile size ranges (W=6 to 48 inches and L=6 to 60 inches) and face sheet thickness range (tf = 0.07 to o. 15 inch) considered in the analyses of concepts B, C and D of row (i) of Figure 44 for the SiC/SiC material (BFG 3-D) material.

Based on previous analysis results it can be expected that analysis of concept H I (see Figure 10) under thermal loading will yield maximum stress values higher than or comparable to concept B because of higher constraint along the edges. Moreover, in actual nozzle, the back structure will deflect in both x and z directions. This fact will make the use of concept HI extremely difficult.

Overall, the maximum stress due to thermal loading is the highest in concept D. The maximum stress values in concepts B and C are comparable, with concept B being somewhat lower especially for larger tile size. The maximum in-plane file displacement is small for all concepts. Also, egg crate wall thickness and attachment have minimal effect on global stress and displacements.

2.7 Conclusions and Recommendations

In service, the acoustic tile finer will be subjected to combined thermal and pressure loading. Because, the individual thermal and pressure loading analyses presented in the two previous sections involved nonlinear contact between the tile and the back structure, strictly speaking the results cannot be superposed to obtain stresses due to combined pressure and thermal loading. However, in the spirit of obtaining global estimates for the purpose of ranking design concepts, it is considered acceptable to employ simple superposition of results. Then, based on the results presented in Section 2.6, it is found that under combined thermal and pressure loading, concept C generally gives the lowest combined maximum stress

Using 50% of the ultimate tensile strength (UTS) as the allowable stress, the concept C tile size may need to be restricted to less than 15" x 15"; unless more detailed analyses with combined thermal and pressure loads indicates otherwise. This recommendation on approximate maximum size takes into account the fact that the tile will be subjected to back structure deflection along as well as across the nozzle axis.

Thus, based on the current results, it is recommended that future work should mainly focus on more detailed analyses of concept C only. These analyses should include: (a) parametric studies in which, tile size, distance between attachments and face sheet wall thickness are varied, and (b) combined pressure and thermal loading.

Guided by the results presented in Section 2.6, AdTech took the initiative of exploring a new tile design concept not included in the original plan (Figure 10). This new concept is schematically shown in Figure 37.

As shown in the top sketch in Figure 37, the new concept contains only one attachment point at the tile center which constrains all translation and rotation degrees of freedom. This can be accomplished, for example, by using a bolt with an X shaped or elliptical cross-section. The use of a single attachment can potentially reduce total weight compared to the use of two OF more attachments. Furthermore, it has the potential of reducing both the thermal and the pressure loading stresses. The likelihood of high stresses close to the attachment location are addressed by potentially using a larger egg crate wall thickness across the attachment location. The other egg crate walls can be made thinner to compensate for the additional weight of the thicker walls. The thicker wall and the face sheet are envisioned to be integral with 3-D weave. Depending upon results of more detailed analyses, the rest of the egg crate may or may not be integral to the face sheet.

The fundamental frequency of vibration of the new concept tile will be somewhat less than for a comparably sized tile with two or more attachments. It is not clear if this is going to be of concern. The frequency of the face sheet itself (with integral egg crate) will, of course, remain unchanged compared to the other design concepts. Also, a single attachment may result in large in-plane displacements which may be of concern as there

may be larger than acceptable gaps between tiles at lower temperatures. As shown in the bottom sketch of Figure 37, this concern can be addressed by having 'lips' extending from the sides of the tiles. By proper design, these lips from neighboring tiles can be made to overlap to prevent any gaps between tiles.

2.7.1 Preliminary Analysis of the New Tile Design Concept

Figures 38 to 39 show preliminary results of finite element analyses of the new tile design concepts. In these preliminary analyses, the egg crate and the face sheet were taken to be integral everywhere and the egg-crate wall thickness was kept uniform at 0.05 inch (i.e. thicker walls were not used across the attachment as depicted in Figure 10). Analyses were performed under the same back structure deflection and thermal conditions as those used in analyzing the other design concepts.

As shown in Figure 38, the global stress due to back structure deflection in the new concept is almost zero. The thermally induced maximum stress shown in Figure 39 is somewhat lower bill in the same range as for the concept C tile analyzed. Furthermore, there is no significant dependence of maximum stress on tile size. Therefore, it may be possible to use larger tile sizes.

Based on these preliminary results corresponding to the new tile design concept, it is recommended that further detailed evaluation of the concept be performed.

2.7.2 Acoustic Fatigue Consideration

Acoustic fatigue analyses will require at least two new finite element models (one each for non-integral and integral tile designs) of the face plate-cell wall (or rib) assembly. These would then be subjected to modal analyses (to obtain at least the first three fundamental frequencies and mode shapes) and stress analyses to generate 'unit pressure' solutions for each mode shape. These finite element solutions for each material system would then be used to generate the Goodman-Miles diagrams. Based on P&W's (Mr. Bob Miller and Mr. Bob Warburton) experience in the NASP program, it may be prudent to commence the acoustic fatigue analyses as early as possible.

3.0 EXPERIMENTAL STUDY OF CMC INTEGRAL T-JOINTS

The noise reduction is a major concern in the design of engine exhaust nozzle. Acoustic treatment of exhaust nozzle is usually required by attaching a layer of acoustic liner on the nozzle sidewalls. The so-called integral design uses a honeycomb structure which is integrally attached to a facesheet and sidewalls. The honeycomb structure provides a precisely sized cavity for the noise reduction mechanism. The baseline nonintegral design for the acoustic tile, however, is a multi-rib stiffened open box with the open end facing away from the flow path. The closed end of the box is flat and forms the flow path

surface which is perforated with small holes that allow sound waves to penetrate into the box. The acoustic absorbing material inside the box then reduces the acoustic emission. The T-shaped joints, as shown in Figure 40, serve as the attachment feature of this nonintegral design and can be slid into a metallic C-shaped track on the nozzle sidewall. The C-shape track allows the rotation of the T-joints about the track axis but does not allow movement transverse to the track. This nonintegral design reduces the thermal stresses due to the over constraint in integral design and also reduces the fabrication and assembly efforts.

In the present study, four ceramic matrix composite materials, as listed in Table 5, were considered for this T-joint design. All the materials were woven fiber reinforced ceramic matrix composite with either two-dimensional or three-dimensional fiber woven patterns. The dimensions of these T-shaped specimens are illustrated in Figure 40. For both B. F. Goodrich 3D SiC/SiC composite and Pratt&Whitney 3D Oxide/Oxide composite, there was only a very small radius at the joint of the web and flange sections of the T specimen. For B. F. Goodrich 2D SiC/SiC composite, the radius at the joint was about 0.2". For GE/Hexcel 2D Oxide/Oxide composite, two sets of specimens were fabricated with two different radii at the joint, one set with a 0.25" radius and another set with a 0.125" radius.

3.1 Tensile-Flexural Test of CMC T-Joints

A fixture was designed and fabricated in the present study to apply the load to the specimen. As shown in Figure 41, the flange of the specimen rests on two supporting pins, while the tensile load is applied to the web section by the hydraulic grip of a MTS test frame. It can be seen that this three-point loading tensile-flexural test is similar to the three-point short beam bending test. The distance between the two supporting pins can be adjusted. However, a span of 2.75" was used in the present study for all the T specimens. The loading speed of the test frame was 0.05in/min. A 5,000 lbs load cell calibrated to 250 lbs full range was utilized.

A swivel joint was used between the bolt and the platform, as shown in Figure 41. In the original fixture, the bolt was connected to the platform directly. However, significant bending of the web section of the T specimen was observed. The swivel joint was utilized to minimize the bending effect.

In the present study, a real time viewing and recording system was set up, as shown in Figure 41, besides the data acquisition system. Through a microscope and a video camera, the whole process of crack propagation and failure of a T-joint can be viewed on a TV monitor in real time. The image can be recorded on video tape in a video cassette recorder (VCR) and be played back later. Still photo can be taken using a special camera through the microscope. Any frame of the video recording can also be printed directly from the video tape by using a video printer.

As mentioned above, four composite materials were investigated in the present study. Three (3) T specimens were tested for each material except that a total of six (6) specimens for GE material with two different radii at the joint. The average failure loads for the T-joints are also listed in Table 6.

It can be seen that SiC/SiC composite T-joints had a higher strength than Oxide/Oxide composite T-joints. The strength of the Pratt&Whitney 3D Oxide/Oxide composite T-joints was the lowest. The GE/Hexcel 2D specimens with a larger radius yielded only a slightly higher failure load than those with a smaller radius. It should be noted that the use of the swivel joint between the bolt and the platform, although reducing the bending at the web section, appears to have no significant effect on the failure load.

3.2 Strain Analysis of T-Joints

A total of six (6) strain gages were placed on one T specimen, as shown in Figure 41, in the middle of the width direction. All the gages were placed symmetrically with respect to the center of the Joint. Since the specimens have different radii at the joint, the strain gages were placed as close to the joint as possible, but not on the fillet.

A set of typical strain curves for an Oxide/Oxide 3D T specimen are presented in Figure 42. This Oxide/Oxide 3D T specimen was tested on the fixture without the swivel joint. Since the fixture did not allow any transverse rigid body motion, the initial misalignment of the specimen or the fixture could cause significant bending of the web section. In fact, only right section of the flange was loaded at the very beginning because of the initial misalignment. This can be seen clearly in 42(a) and 42(b), since strain data from gages 5 and 6 show that left section of the flange did not carry any load at the beginning. Therefore, the web section and right section of the flange were forced to open as loaded. Strain gage 3 thus read positive (tensile) strain while gage 4 read negative (compressive) strain. However, after left section of the flange began to carry load, the bending of the web section was released. The strain curves in Figure 42(c) started to change trend when strain gages 5 and 6 started reading strain data at about the same time.

At a load of about 4.5 lbs, the specimen initialized failure at a location in the middle of the joint and the right support. In Figures 42(a) and 42(b), strains from gages 1 and 2 did not increase further because of the failure. Now the load was carried mainly by left section of the flange. The strains at gage 5 and 6 continued to increase. At the same time the web section was further bent to right side and this is obvious in Figure 42(c). The specimen continued to be loaded until about 5.5 lbs. Strain data indicated that unloading started and the T-joint specimen was then considered to be of complete failure.

Another set of typical strain curves are presented for a SiC/SiC 3D composite T specimen in Figure 43. It should be noted, though, that the swivel joint was used for this

specimen. As can be seen in Figure 43(c), the initial bending of the web section was greatly reduced compared to the previous example, considering that the load applied to this specimen was much higher. The tensile strains outputted from gages 3 and 4 were also low because of the relatively high material stiffness. At a load of about 23 lbs, failure started at the tensile side of the right section of the flange as indicated by the strain data from gage 2 in Figure 43(b). The load was then carried by left section of the flange and the web section was bent slightly to the right. Strain gage 3 thus read negative (compressive) strain and strain gage 4 read positive (tensile) strain. The failure of this SiC/SiC 3D specimen was more brittle than the Oxide/Oxide 3D specimen shown in the previous example. The photo for this failed specimen and the examination of its failure mode will be presented in the next section.

A set of typical load versus strain curves for a SiC/SiC 2D T specimen are shown in Figure 44. It can be seen from Figures 44(c) that both the strain gages 3 and 4 on the web section of the joint yielded negative strains. This was not expected since a tensile load was applied to the web section. The compression at these two strain gage locations were observed for all the SiC/SiC 2D T specimens. For other T-joints, the strain gages at the web section all indicated bending, as in previous examples. Finite element modeling will be used to investigate and further explore the structural response of these SiC/SiC 2D T-joints. The numerical modeling results will be presented later.

3.3 Failure Modes of Various CMC Specimens

All the T specimens were examined under a microscope to inspect any material defect or initial crack. All the GE Oxide/Oxide 2D specimens were found to have smooth surfaces and no obvious defect. Both BFG SiC/SiC 3D and PW Oxide/Oxide 3D specimens were found to have small voids on the specimen surfaces due to the nature of 3D fiber woven pattern, the quality of PW specimens being slightly better than BFG 3D specimens.

However, BFG SiC/SiC 2D specimens had small see-through initial cracks at the joints. These initial defects could be seen even without the aid of a microscope. A closed-up photo of one SiC/SiC 2D composite T specimen is presented in Figure 45(a), showing an enlarged joint section. The cracks at the joint can be seen clearly in the photo. The failed specimen, being painted white to reveal the delamination, is also shown in Figure 45(b). As can be seen in the photos, delamination caused by the growth of the initial cracks was the main reason of specimen failure. There were also some other delaminations occurring at the joint as shown in Figure 45(b).

As mentioned before, a real time monitoring system was set up in the present study. The crack initialization and propagation in the T joint was able to be viewed and recorded either on video tape. As an example, the crack initialization and propagation at the joint of a Oxide/Oxide 2D T specimen, with a radius of 1/4", are shown in Figure 46. These

images were printed directly from the video tape recording using a video printer. The joint surface was painted black before testing to reveal any cracks since the material is white.

Frame 46(a) shows the joint without any crack present. In Frame 46(b), the delamination started from the flange section and propagated down the web section. The cracks occurred at both side of the joint with left side more obvious as shown in the photo. The cracks branched into the center of the joint in Frame 46(c) before the left crack traveled further down the web section of the joint in Frame 46(d). The right crack also propagated further along its original path into the web section in Frame 46(e). It is obvious that delamination is the main reason for the failure of the Oxide/Oxide 2D T-joint, same as the SiC/SiC 2D T-joint.

It should be noted that for the Frames 46(a) through 46(d), the position of the microscope was fixed. The deflection of the specimen can thus be seen from these frames. The position of the microscope was lowered in Frame 46(e) to record the crack propagating down the web section of the T-joint specimen.

For 3D woven fiber reinforced composite T-joint, the failure mode was an obvious bending failure on the tensile side of the flange. In Figure 47, a SiC/SiC 3D composite specimen was shown, for both before and after the test. The specimen surface was painted white before testing to reveal any new cracks. The surface of the three-dimensional woven fiber reinforced specimen was rough, even with some small notches, as can be seen in this enlarged photo. It can be seen from Figure 47(b) that a vertical crack, starting from the tensile side of the right flange, occurred at a location close to the joint. These images were printed directly from the video tape recording using a video printer. The strain data for this specimen have been presented in Figure 43 in the previous section.

For Oxide/Oxide 3D T-joints, the bending failure occurred at a location in the middle of the joint and the support. There was no obvious crack due to more compliant nature of the material.

3.4 Conclusions for Experimental Study of Integral T-Joints

In the present study, four candidate ceramic matrix composite materials were investigated for the nonintegral design of acoustic tile of nozzle sidewall. The T-joint, designed to attach the acoustic tile to the nozzle sidewall through a C-shaped track, was tested under a tensile-flexural loading. The SiC/SiC composite joints yielded higher failure load than those made from Oxide/Oxide composites. Two distinct failure modes were observed. The composite T-joints with 2D fiber architecture failed due to delamination starting from the joint, while the T-joints with 3D fiber architecture had a bending failure at the tensile side of the flange.

Many other factors besides the structural strength have to be considered in the material screening process and acoustic tile design. The present study, in which static tensile-flexural test on T-joint was performed under room temperature, only constitutes a very small part of this process.

4.0 EXPERIMENTAL STUDY OF NOTCHED CMC PLATES

Three ceramic matrix composite materials were investigated in the present study. They are BFG SiC/SiC 3D composite, GE Oxide/Oxide 2D composite and Pratt&Whitney Oxide/Oxide 3D composite. All the materials are woven fiber reinforced ceramic matrix composite with either three-dimensional or two-dimensional fiber woven patterns, as listed in Table 5.

Both static and fatigue tests were performed under room temperature (75°F) and elevated temperature (1650°F). X-ray radiography was conducted on some coupon specimens to detect the damage at the hole region.

All the coupon specimens in the present study have the same nominal dimensions, i.e., 6.0 inch long and 1.25 inch wide with a thickness of 0.1 inch. All the coupons have a 0.25 inch diameter hole in the center.

4.1 Static Tensile Test Under Room and Elevated Temperatures

Static tensile test was performed on a total of fifteen (15) specimens. The average failure loads are listed in Table 7, for both room temperature and elevated temperature.

The surfaces of SiC/SiC-3D composite specimens have many small bumps, probably due to the manufacturing process. The stress concentration at these small bumps caused one specimen failed inside the grips. A layer of epoxy was then applied to the ends of two specimens to make the surface smooth. However, they still failed inside the grips. The failure load at room temperature averaged from these three specimens thus has a very low value, as listed in Table 7. A very fine diamond grinder was then utilized to grind the end surface of all the remaining SiC/SiC-3D specimens and to smooth out the bumps. All three specimen tested under elevated temperature failed at the hole and yielded fairly close strength after this treatment.

Three strain gages were placed on all specimens tested under room temperature except those for x-ray radiography. The strain gages were placed around the hole. Two extensometers were used on all specimens including those for x-ray radiography. For specimens tested under elevated temperature, no strain gages were applied and only two extensometers were used. An one-inch gage length extensometer was placed across the

hole, while a half-inch gage length extensometer was placed at the edge of the coupon. The locations of the strain gages and extensometers are shown in Figure 48.

Some typical load versus strain curves for static tensile test of notched CMC coupon are presented in the following. For example, the strains obtained from the three strain gages are shown in Figure 49 for an Oxide/Oxide-2D specimen and in Figure 50 for an Oxide/Oxide-3D specimen, respectively. It should be noted that, for the Oxide/Oxide-3D specimen, strain obtained from gage 3 is higher than that from both gages 1 and 2. Usually the strain obtained from strain gage 1 where the stress concentration exists is the highest, one example having been shown in Figure 49 for an Oxide/Oxide-2D specimen. This trend reversal is probably due to the fiber woven structure in the Oxide/Oxide-3D composite.

4.2 High Temperature Fatigue Test

A total of six (6) notched CMC coupon specimens were tested under fatigue loading at 1650°F, as presented in Table 8. The loading was tensile-tensile with R=0.1. The specimen was loaded at a low frequency of 10 cycles per minute (0.167 Hz) up to 10,000 cycles. Then the frequency was increased to 30 Hz and the test continued. The maximum load was about 60% of the static failure load as reported in the previous section. Two extensometers were used to measure the strain in the specimen. A one-inch gage length extensometer was placed across the hole while a half-inch one being placed at the edge of the coupon, as shown in Figure 48.

The load versus strain curves for an Oxide/Oxide-2D composite specimen are presented in Figure 51 for different cycles, strain being obtained from one-inch gage length extensometer. There is no significant change in stiffness as shown in the figure.

For Oxide/Oxide-3D composite specimen, the damage and stiffness change can be seen clearly in Figure 52, which shows the load versus strain obtained from the one-inch gage length extensometer. At the first loading cycle, there was a large residual strain. Comparing the curves for cycle 5100 and cycle 9600, there was a noticeable change in material stiffness. It should be noted that in the same cycle the stiffness also increased when load increased. This is probably because the fibers carried most of the load after the cracks saturated in the matrix. When the load was applied to the specimen, the fiber reoriented to the loading direction and therefore the apparent modulus of the specimen increased.

For SiC/SiC-3D composite, the fatigue behavior is similar to that of Oxide/Oxide-2D composite. No significant change in stiffness was noticed.

In the present high temperature fatigue testing, the conventional hydraulic grips were used, only the center portion of the specimen being put inside the furnace. The effect of the temperature gradient in the specimen on the fatigue strength can be investigated by

using a pair of specially designed grips which can be put inside a larger furnace together with the specimen. The specimens will thus have more uniform temperature distribution compared to the specimens with hydraulic grips.

4.3 X-ray Radiography of Notched CMC Plates

Damage modes such as delamination and matrix crack can be detected by penetrant enhanced x-ray radiography. A zinc-iodide solution (60 gm zinc-iodide powder, 15 ml isopropyl alcohol and 15 ml water) was used in the present study as an x-ray opaque penetrant. This penetrant was applied over the surface at the hole region and seeped into the damaged areas. Excess penetrant was removed from the surface with acetone prior to exposure to the x-ray. The damage in five (5) specimens, one from each group, in different loading levels was monitored using penetrant enhanced x-ray radiography. The technique was applied to the specimen before applying any load to detect initial defect and damage. Then the specimen was loaded to a certain level, unloaded and the penetrant enhanced x-ray radiography was applied. Two different loads were applied before the specimen was loaded to the final failure.

As an example, the load versus strain curves for an Oxide/Oxide-3D specimen are shown in Figure 53. This specimen was loaded up to 300 lbs and then unloaded. After x-ray radiography, the specimen was loaded again to 500 lbs, then unloaded. Both strains obtained from one-inch and half-inch gage length extensometers are shown in the figures. It can be seen that there are significant residual strain at the hole region, where the one-inch gage length extensometer was placed, caused by the damage. The x-ray photos taken before any load was applied, and taken after the second loading, i.e., 500 lbs, are presented in Figure 54. The damage, as shown in the photos as white areas, accumulated after more load was applied.

There is one obvious limitation to the penetrant enhanced technique, that is, only damage that has paths open to the surface will be detected. In fact, the damage accumulations shown in x-ray photos for other specimens are not very clear and will not be presented here.

5.0 NUMERICAL MODELING OF CMC INTEGRAL T-JOINTS

Before experiment, all the specimens were examined under a microscope to inspect any initial defect. Some T-joints made from two-dimensional SiC/SiC fabric composite, which consists of ceramic grade Nicalon fiber with an interface coating, and a CVI SiC matrix, had small see-through cracks at the joints. These initial cracks could be seen even without the aid of a microscope. A closed-up photo of one such T-joint has been presented in Figure 45(a), showing an enlarged joint section. The cracks in the T-joint can be seen clearly in the photo. The failed specimen has also been shown in Figure 45(b), a layer of white painting being applied to the surface to reveal the new cracks in this black material.

As can be seen in the photos, the growth of the initial cracks was the main reason of the structural failure. There were also some other delaminations occurring at the joint, as shown in Figure 45(b). All the other T-joints were found to have no obvious defect.

A set of typical load versus strain curves for a T-joint with initial cracks have been shown in Figure 44. The locations of the strain gages 1 through 6 have been illustrated in Figure 41. It can be seen from Figures 44(a) and 44(b) that the bending of the flange section of the T-shaped joint is obvious, since initially the strain gages 1 and 6 on the top of the flange read negative strains while the strain gages 2 and 5 on the bottom of the flange read positive strains.

However, the strain gages 3 and 4 on the web section of the joint yielded negative strains, as shown in Figure 44(c). This was not expected since a tensile load was applied to the web section. The compression at these two strain gage locations were only observed for the T-joints with initial cracks. For other T-joints, the strain gages at the web section all produced tensile strain.

All SiC/SiC 2D T-joints yielded compressive strains at the web section which was subjected to tensile loading while this was not observed for any other T-joints. This was probably due to the initial defect at the joint section of these SiC/SiC 2D T-joints. A three-dimensional finite element analysis was performed in the present study to predict and further understand the stress-strain response of the imperfect T-joint.

The triangular web-flange transition area of these SiC/SiC 2D T-joints was filled with the same SiC/SiC unidirectional composite, its fiber direction being the same as the width direction as shown in Figure 45(a). Both the laminated and unidirectional composite material properties are listed in the following, the unidirectional composite properties being calculated using laminate theory assuming a $[0/90]_S$ lay-up in the laminate. For laminated composite,

$$E_{11} = E_{22} = 14.1 \text{ Msi}, E_{33} = 6.0 \text{ Msi},$$
$$\nu_{12} = 0.15, \nu_{13} = \nu_{23} = 0.22$$
$$G_{12} = 10.0 \text{ Msi}, G_{13} = G_{23} = 5.8 \text{ Msi}$$

For unidirectional composite,

$$E_{11} = 22.2 \text{ Msi}, E_{22} = E_{33} = 6.0 \text{ Msi},$$
$$\nu_{12} = \nu_{13} = \nu_{23} = 0.35$$
$$G_{12} = G_{13} = 10.0 \text{ Msi}, G_{23} = 2.2 \text{ Msi}$$

A SiC/SiC 2D T-joint with perfect bonding at the web-flange transition area was modeled, as well as a SiC/SiC 2D T-joint without the fill-in unidirectional composite at the transition area. A T-joint without fill-in material was also modeled with the initial

delamination at the vertices of the transition area extending into the web and the flange section for another 0.1 inch. These three models would help to understand the behavior of real SiC/SiC 2D T-joints which had imperfect bonding at the transition area.

Only a quarter of the T-joint was modeled because of the symmetry. Twenty-node quadratic brick element in finite element software ABAQUS was utilized in the analysis. Five layers of element was used in the width direction of the T-joint and the variation of the stress distribution in the width direction was found later to be not significant. A total of 6180 nodes (1145 elements), 5620 nodes (1005 elements) and 5733 nodes (1005 elements) were used for T-joint with perfect bonding, T-joint without fill-in material, T-joint without fill-in material and with 0.1" extended cracks, respectively.

Figure 55 shows the strain distribution for a T-joint without fill-in material, along 2-direction of the local coordinate system, when a 0.05 inch vertical displacement was applied to the web section. It can be seen clearly that the outer surface of the web section at the joint region was subjected to compression where the strain gages 3 and 4 were placed. Similar results were obtained for the modeling of T-joint without fill-in material and with extended cracks. However, for a SiC/SiC 2D T-joint with fill-in material and a perfect bonding, positive strain was obtained at the same location. Therefore, it was concluded that the initial delamination at the joint section caused the different structural response between these imperfect SiC/SiC 2D specimens and other T-joint specimens.

When the SiC/SiC 2D T-joint was subjected to about 20 lbs load, the strain at gage 3 and 4 measured at the experiment was about -75×10^{-6}, as shown in Figure 44(c). The finite element models for T-joint with and without fill-in material predicted a strain of 21×10^{-6} and -599×10^{-6} at the same locations, respectively, for the same load level. For the model without the fill-in material and with 0.1" extended initial delamination, the predicted strain at these location was -163×10^{-6} and was more close to the measured value.

A typical curve for load versus vertical displacement obtained in the experiment for an imperfect SiC/SiC 2D T-joint is shown in Figure 56. The numerical predictions of the present finite element modeling are also presented. It can be seen that even the prediction for T-joint without fill-in material and with 0.1 inch extended cracks overestimated the stiffness of the T-joint. The reason for this overestimation is that the initial defect at the SiC/SiC 2D T-joint was much more severe, as evident in Figure 45(a), than that modeled in the present analysis.

In summary, although the present numerical modeling was able to correlate with the experimental data on tensile-flexural test of ceramics composite integral T-joints with initial defect, they were preliminary and qualitative. More in-depth finite element modeling of composite integral T-joints should be conducted to investigate their stress-strain responses and failure mechanisms.

6.0 NUMERICAL MODELING OF NOTCHED CMC PLATE

Three dimensional stress analysis in laminated composite plates containing open hole and subjected to unidirectional tension was performed. Two material systems were considered: GE/Hexel 2D Oxide/Oxide Gen 4 matrix/Nextel fiber and UTRC UT-22 2D. The laminates considered were: [0/90]s and [0/45/90/-45]s. Load levels of 200lb and 250lb were applied to these laminates respectively. Distributions of the hoop stress and interlaminar normal and shear stress around the hole edge are displayed. Contours of all stress components divided by their ultimate allowable values in a region surrounding the hole are presented.

6.1 Method of Analysis

Independent polynomial spline approximation of displacement and interlaminar tractions is utilized for stress analysis. Spline approximation eliminates the inter element compatibility problems leading to unsatisfactory finite element results in the presence of field singularities. Spline approximation offers continuity of displacement, strain and stress within homogeneous domains preserving at the same time the advantages of local approximation, such as sparcity of resulting system of equations. Special emphasis was placed on verification of the accuracy of interlaminar stress calculation. The results of interlaminar stress calculation were compared with closed form asymptotic solution developed by several researchers. Excellent agreement has been observed for interlaminar stresses in [45/-45]s composite containing a circular hole and subjected to tensile loading.

A rectangular laminated plate consisting of N-plies and having a through-the-thickness opening, shown in Figure 57, is considered. In x, y, z coordinates the contour of the plate is defined in parametric form as

$$x = \frac{d}{2}\cos\theta + x_c,\ y = \frac{d}{2}\sin\theta + y_c \tag{1}$$

where d- is the hole diameter and x_c and y_c - the hole center coordinates. q - is the polar angle measured from the x-direction. The center of the polar coordinate system r, q, z coincides with the center of the hole. The plate is of length L -in x-direction and width A in the y-direction. Displacement boundary conditions are applied at lateral edges x=0,L as follows

$$\begin{gathered} u_x(0,y,z) = -u_x(L,y,z) = \Delta \\ u_y(0,y,z) = u_y(L,y,z) = u_z(0,y,z) = u_z(L,y,z) = 0 \end{gathered} \tag{2}$$

$\Delta>0$ corresponds to tensile loading. The interlaminar surfaces between s and s+1 plies are denoted as $z = z^{(s)}$, where $z^{(0)} = 0$ and $z^{(N)} = H$ -thickness of the plate. The top and bottom surfaces, the lateral surfaces y=0, y=A and the hole edge are traction free. After the problem is solved, the uniaxial load can be calculated as

$$P = \int_0^H \int_0^A \sigma_{xx}(0,y,z)dydz \qquad (3)$$

The full field spline approximation solution is performed in curvilinear coordinates mapping the x,y plane onto ρ and ϕ plane where $0 \leq \rho \leq 1$ and $0 \leq \phi \leq 2\pi$. Spline approximation nodes are introduced along independent coordinates: $0 = \rho_1 < \rho_2 < ... \rho_m = 1$; $0 = \phi_1 < \phi_2 < ... < f\ \phi_k = 2\pi$; $z^{(s)} = z_1 < z_2 < ... < z_{ns} = z^{(s+1)}$. Sets of spline functions upon each coordinate are built and used for three-dimensional displacement approximation and for interlaminar stress approximation at the interfaces. To obtain the unknown coefficients of displacement and interlaminar stress spline approximation, the variational technique is used.

6.2 Plate Geometry and Material Properties

The geometric properties of the plates under investigation were L=6", A=1.25" and d=0.25" central circular hole. Figure 58 shows the coordinate lines of the curvilinear transformation for this geometry (solid lines are $\phi = \phi_i$, i=1,...,m lines and dashed lines are $\phi = \phi_i$, i-1,...,k lines). m=14 intervals were used in ρ-direction and k=24 were used in ϕ - direction.

Material properties used in computation are the unidirectional ply properties reduced from the [0/90]s coupon properties provided by sponsor. The material properties used are given in Table 1.

6.3 Numerical Results

In following analysis a half of the symmetric laminate was considered and each ply was subdivided into 2 sublayers (ns = 2). Plies were numbered starting from the mid-surface.

6.3.1 Laminate: [0/90]s; Material: GE/Hexel 2D Oxide/Oxide Gen 4 matrix/Nextel 610 Fibre

Applied load the edges x = 0,L was equal to 200 lb (applied stress - 8 ksi). The distribution of hoop stresses along the edge boundary at different locations through the thickness the laminate are shown in Figure 59. The stress concentration factor in 0° ply is around 11. Interlaminar normal σ_{zz} and shear $\sigma_{\theta z}$ stresses at the hole edge and 90/0 interface are shown in Figures 60 and 61 respectively. These graphs allow to assess the accuracy of analysis and character of interlaminar stress distribution. Transverse

Table 1. Material Properties Used in Calculations.

Property	Ge/Hexel 2D Oxide/Oxide Gen 4 matrix/Nextel 610 fibre	UTRC UT-22 2D
E11 (Msi) (fibre direction)	21.2	
E22 (Msi)	1.0	
E33 (Msi)	1.0	
G13 (Msi)	0.63	
G23 (Msi)	0.32	
G12 (Msi)	0.63	
U13	0.22	
U23	0.22	
U12	0.22	
Xt=Xc (Ksi)(fibre direction)	64	
Yt (Ksi) (matrix tension)	0.8	
Yc (Ksi)	---	
S (Ksi) (shear strength)	2	

interlaminar stresses have to be continuous at the interface. The largest discontinuity of the σ_{zz} stress at around q=70° is less than 10%. It was shown that this discontinuity reduces almost to zero immediately away from the hole surface. Accuracy of $\sigma_{\theta z}$ calculation is 2.5%. Negative sign of the interlaminar normal stresses almost at all locations makes delaminations very unlikely to appear at early stages of damage initiation.

Damage onset evaluation is performed by investigating all stress components at each interface, including mid-surface and top surface. Stresses were calculated in ply coordinates and divided by allowables given in Table 1. A semi-circular area $180°<\theta<360°$ $d/2<r<d/2+2H$ (H-laminate thickness) was considered.

Stresses at the surfaces were the largest values were observed are shown in Figures 62a, 62b, 63a, 63b and 64a and 64b. The highest stress to strength value 3.8 is shown by tensile matrix in-plane stresses on 62b. Due to linearity of the analysis the contour values can be proportionally reduced or increased to obtain stresses for other load amplitudes. So that to predict the onset of matrix cracking one may observe that even at 100lb load the tensile matrix stresses exceed the allowable - Yt in a region about half the laminate thickness long at around $\theta=90°$. At the applied load level, 200lb, the tensile stresses in 0° plies already exceed their allowables (Figure 62a). According to last ply failure concept this load is close to the failure load. Other stress components on Figures 63 and 64 have intermediate values.

6.3.2 Laminate: [0/45/90/-45]s; Material: GE/Hexel 2D Oxide/Oxide Gen 4 Matrix/Nextel 610 Fibre

Similar results are presented for the quasi-isotropic laminate. The applied load in this case is 250lb (5 Ksi). The distribution of the hoop stresses and interlaminar stresses at the hole edge are given in Figures 65, 66, 67. The major difference in interlaminar stress distribution between this and the cross-ply laminate is that the normal stress σ_{zz} between -45 and 90 plies becomes positive and introduces a possibility of delaminations at early stages.

The stress contours similar to those for cross-ply laminate are given in Figures 68, 69 and 70. Again the highest stress to strength value of 2.8 is shown by tensile matrix in-plane stresses on 68b. Thus the stresses appear in 45 ply at approximately 250° and 70° directions. At this location matrix cracks will initiate in 45-ply at approximately 250° and 70° directions. At this location matrix cracks will initiate in 45-ply. Since at the load of 250lb the region where Yt is exceeded extends approximately half the laminate thickness from the hole edge we conclude that at this load the matrix cracking is likely to appear. Similar high stress to strength ratio is observed in Figure 70a for interlaminar shear stress. However, the region were it is high is very narrow and unlikely produces delaminations at the 250lb load.

7.0 SUMMARY

Two major studies have been conducted in this performance period. The evaluation and assessment of ceramic matrix composite acoustic tile, including its design, thermal and acoustic load carrying capabilities, were performed using finite element analysis. Then benchmark testing on subelements of acoustic tile, including ceramic matrix composite integral T-joints and notched plates, were conducted to evaluate their performance in various thermal conditions. Numerical modeling was also utilized to analyze the stress-strain response of these benchmark specimens and the numerical results were correlated to the obtained experimental data.

In Enabling Propulsion Materials (EPM) Program and other NASA aircraft programs, many studies on composite materials, including ceramic matrix composites (CMC), metal matrix composites (MMC) and polymer matrix composites (PMC), have been performed on material design and structural durability. For example, one candidate CMC material for acoustic tile design has been identified recently after detailed analytical and experimental evaluations.

However, it is still very difficult to assess the long term durability of candidate materials and structural designs under simulated mechanical and environmental loading conditions. It requires significant amount of experimental effort, and at the same time, an efficient

analytical model to further interpret the obtained experimental data and predict the life of candidate materials and structures.

Experimental support to the analytical/numerical effort will be necessary because: (1) Experimental data may be needed as specific input to the micromechanical models beyond what can be found in the literature; (2) Experimental data may be needed for the validation of the newly developed micromechanical and structural model; and (3) Some innovative experiments may be needed to further study the material behavior and structural response. This is particularly important for testing in high temperature environment since it usually requires very delicate experiment design in heating, specimen alignment and strain measurement.

However, experimental study is typically time consuming and expensive. Also, many test parameters cannot be readily characterized experimentally. The use of a combined analytical and experimental study can be much more efficient. The numerical analysis can be used not only for interpretation of experimental data, but also to explore various testing parameters. Only the most critical of these parameters then need to be verified experimentally.

Many experimental results, including both material characterization and benchmark testing on typical subelements of aircraft components, are now available. However, there are no reliable analytical models available, which can model the damage and failure and predict the life of fiber reinforced composite materials and their structures. Therefore, there is an need at this stage of NASA aircraft programs for an efficient and effective life prediction methodology which can interpret these large amount of experimental data and further predict the material life and structural durability.

In our new contract with NASA (Program Monitor Mike Verrilli), some of the issues addressed above will be investigated. Particularly, a combined analytical and experimental approach will be used. A life prediction methodology will be developed for ceramic matrix composite materials. Experimental study will also be performed to generate needed data for the analysis and validate the analytical model.

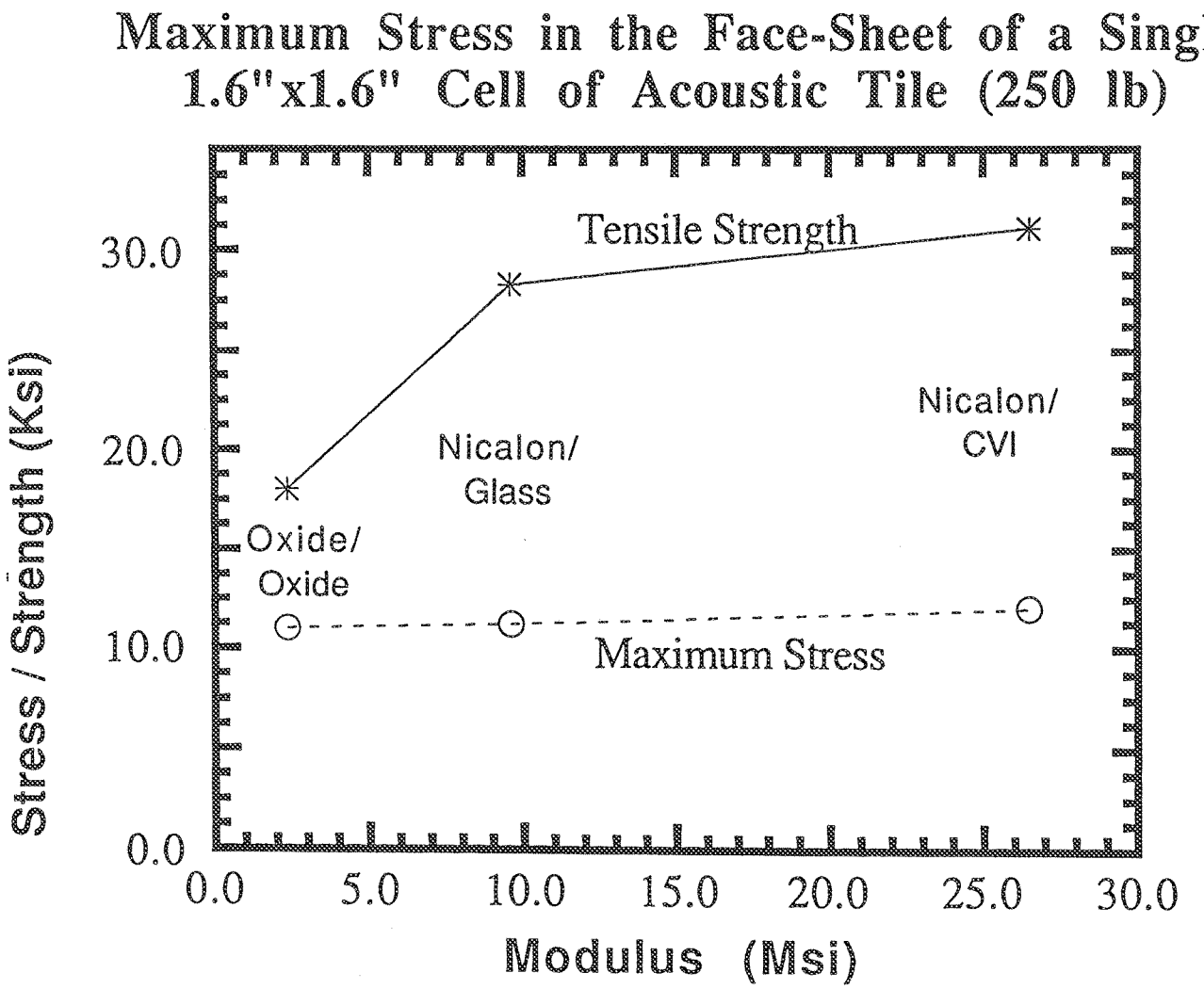
Maximum Stress in the Face-Sheet of a Single 1.6"x1.6" Cell of Acoustic Tile (250 lb)
Tensile Strength
Nicalon/ CVI
Nicalon/ Glass
Oxide/ Oxide
Maximum Stress
Stress / Strength (Ksi)
30.0
20.0
10.0
0.0
0.0
5.0
10.0
15.0
20.0
25.0
30.0
Modulus (Msi)

Figure 1.

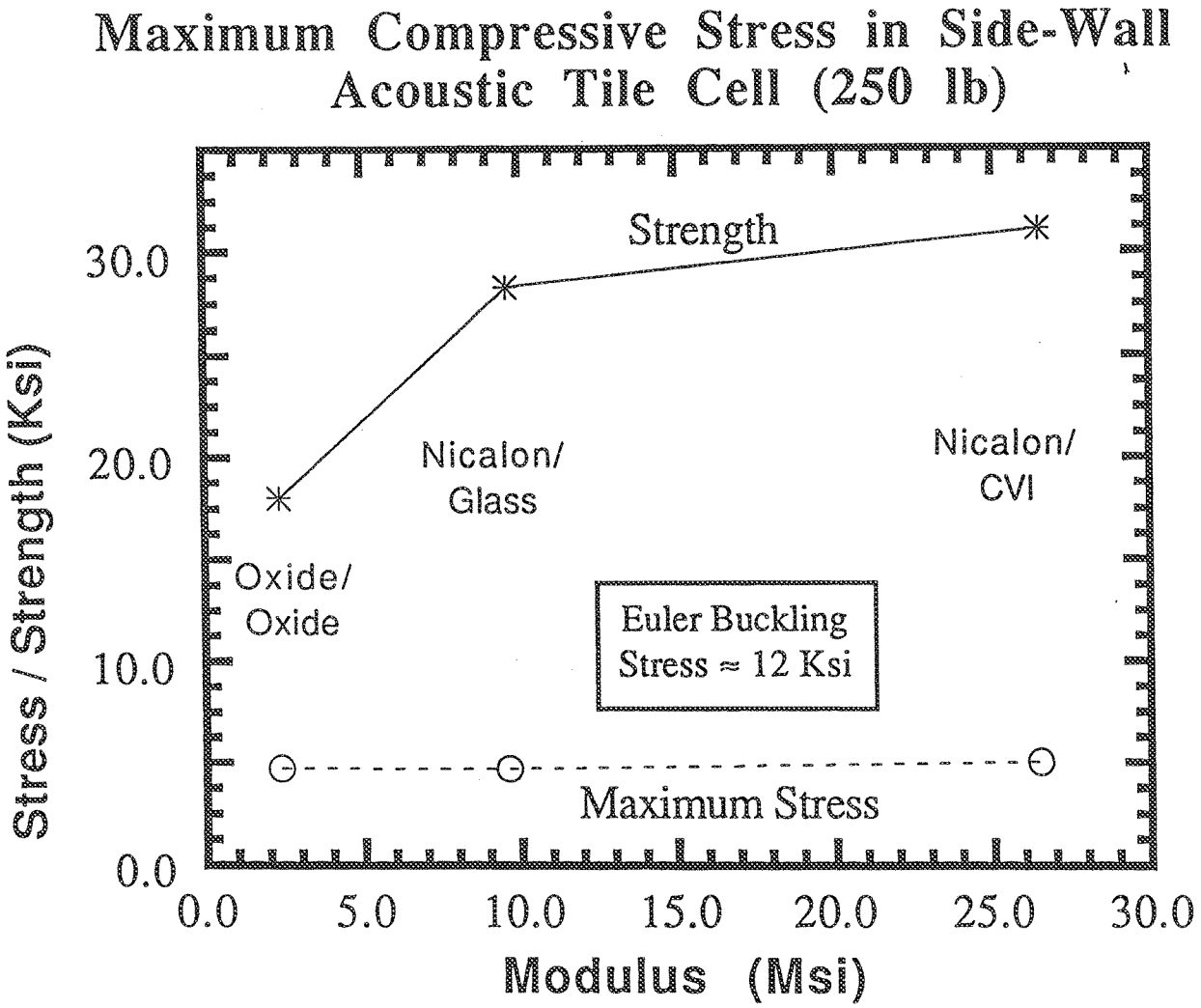
Maximum Compressive Stress in Side-Wall of Acoustic Tile Cell (250 lb)
Strength
Nicalon/ Glass
Nicalon/ CVI
Oxide/ Oxide
Euler Buckling Stress ≈ 12 Ksi
Maximum Stress
Stress / Strength (Ksi)
30.0
20.0
10.0
0.0
0.0
5.0
10.0
15.0
20.0
25.0
30.0
Modulus (Msi)

Figure 2.

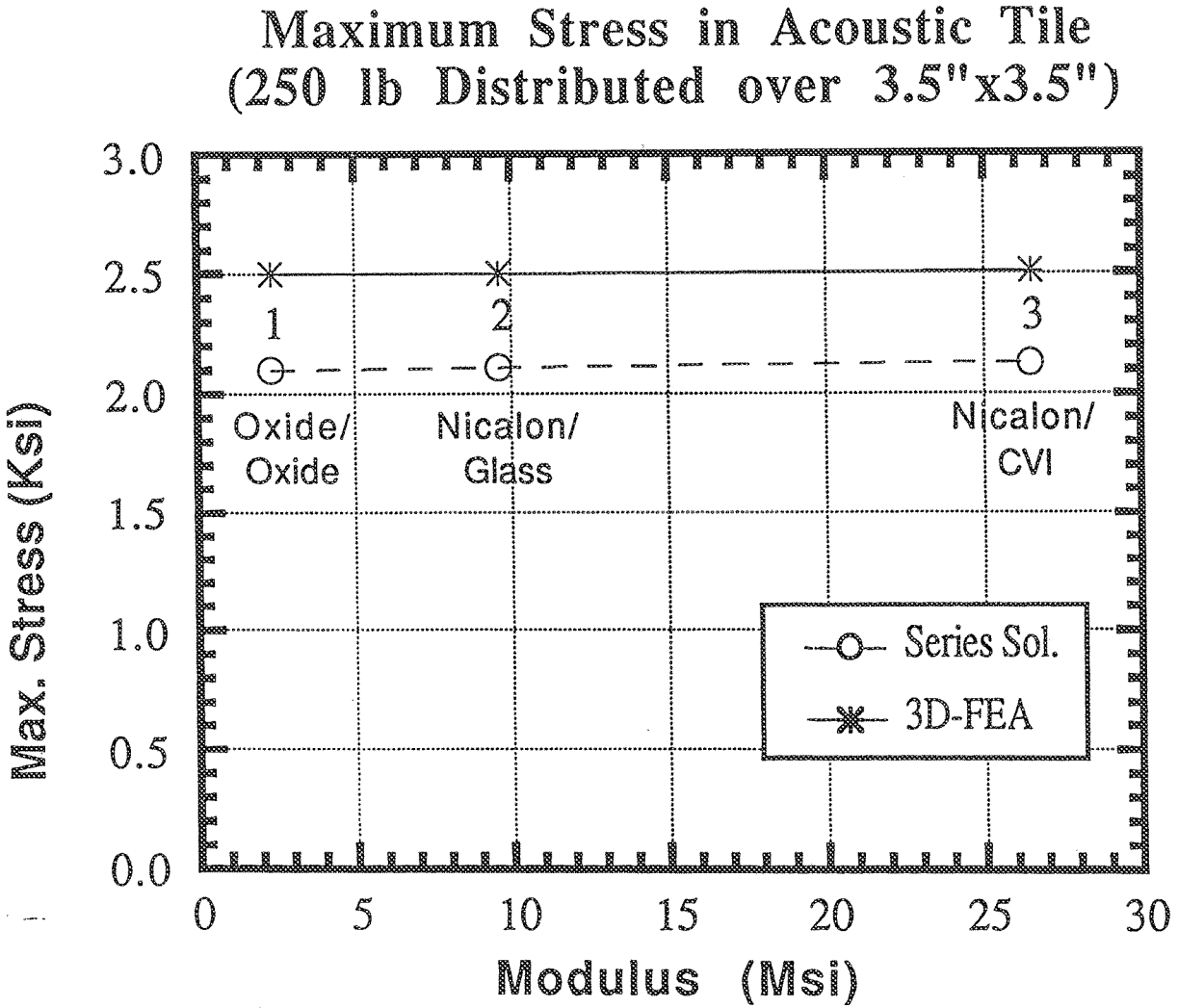
Maximum Stress in Acoustic Tile
(250 lb Distributed over 3.5"x3.5")
Max. Stress (Ksi)
3.0
2.5
2.0
1.5
1.0
0.5
0.0
0
5
10
15
20
25
30
Modulus (Msi)
1
2
3
Oxide/
Oxide
Nicalon/
Glass
Nicalon/
CVI
Series Sol.
3D-FEA

Figure 3.

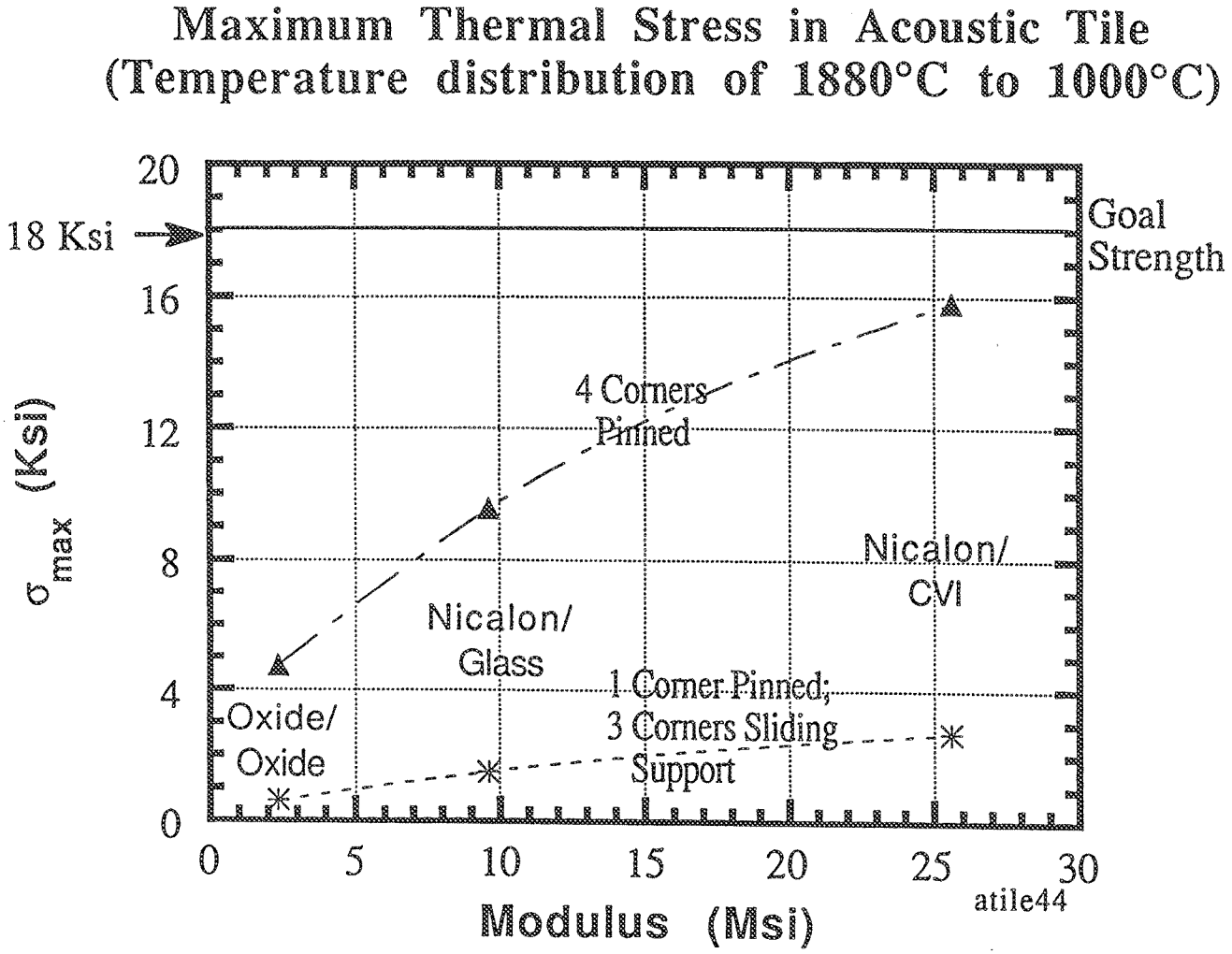
Maximum Thermal Stress in Acoustic Tile
(Temperature distribution of 1880°C to 1000°C)
20
18 Ksi
16
12
8
4
0
σmax (Ksi)
Goal
Strength
4 Corners
Pinned
Nicalon/
CVI
Nicalon/
Glass
1 Corner Pinned;
3 Corners Sliding
Support
Oxide/
Oxide
0
5
10
15
20
25
30
Modulus (Msi)
atile44

Figure 4.

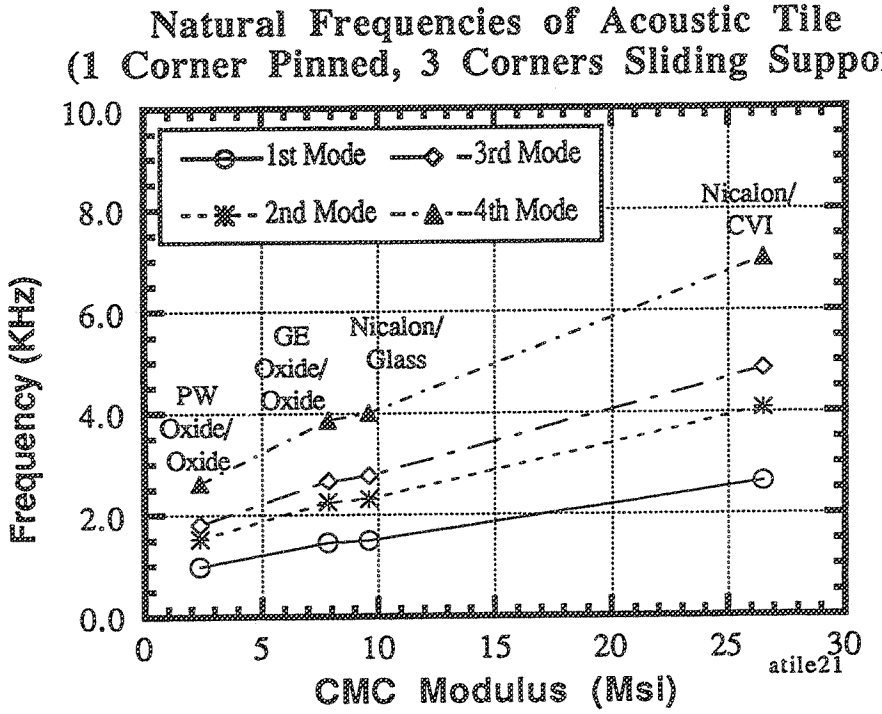
Natural Frequencies of Acoustic Tile
(1 Corner Pinned, 3 Corners Sliding Support)
1st Mode
2nd Mode
3rd Mode
4th Mode
Nicalon/
CVI
GE
Oxide/
Oxide
Nicalon/
Glass
PW
Oxide/
Oxide
Frequency (KHz)
CMC Modulus (Msi)
atile21

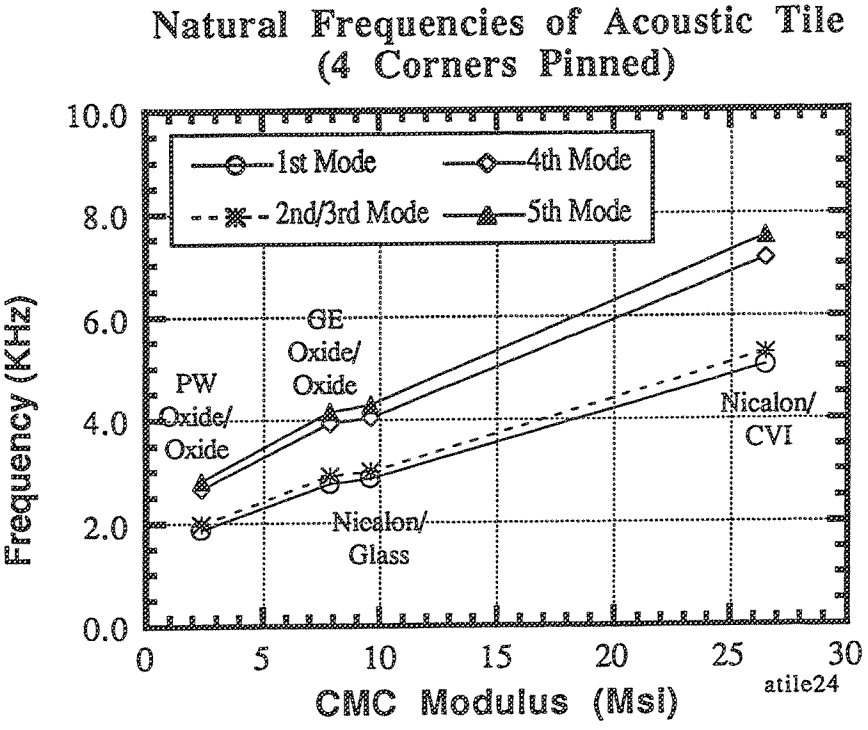
Natural Frequencies of Acoustic Tile
(4 Corners Pinned)
1st Mode
2nd/3rd Mode
4th Mode
5th Mode
GE
Oxide/
Oxide
PW
Oxide/
Oxide
Nicalon/
CVI
Nicalon/
Glass
Frequency (KHz)
CMC Modulus (Msi)
atile24

Figure 5.

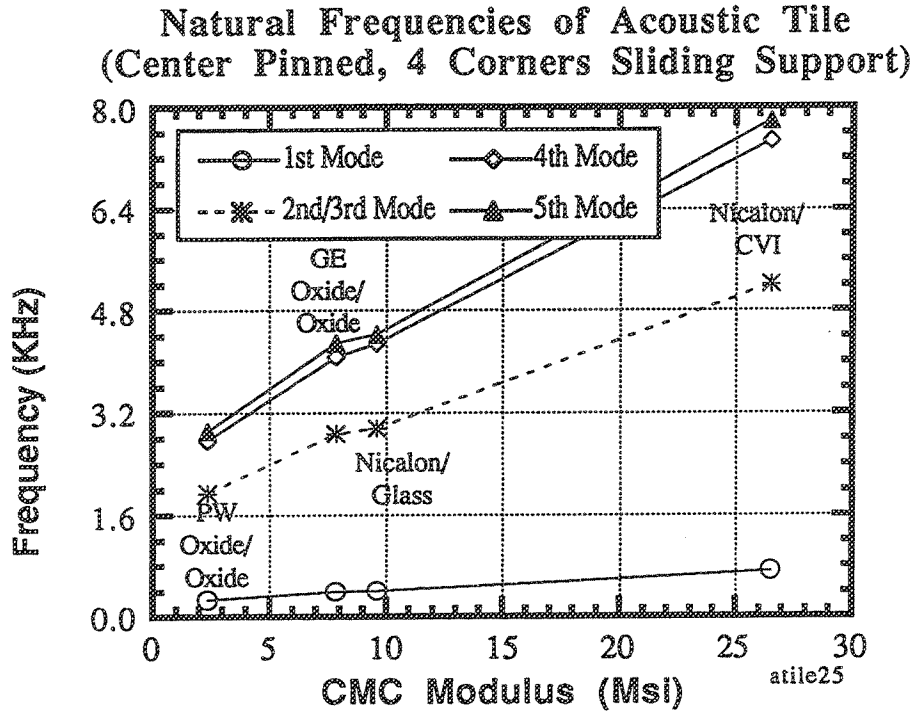
Natural Frequencies of Acoustic Tile
(Center Pinned, 4 Corners Sliding Support)
Frequency (KHz)
8.0
6.4
4.8
3.2
1.6
0.0
0
5
10
15
20
25
30
CMC Modulus (Msi)
atile25
1st Mode
4th Mode
2nd/3rd Mode
5th Mode
GE
Oxide/
Oxide
Nicalon/
CVI
Nicalon/
Glass
PW
Oxide/
Oxide

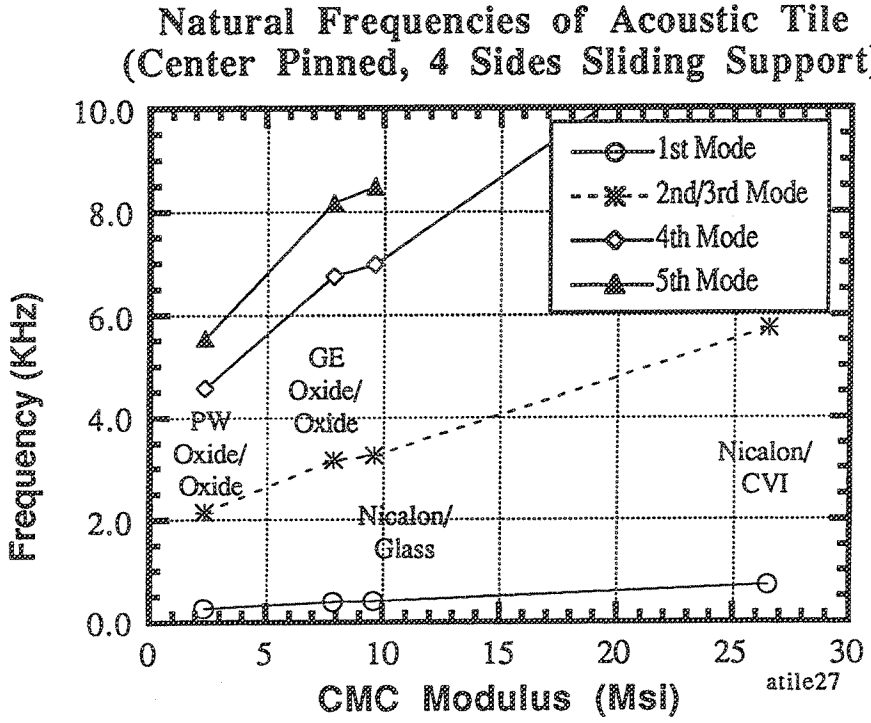
Natural Frequencies of Acoustic Tile
(Center Pinned, 4 Sides Sliding Support)
Frequency (KHz)
10.0
8.0
6.0
4.0
2.0
0.0
0
5
10
15
20
25
30
CMC Modulus (Msi)
atile27
1st Mode
2nd/3rd Mode
4th Mode
5th Mode
GE
Oxide/
Oxide
PW
Oxide/
Oxide
Nicalon/
CVI
Nicalon/
Glass

Figure 6.

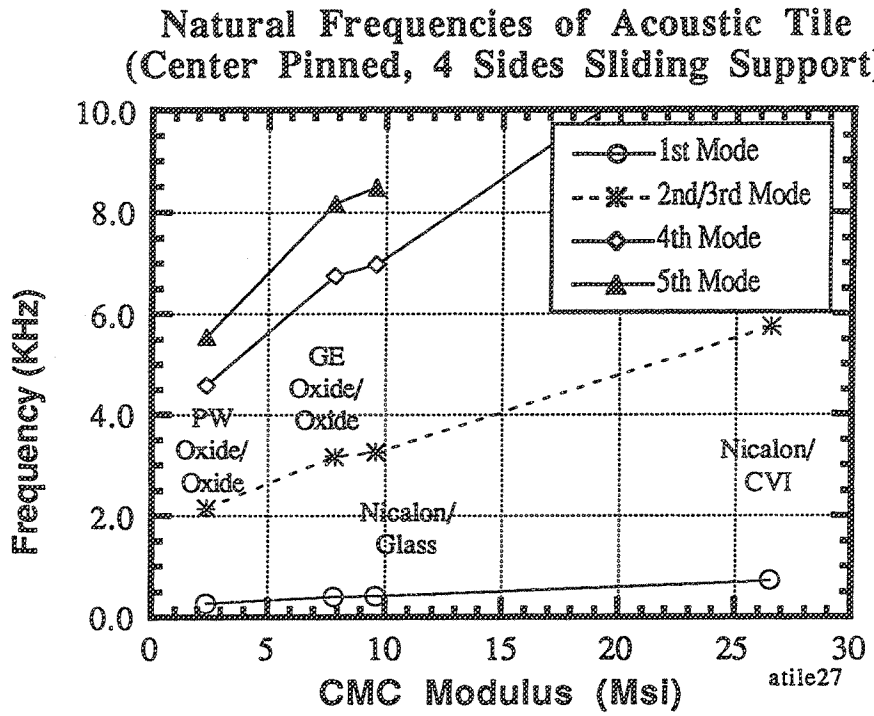
Natural Frequencies of Acoustic Tile
(Center Pinned, 4 Sides Sliding Support)
Frequency (KHz)
CMC Modulus (Msi)
1st Mode
2nd/3rd Mode
4th Mode
5th Mode
GE
Oxide/
Oxide
PW
Oxide/
Oxide
Nicalon/
CVI
Nicalon/
Glass
atile27

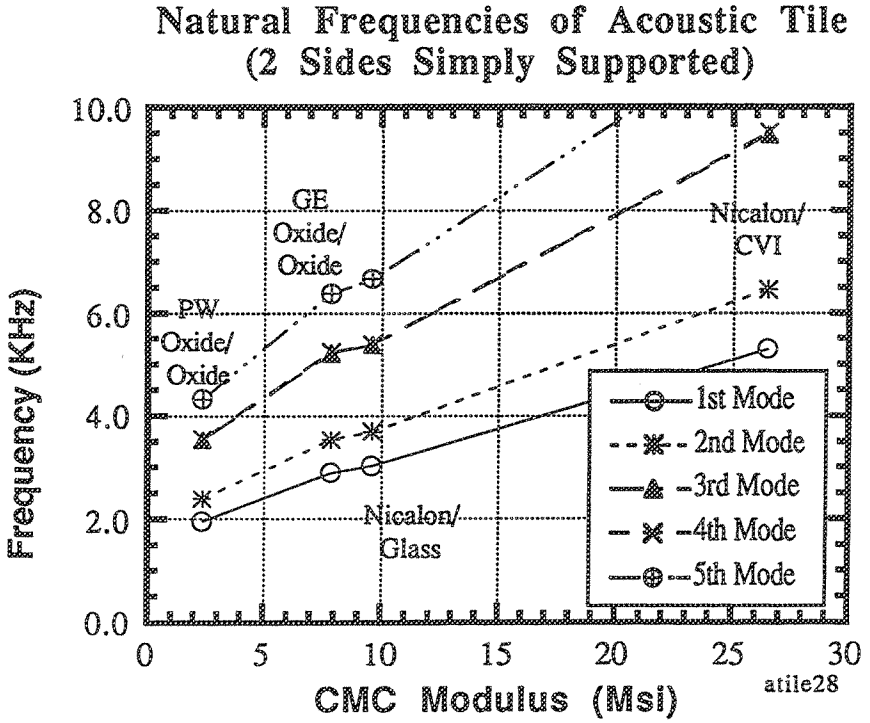
Natural Frequencies of Acoustic Tile
(2 Sides Simply Supported)
Frequency (KHz)
CMC Modulus (Msi)
GE
Oxide/
Oxide
PW
Oxide/
Oxide
Nicalon/
CVI
Nicalon/
Glass
1st Mode
2nd Mode
3rd Mode
4th Mode
5th Mode
atile28

Figure 7.

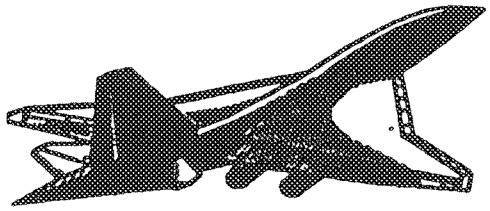

Table 2.

Materials/Design Assessment: Acoustic tile with integral face-sheet & core

Material	Static Stress ($\sigma_{max}/\sigma_{allowable}$)	Thermal Stress ($\sigma_{max}/\sigma_{allowable}$)	Free Vibration (ν_1/5KHz)	Weight (lbf)
Amercom 2D SiC/SiC	0.004	0.300	0.586	4.63
BF Goodrich 2D SiC/SiC	0.004	0.206	0.520	4.26
Corning-Kaiser 2D SiC/SiC	0.004	0.145	0.450	3.52
DuPont/Lanxide 2D SiC/SiC	0.004	0.302	0.531	3.70
HITCO 2D SiC/C	0.004	0.144	0.450	3.24
GE/Hexel 2D Oxide/Oxide	0.003	0.250	0.400	4.63
Techniweave 3D Oxide/Oxide	0.038	1.308	0.260	4.63
PW Altex/Alumina 3D CMC	0.015	0.172	0.197	3.03
PW Nextel 440/Alumina	0.007	0.325	0.322	3.19
PW Nextel 440/Silica 3D	0.009	0.400	0.310	3.24
UTRC Nicalon/1723 CMC	0.005	0.234	0.345	4.35
UTRC UT-22 2D	0.003	0.129	0.439	4.44
UTRC UT-22 3D	0.004	0.150	0.435	4.44

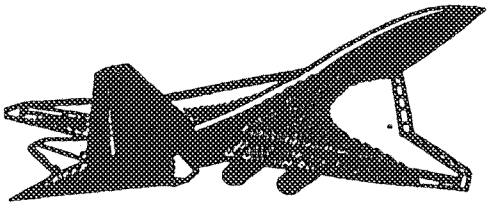

Table 3.

Materials/Design Assessment: Acoustic tile with non-integral face-sheet & core

Material	Static Stress ($\sigma_{max}/\sigma_{allowable}$)	Thermal Stress ($\sigma_{max}/\sigma_{allowable}$)	Free Vibration (ν_1/5KHz)	Weight (lbf)
Amercom 2D SiC/SiC	0.140	0.430	0.056	1.91
BF Goodrich 2D SiC/SiC	0.120	0.266	0.051	1.76
Corning-Kaiser 2D SiC/SiC	0.133	0.134	0.043	1.46
DuPont/Lanxide 2D SiC/SiC	0.121	0.428	0.052	1.53
HITCO 2D SiC/C	0.138	0.219	0.045	1.34
GE/Hexel 2D Oxide/Oxide	0.102	0.339	0.029	1.91
Techniweave 3D Oxide/Oxide	0.694	1.536	0.023	1.91
PW Altex/Alumina 3D CMC	0.588	0.201	0.019	1.25
PW Nextel 440/Alumina	0.256	0.324	0.031	1.32
PW Nextel 440/Silica 3D	0.411	0.318	0.027	1.34
UTRC Nicalon/1723 CMC	0.153	0.308	0.033	1.80
UTRC UT-22 2D	0.096	0.182	0.043	1.84
UTRC UT-22 3D	0.117	0.128	0.036	1.84

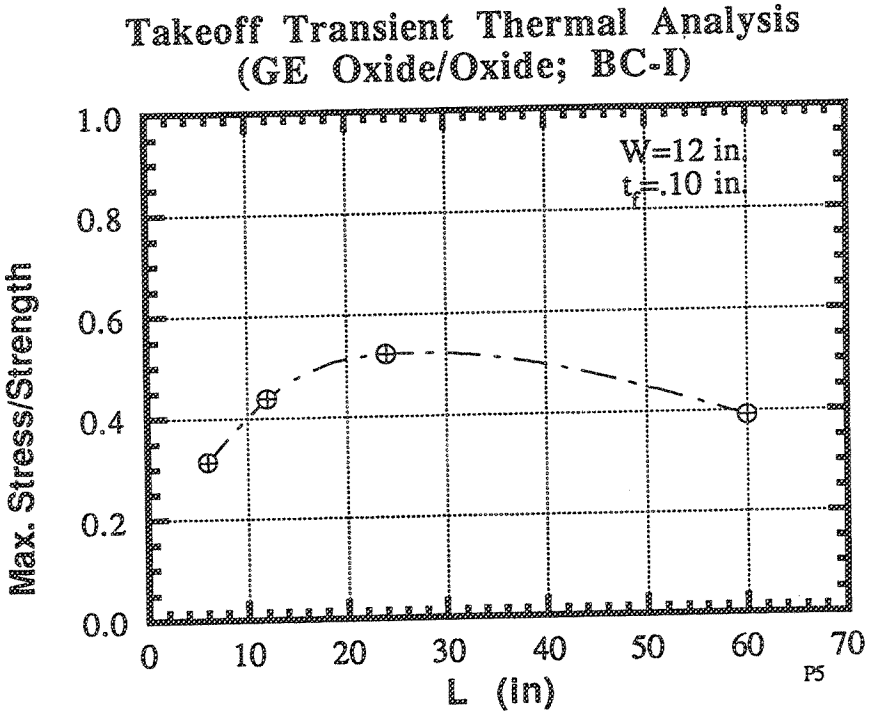
Takeoff Transient Thermal Analysis
(GE Oxide/Oxide; BC-I)
W=12 in.
t_f=.10 in.
Max. Stress/Strength
1.0
0.8
0.6
0.4
0.2
0.0
0
10
20
30
40
50
60
70
L (in)
P5

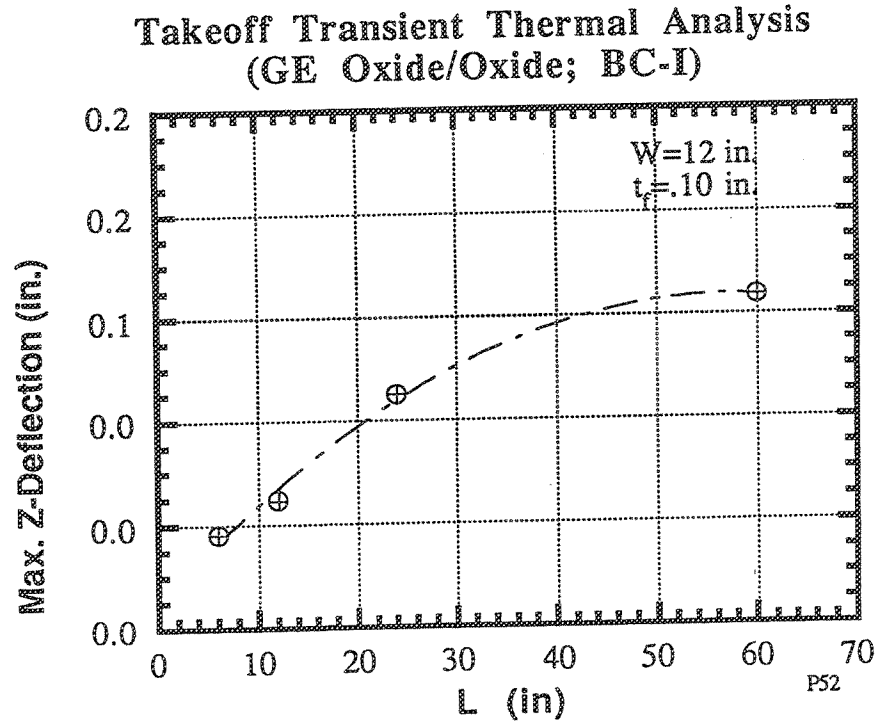
Takeoff Transient Thermal Analysis
(GE Oxide/Oxide; BC-I)
W=12 in.
t_f=.10 in.
Max. Z-Deflection (in.)
0.2
0.2
0.1
0.0
0.0
0.0
0
10
20
30
40
50
60
70
L (in)
P52

Figure 8.

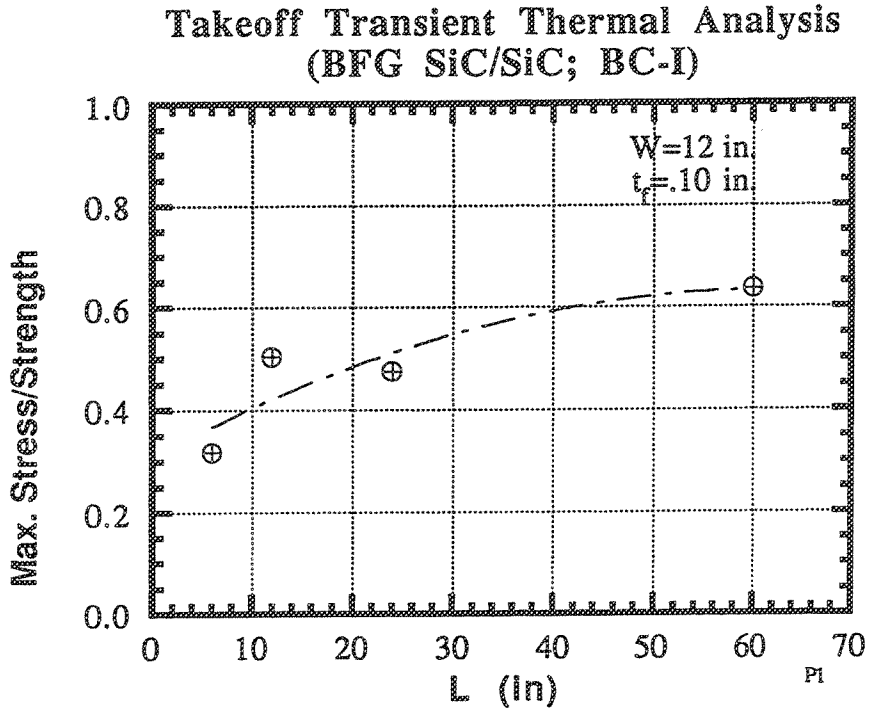
Takeoff Transient Thermal Analysis
(BFG SiC/SiC; BC-I)
Max. Stress/Strength
1.0
0.8
0.6
0.4
0.2
0.0
W=12 in.
t_f=.10 in.
0
10
20
30
40
50
60
70
L (in)
P1

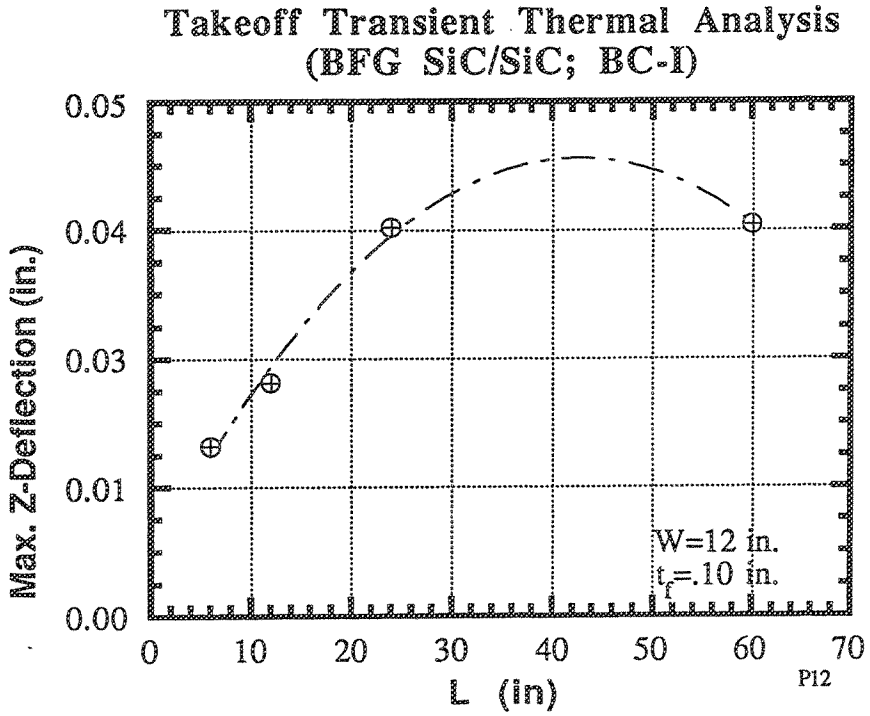
Takeoff Transient Thermal Analysis
(BFG SiC/SiC; BC-I)
Max. Z-Deflection (in.)
0.05
0.04
0.03
0.01
0.00
W=12 in.
t_f=.10 in.
0
10
20
30
40
50
60
70
L (in)
P12

Figure 9.

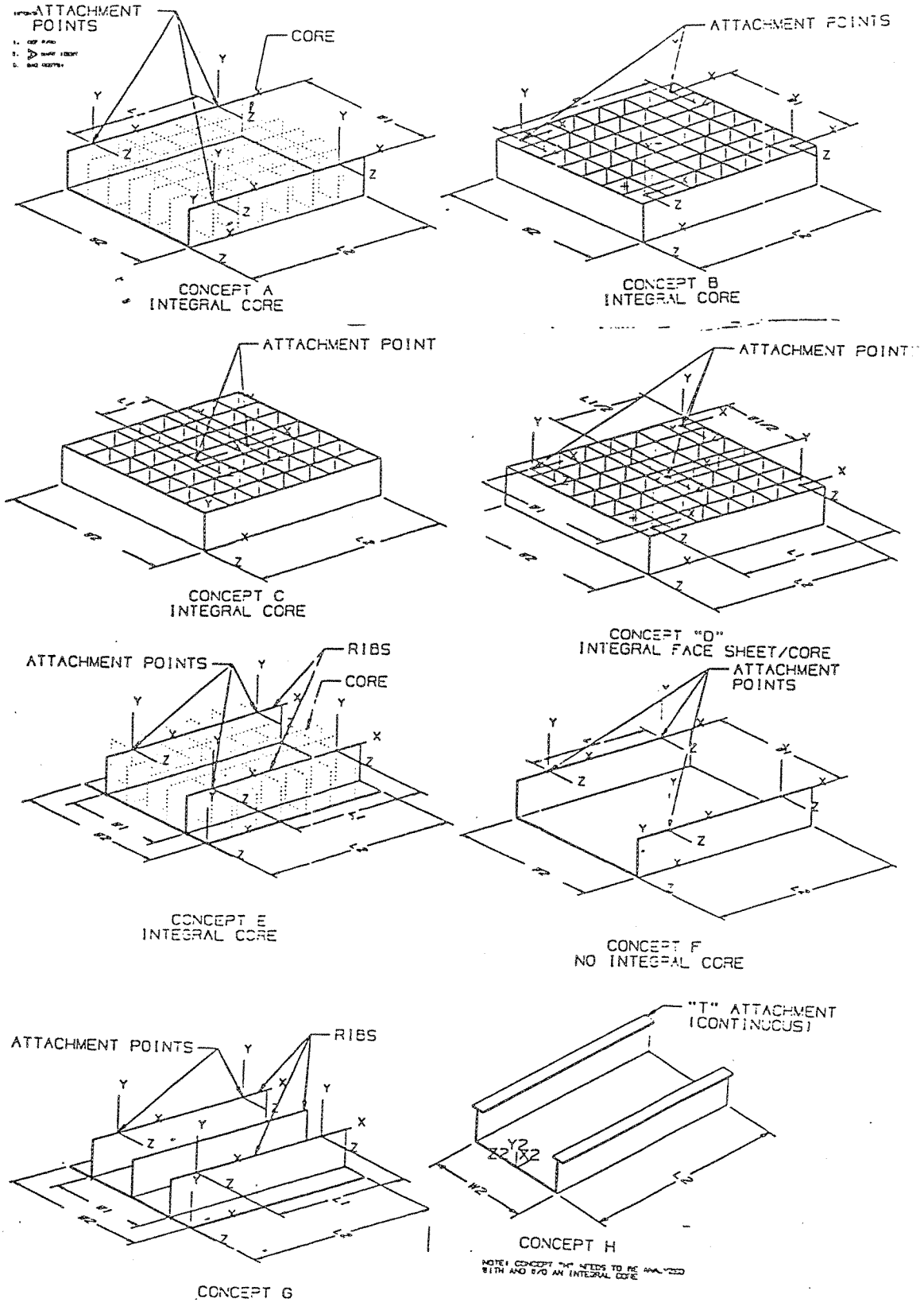

Figure 10. CMC Acoustic Tile Design Concepts Received From P&W.

Table 4. Initial Candidate Material Systems for CMC Acoustic Tile Liner.

2D	Amercom SiC/SiC
	BF Goodrich SiC/SiC
	Corning-Kaiser SiC/SiC
	DuPont/Lanxide SiC/SiC
	HITCO SiC/C
	GE/Hexel Oxide/Oxide
	UTRC UT-22
3D	Techniweave Oxide/Oxide
	PW Altex/Alumina
	PW Nextel 440/Alumina
	PW Nextel 440/Silica
	UTRC Nicalon/1723
	UTRC UT-22

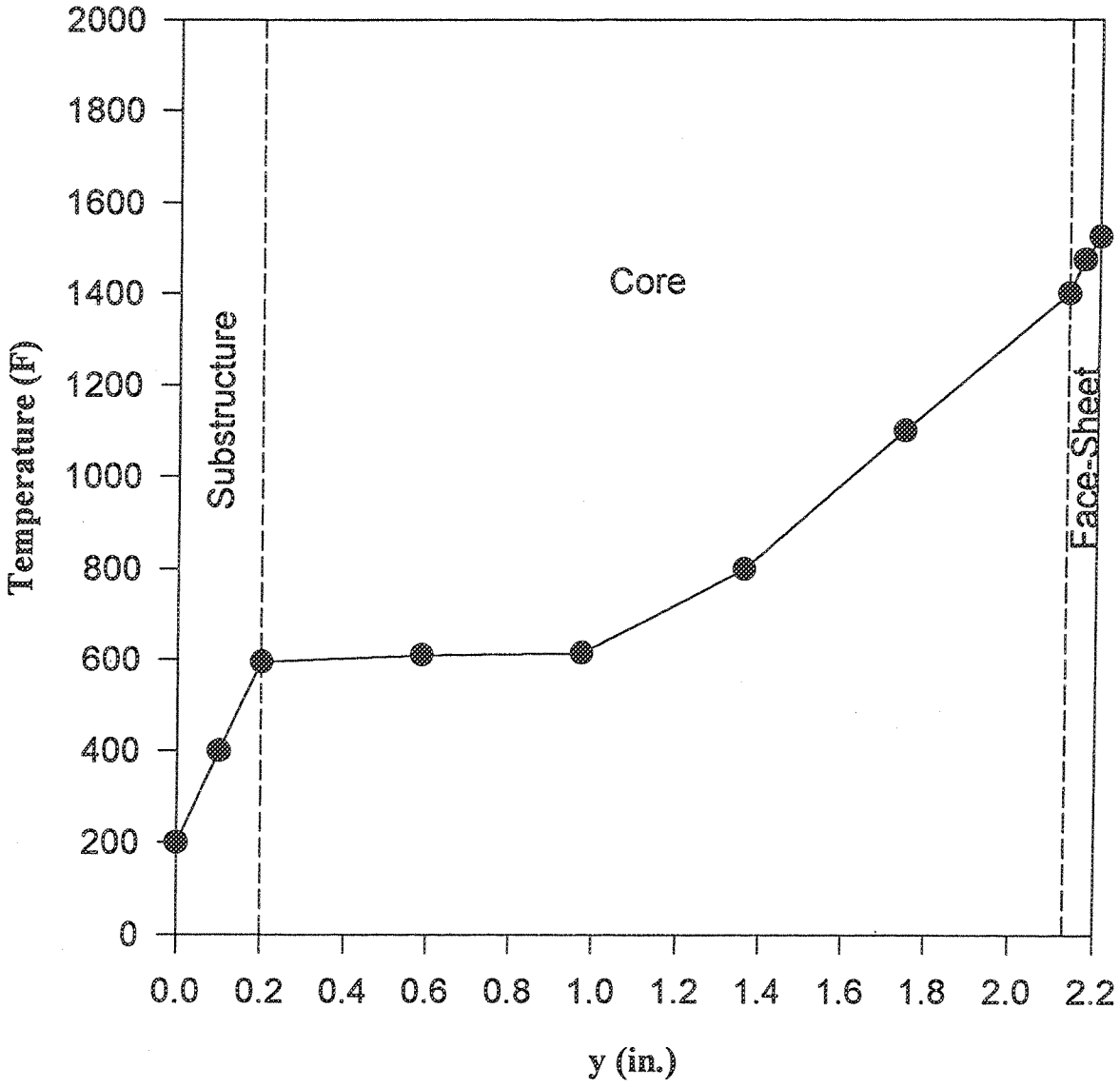
Temperature distribution used in the Thermal Analysis
2000
1800
1600
1400
1200
1000
800
600
400
200
0
Temperature (F)
Substructure
Core
Face-Sheet
0.0
0.2
0.4
0.6
0.8
1.0
1.2
1.4
1.6
1.8
2.0
2.2
y (in.)

Figure 11.

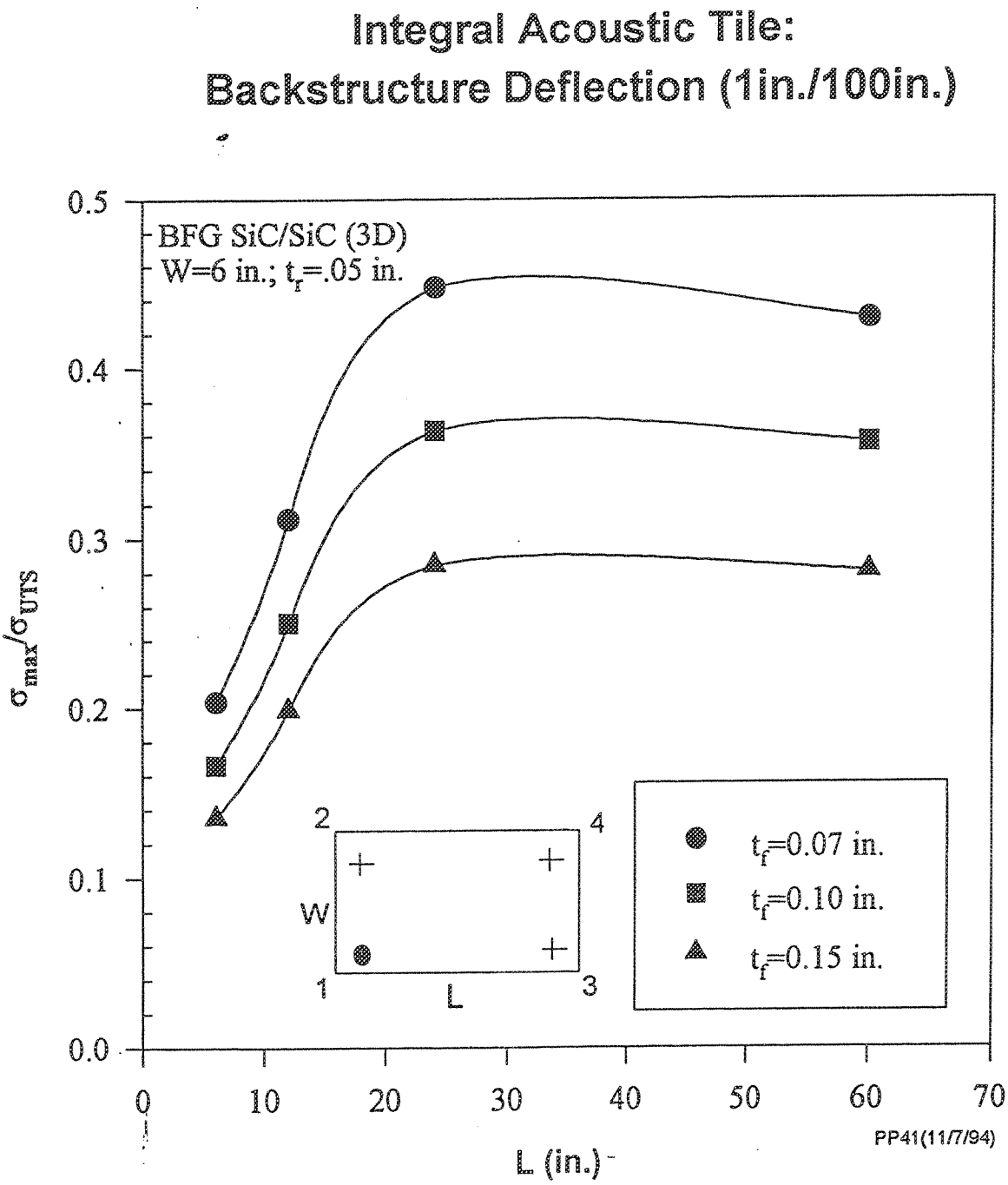
Integral Acoustic Tile:
Backstructure Deflection (1in./100in.)
BFG SiC/SiC (3D)
W=6 in.; t_r=.05 in.
$\sigma_{max}/\sigma_{UTS}$
0.5
0.4
0.3
0.2
0.1
0.0
0
10
20
30
40
50
60
70
L (in.)
2
4
W
1
L
3
t_f=0.07 in.
t_f=0.10 in.
t_f=0.15 in.
PP41(11/7/94)

Figure 12.

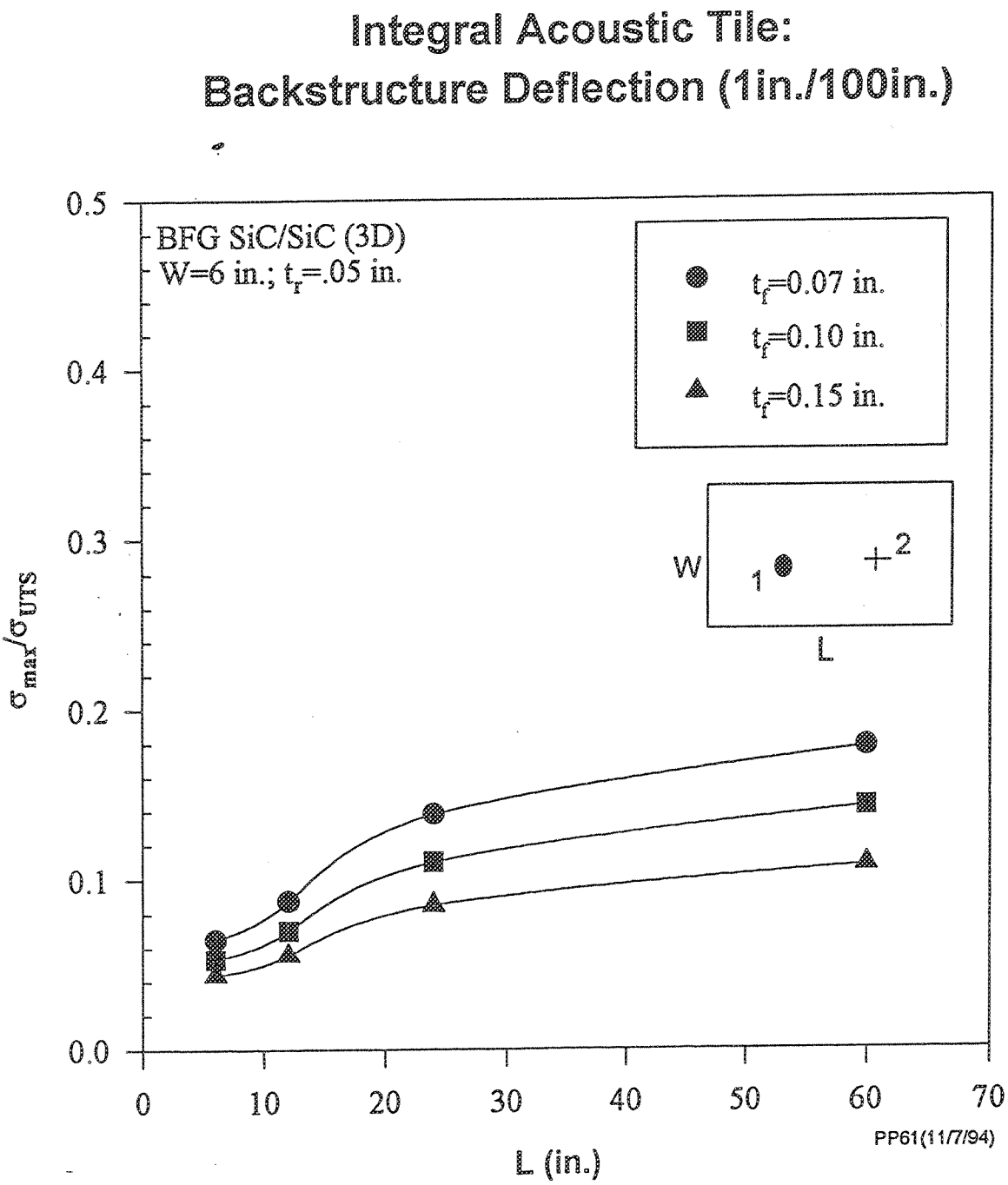
Integral Acoustic Tile:
Backstructure Deflection (1in./100in.)
BFG SiC/SiC (3D)
W=6 in.; t_r=.05 in.
t_f=0.07 in.
t_f=0.10 in.
t_f=0.15 in.
W
1
2
L
σ_max/σ_UTS
0.0
0.1
0.2
0.3
0.4
0.5
0
10
20
30
40
50
60
70
L (in.)
PP61(11/7/94)

Figure 13.

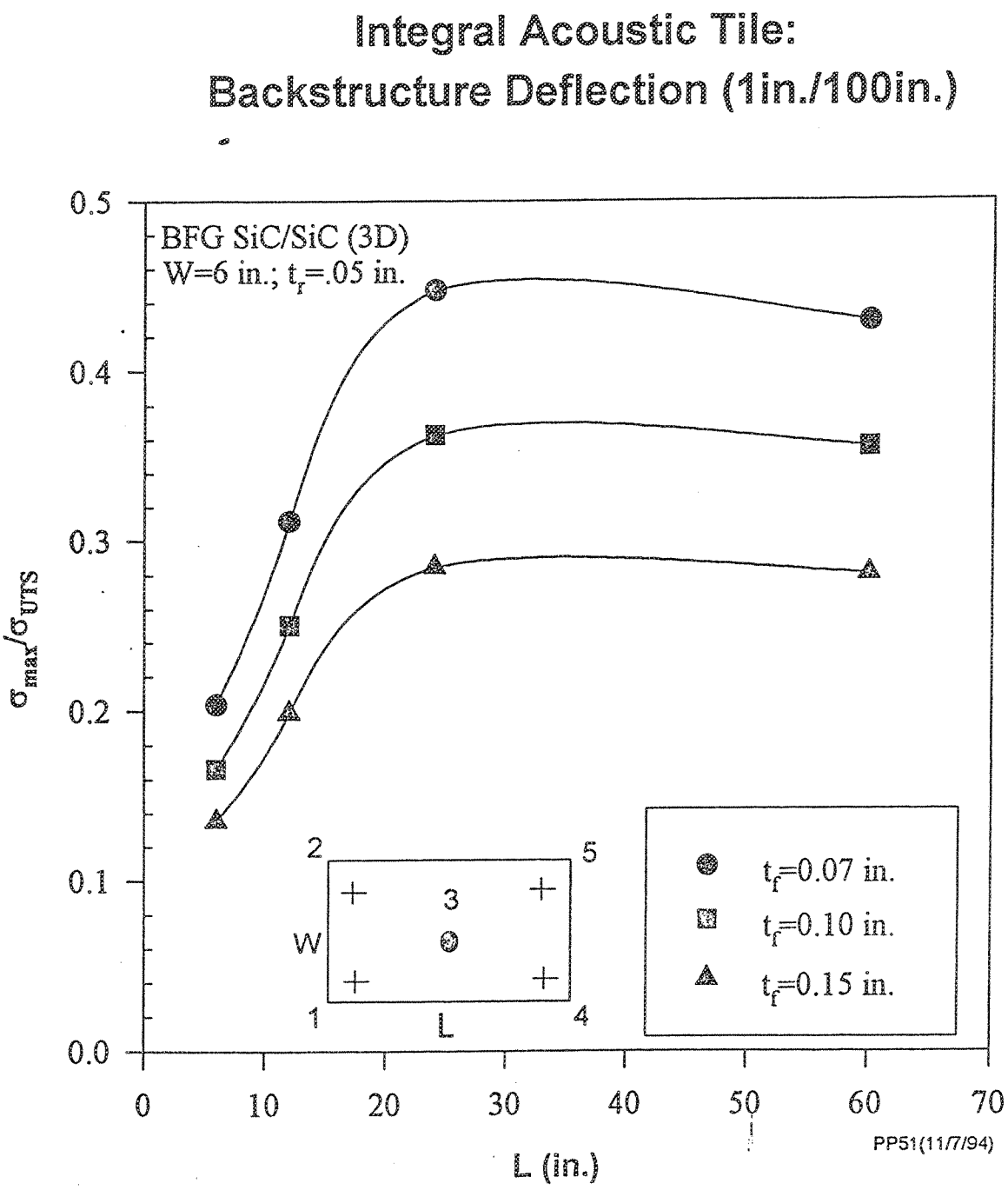
Integral Acoustic Tile:
Backstructure Deflection (1in./100in.)
BFG SiC/SiC (3D)
W=6 in.; t_r=.05 in.
$\sigma_{max}/\sigma_{UTS}$
0.5
0.4
0.3
0.2
0.1
0.0
0
10
20
30
40
50
60
70
L (in.)
2
5
3
W
1
L
4
t_f=0.07 in.
t_f=0.10 in.
t_f=0.15 in.
PP51(11/7/94)

Figure 14.

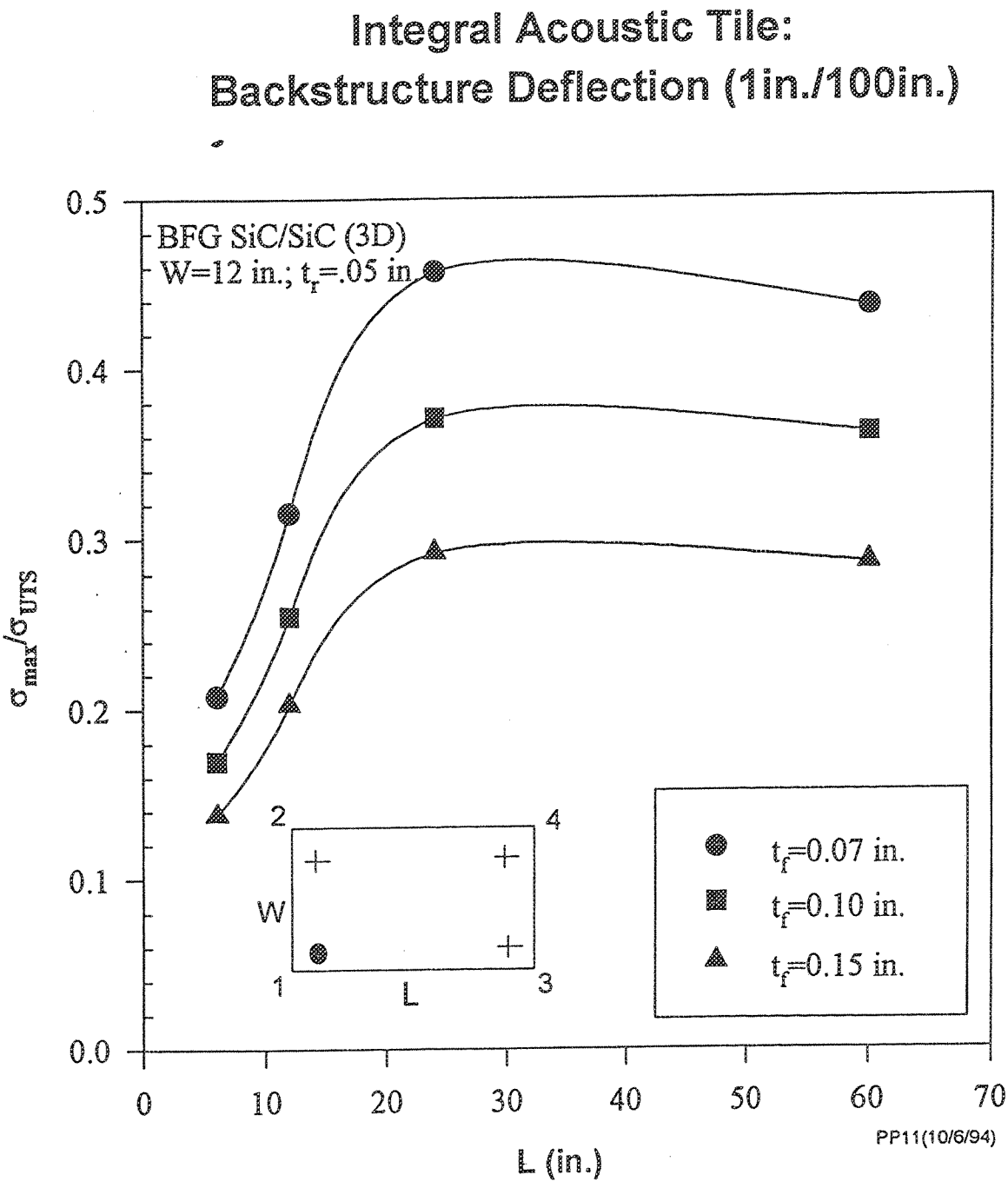
Integral Acoustic Tile:
Backstructure Deflection (1in./100in.)
BFG SiC/SiC (3D)
W=12 in.; t_r=.05 in.
$\sigma_{max}/\sigma_{UTS}$
0.5
0.4
0.3
0.2
0.1
0.0
0
10
20
30
40
50
60
70
L (in.)
2
4
W
1
L
3
t_f=0.07 in.
t_f=0.10 in.
t_f=0.15 in.
PP11(10/6/94)

Figure 15.

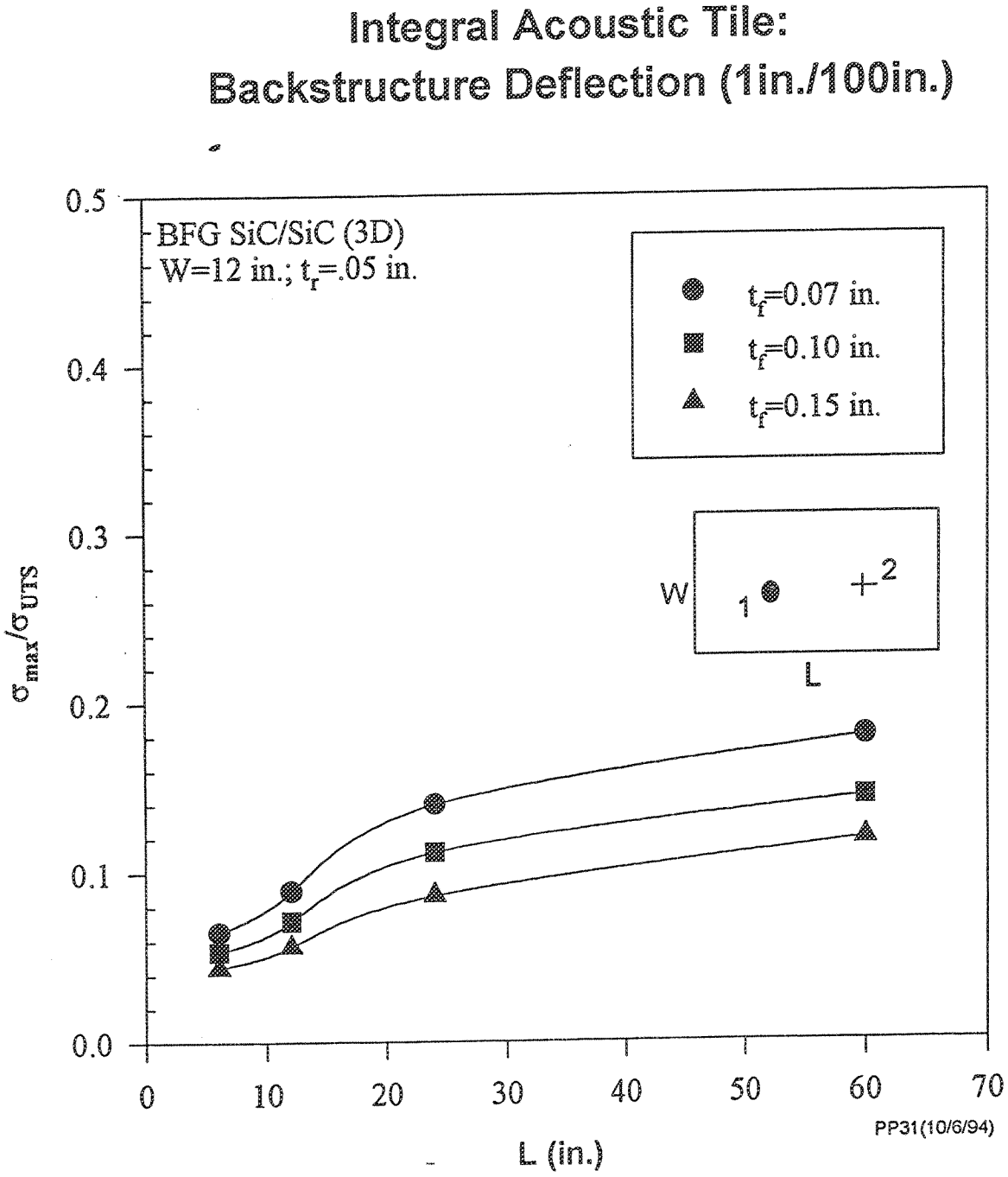
Integral Acoustic Tile:
Backstructure Deflection (1in./100in.)
BFG SiC/SiC (3D)
W=12 in.; t_r=.05 in.
t_f=0.07 in.
t_f=0.10 in.
t_f=0.15 in.
W
1
2
L
$\sigma_{max}/\sigma_{UTS}$
0.0
0.1
0.2
0.3
0.4
0.5
0
10
20
30
40
50
60
70
L (in.)
PP31(10/6/94)

Figure 16.

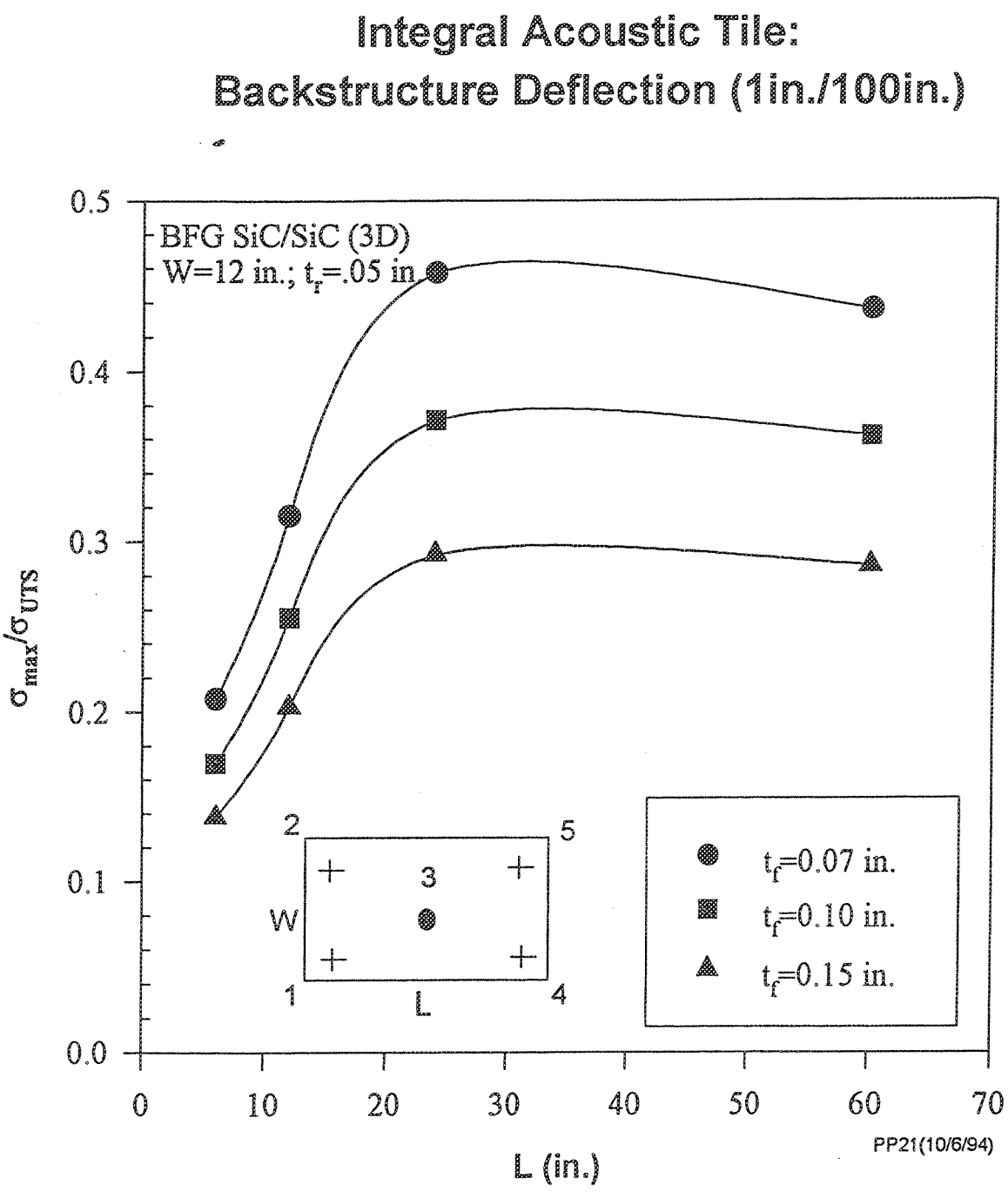
Integral Acoustic Tile:
Backstructure Deflection (1in./100in.)
BFG SiC/SiC (3D)
W=12 in.; t_r=.05 in
σmax/σUTS
0.0
0.1
0.2
0.3
0.4
0.5
0
10
20
30
40
50
60
70
L (in.)
2
5
3
W
1
4
L
tf=0.07 in.
tf=0.10 in.
tf=0.15 in.
PP21(10/6/94)

Figure 17.

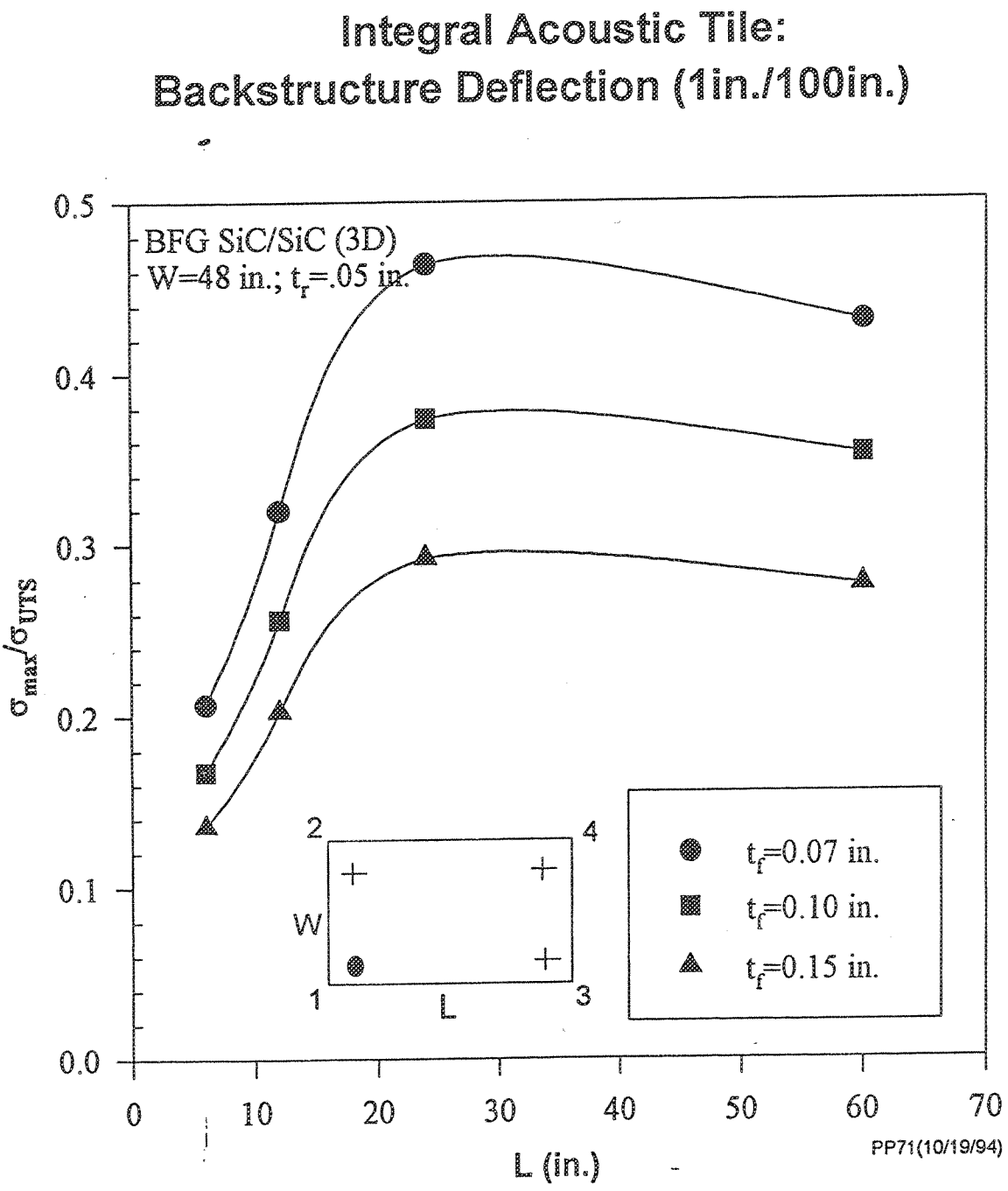
Integral Acoustic Tile:
Backstructure Deflection (1in./100in.)
BFG SiC/SiC (3D)
W=48 in.; t_r=.05 in.
$\sigma_{max}/\sigma_{UTS}$
0.0
0.1
0.2
0.3
0.4
0.5
0
10
20
30
40
50
60
70
L (in.)
2
4
W
1
3
L
t_f=0.07 in.
t_f=0.10 in.
t_f=0.15 in.
PP71(10/19/94)

Figure 18.

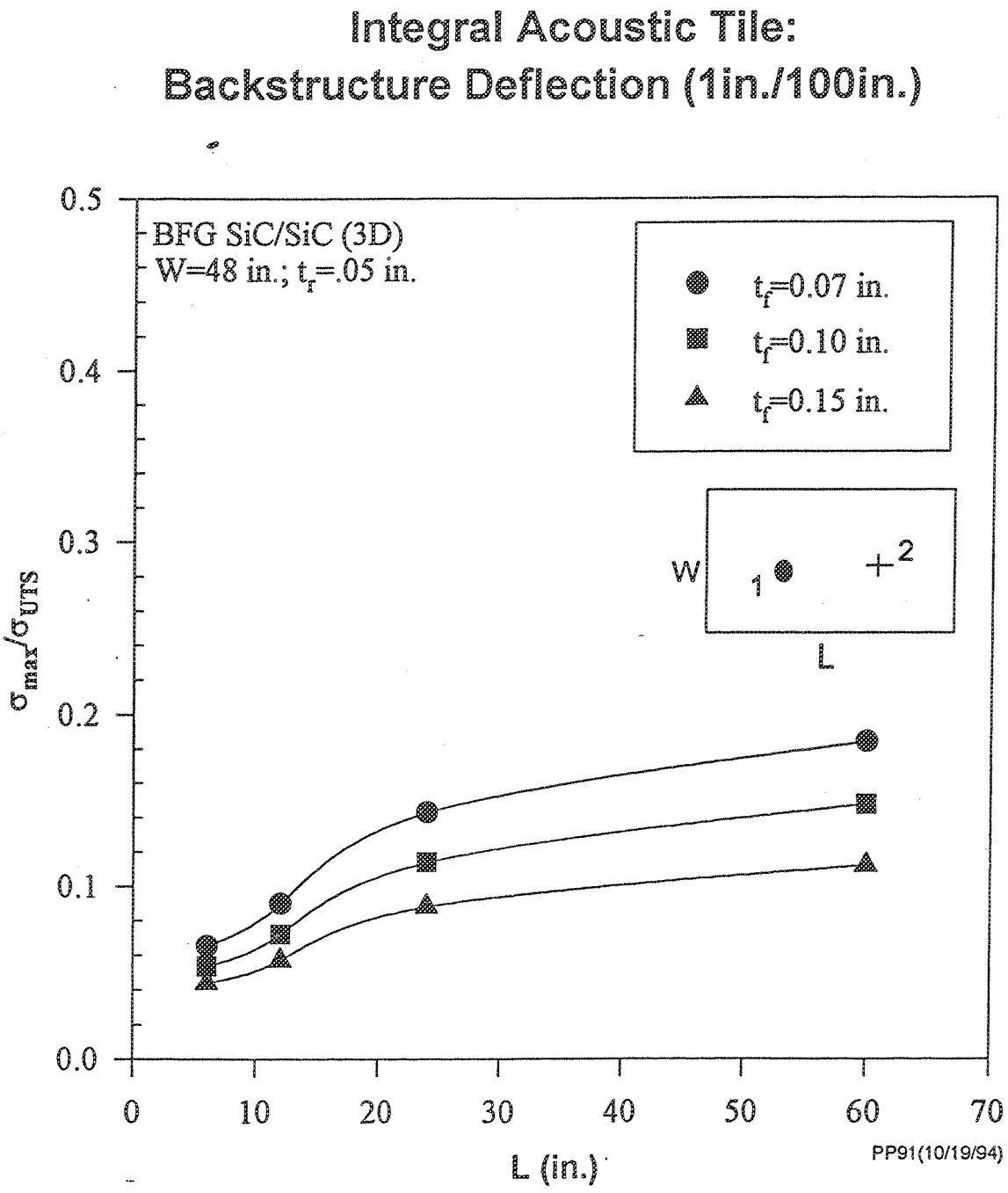
Integral Acoustic Tile:
Backstructure Deflection (1in./100in.)
BFG SiC/SiC (3D)
W=48 in.; t_r=.05 in.
t_f=0.07 in.
t_f=0.10 in.
t_f=0.15 in.
W
1
2
L
$\sigma_{max}/\sigma_{UTS}$
0.0
0.1
0.2
0.3
0.4
0.5
0
10
20
30
40
50
60
70
L (in.)
PP91(10/19/94)

Figure 19.

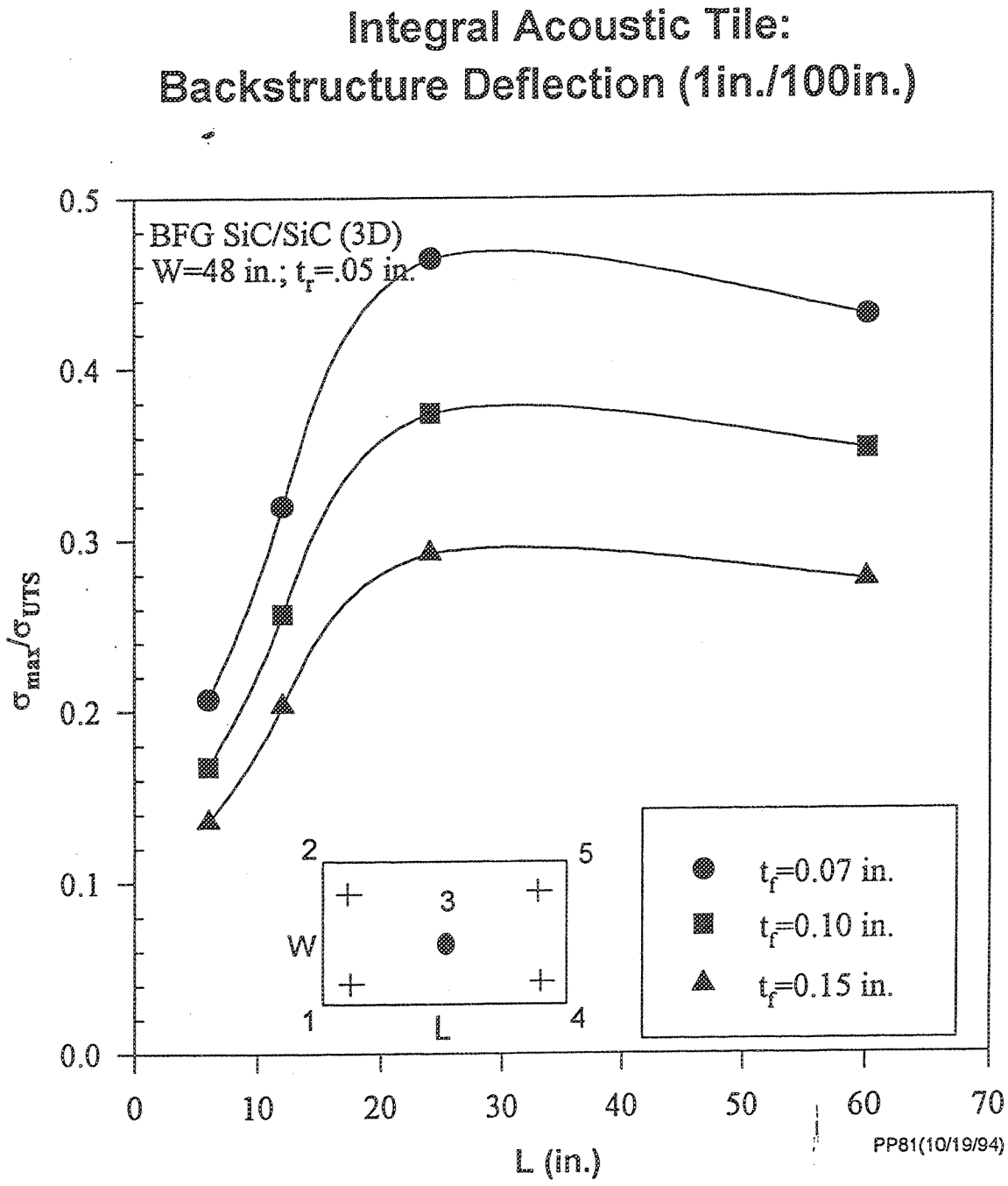
Integral Acoustic Tile:
Backstructure Deflection (1in./100in.)
BFG SiC/SiC (3D)
W=48 in.; t_r=.05 in.
$\sigma_{max}/\sigma_{UTS}$
0.0
0.1
0.2
0.3
0.4
0.5
0
10
20
30
40
50
60
70
L (in.)
1
2
3
4
5
W
L
t_f=0.07 in.
t_f=0.10 in.
t_f=0.15 in.
PP81(10/19/94)

Figure 20.

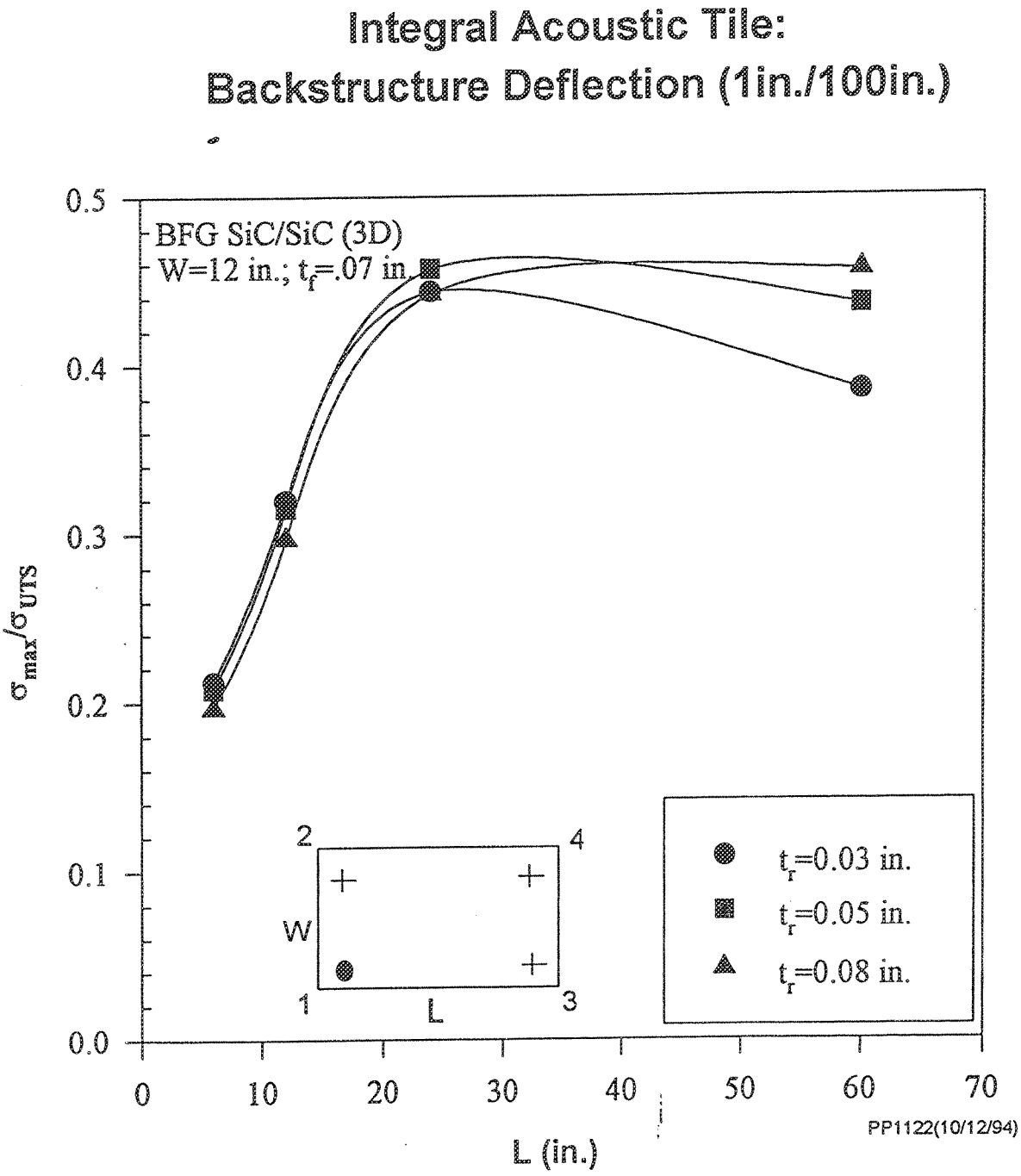
Integral Acoustic Tile:
Backstructure Deflection (1in./100in.)
BFG SiC/SiC (3D)
W=12 in.; t_f=.07 in
$\sigma_{max}/\sigma_{UTS}$
0.5
0.4
0.3
0.2
0.1
0.0
0
10
20
30
40
50
60
70
L (in.)
2
4
W
1
L
3
t_r=0.03 in.
t_r=0.05 in.
t_r=0.08 in.
PP1122(10/12/94)

Figure 21.

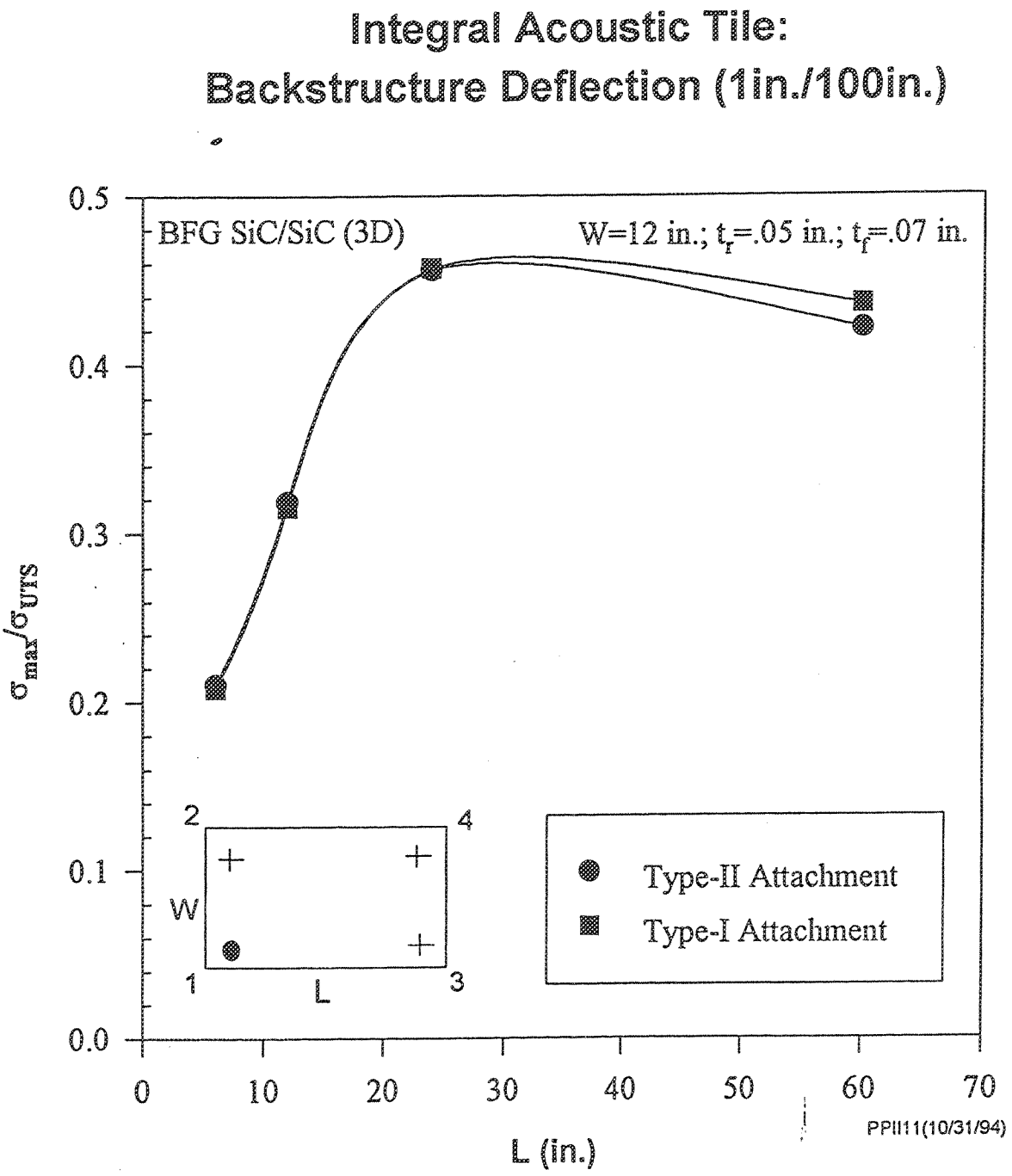
Integral Acoustic Tile:
Backstructure Deflection (1in./100in.)
BFG SiC/SiC (3D)
W=12 in.; t_r=.05 in.; t_f=.07 in.
$\sigma_{max}/\sigma_{UTS}$
0.5
0.4
0.3
0.2
0.1
0.0
0
10
20
30
40
50
60
70
L (in.)
2
4
W
1
L
3
Type-II Attachment
Type-I Attachment
PPII11(10/31/94)

Figure 22.

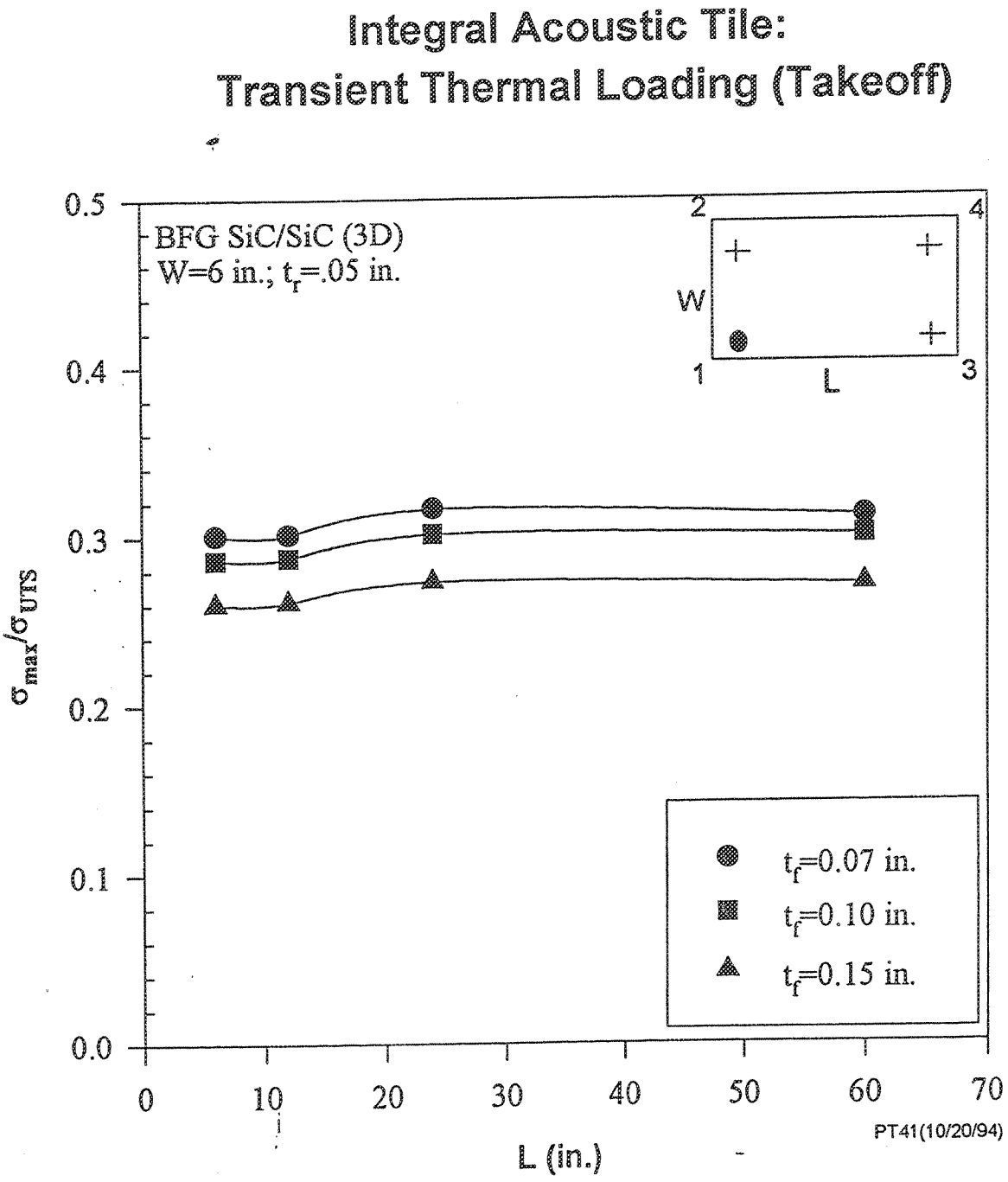
Integral Acoustic Tile:
Transient Thermal Loading (Takeoff)
BFG SiC/SiC (3D)
W=6 in.; t_r=.05 in.
2
4
W
1
L
3
$\sigma_{max}/\sigma_{UTS}$
0.5
0.4
0.3
0.2
0.1
0.0
t_f=0.07 in.
t_f=0.10 in.
t_f=0.15 in.
0
10
20
30
40
50
60
70
L (in.)
PT41(10/20/94)

Figure 23.

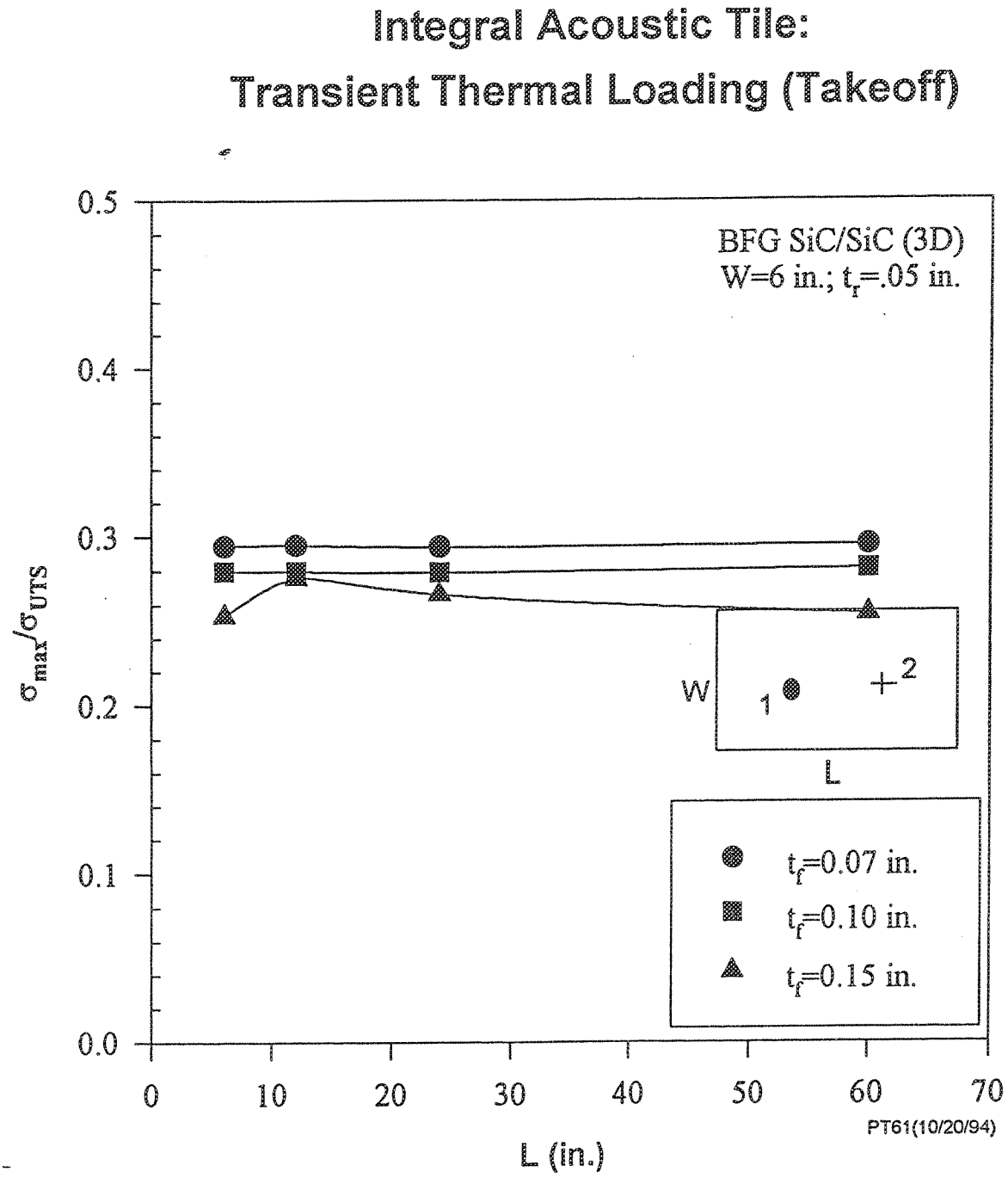
Integral Acoustic Tile:
Transient Thermal Loading (Takeoff)
BFG SiC/SiC (3D)
W=6 in.; t_r=.05 in.
σ_max/σ_UTS
0.5
0.4
0.3
0.2
0.1
0.0
0
10
20
30
40
50
60
70
L (in.)
W
L
1
2
t_f=0.07 in.
t_f=0.10 in.
t_f=0.15 in.
PT61(10/20/94)

Figure 24.

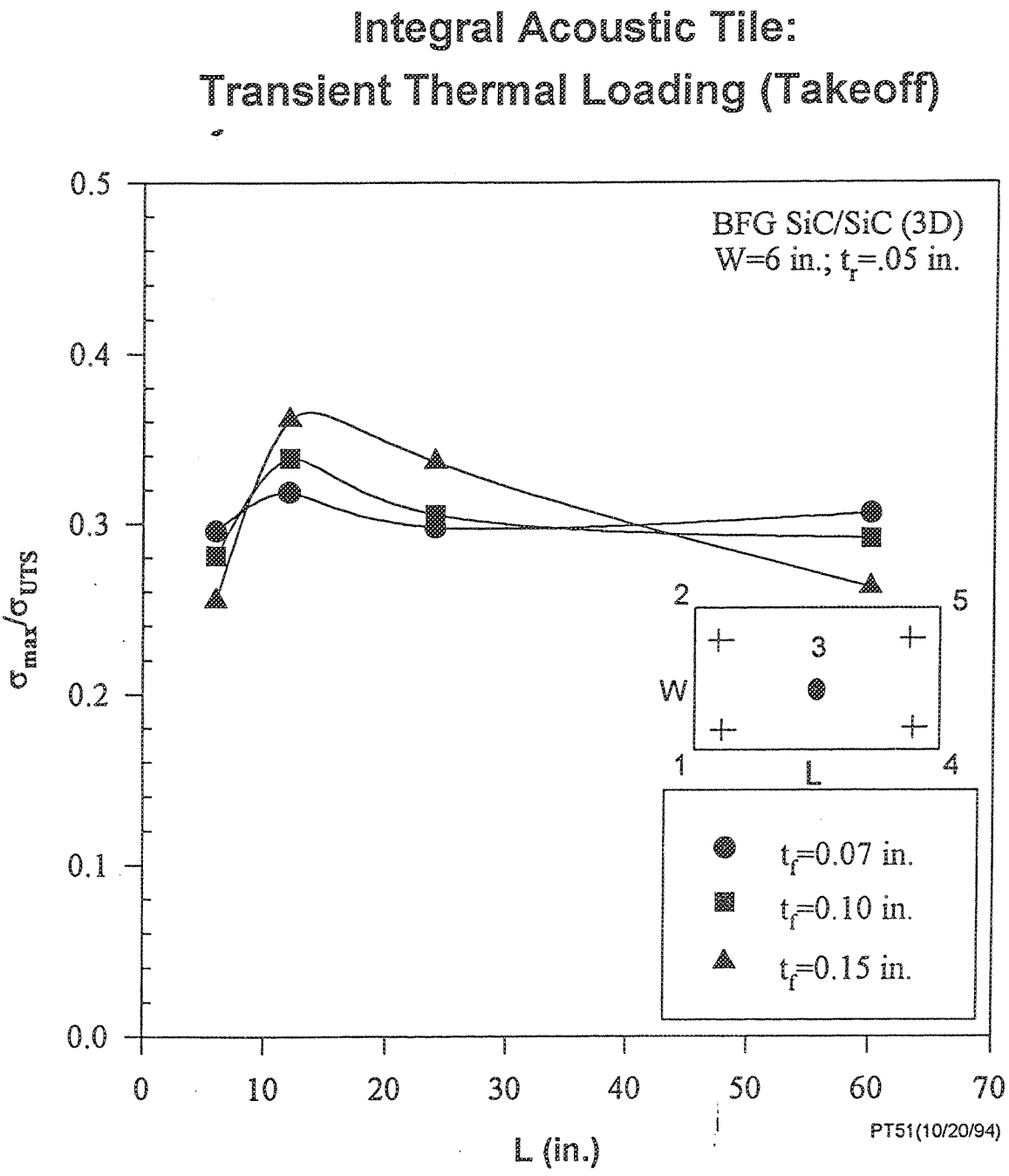
Integral Acoustic Tile:
Transient Thermal Loading (Takeoff)
BFG SiC/SiC (3D)
W=6 in.; t_r=.05 in.
σ_max/σ_UTS
0.5
0.4
0.3
0.2
0.1
0.0
0
10
20
30
40
50
60
70
L (in.)
2
5
3
W
1
L
4
t_f=0.07 in.
t_f=0.10 in.
t_f=0.15 in.
PT51(10/20/94)

Figure 25.

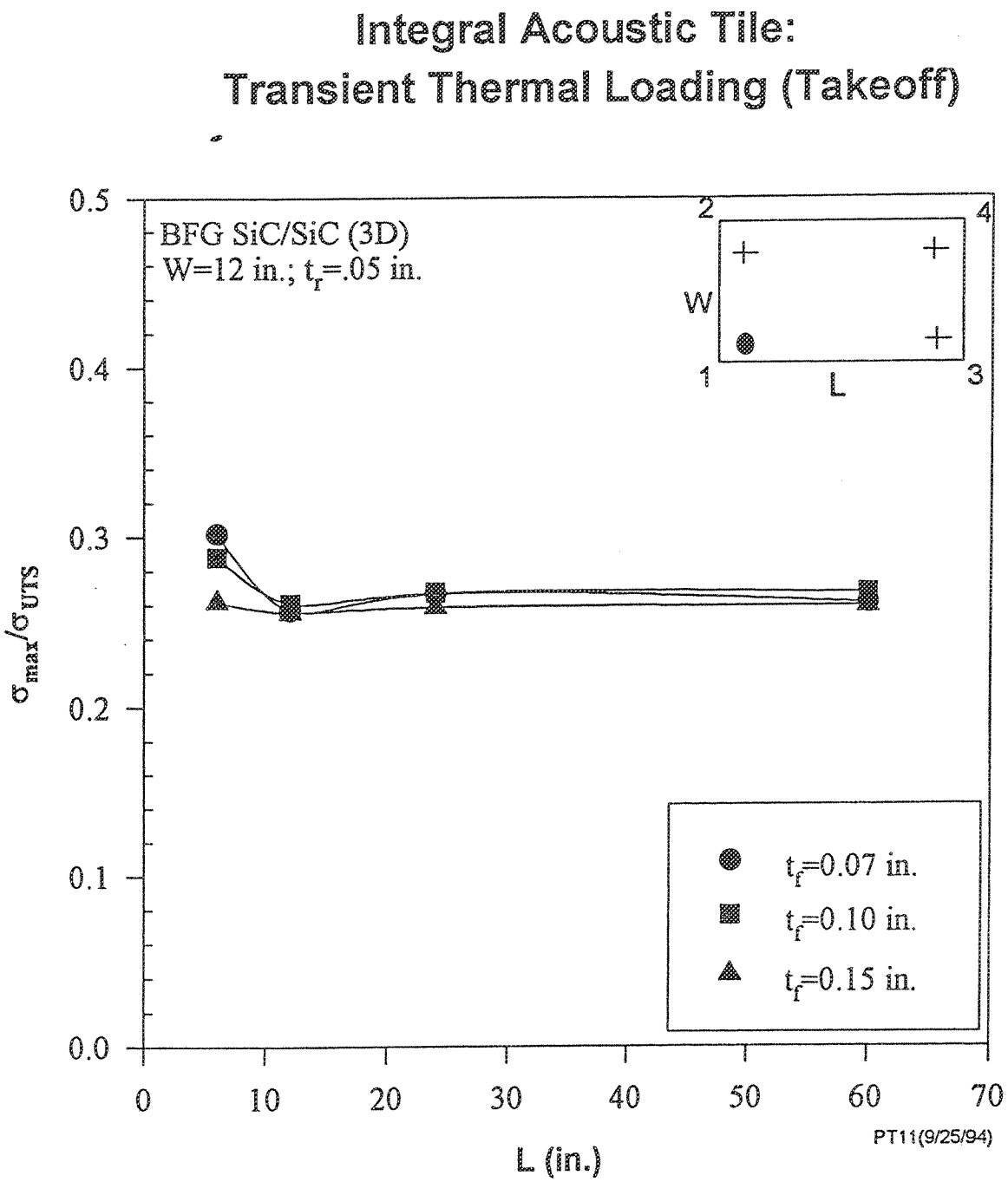
Integral Acoustic Tile:
Transient Thermal Loading (Takeoff)
BFG SiC/SiC (3D)
W=12 in.; t_r=.05 in.
2
4
W
1
L
3
0.5
0.4
0.3
0.2
0.1
0.0
$\sigma_{max}/\sigma_{UTS}$
t_f=0.07 in.
t_f=0.10 in.
t_f=0.15 in.
0
10
20
30
40
50
60
70
L (in.)
PT11(9/25/94)

Figure 26.

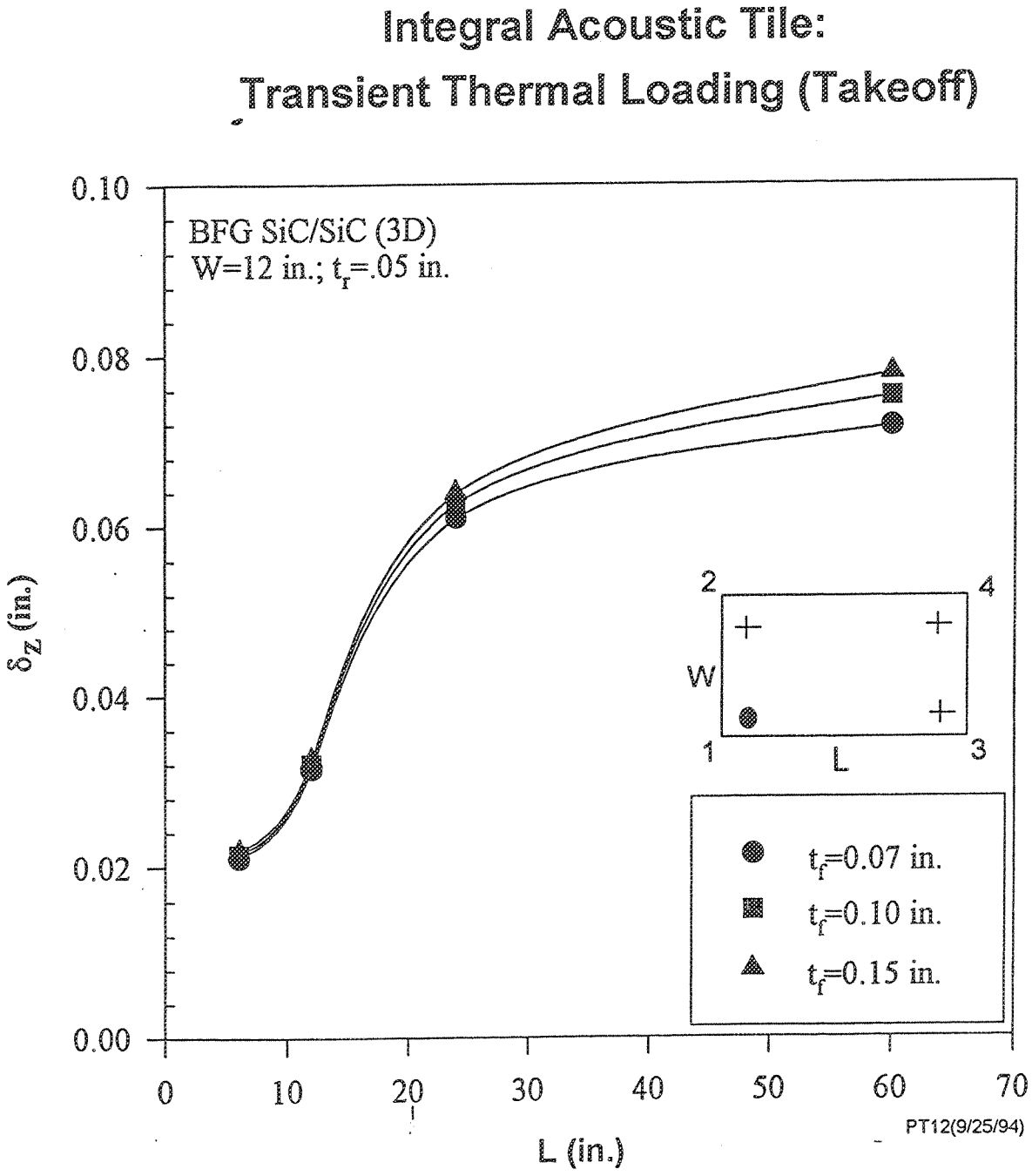
Integral Acoustic Tile:
Transient Thermal Loading (Takeoff)
BFG SiC/SiC (3D)
W=12 in.; t_r=.05 in.
δ_Z (in.)
0.10
0.08
0.06
0.04
0.02
0.00
0
10
20
30
40
50
60
70
L (in.)
2
4
W
1
L
3
t_f=0.07 in.
t_f=0.10 in.
t_f=0.15 in.
PT12(9/25/94)

Figure 27.

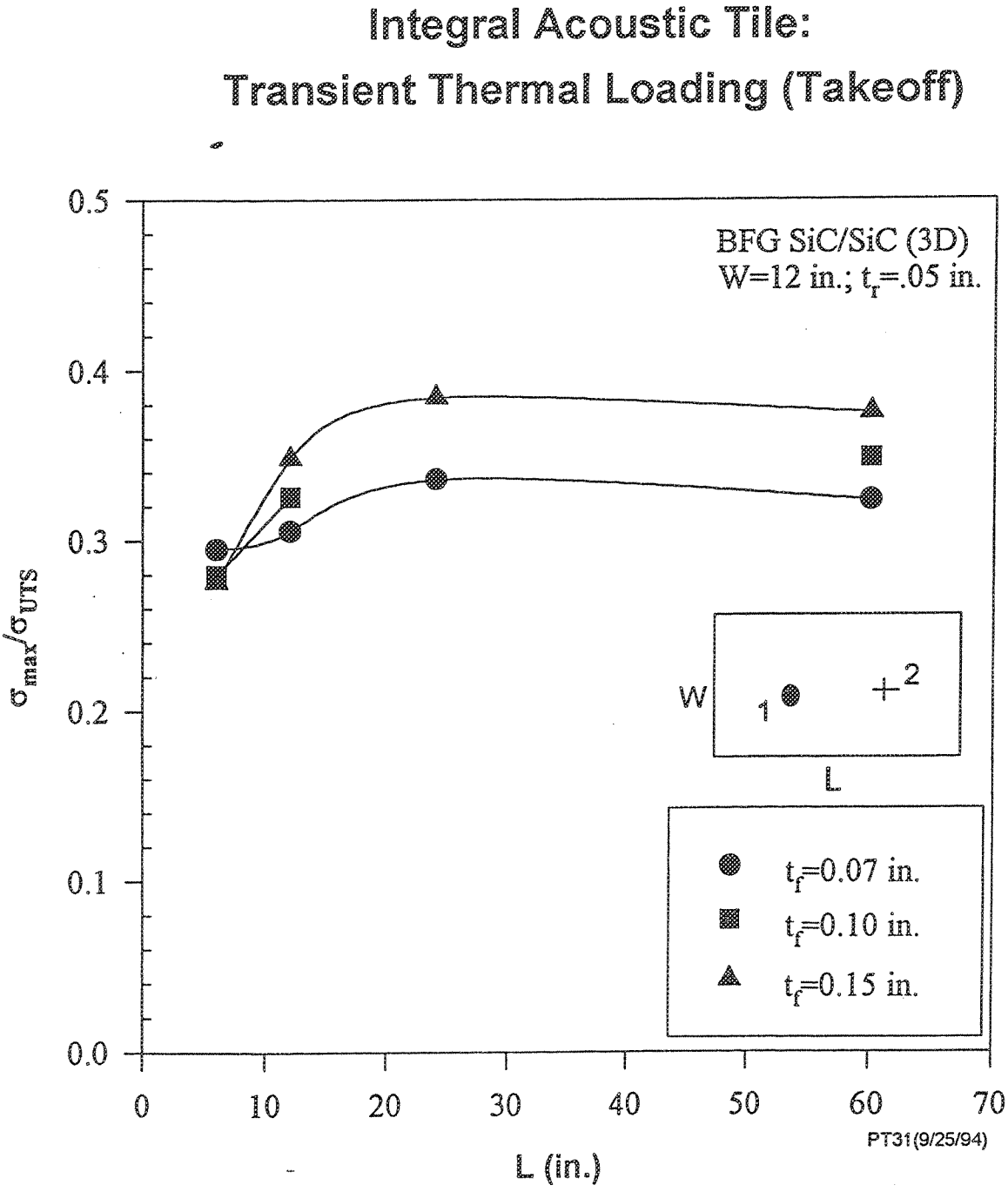
Integral Acoustic Tile:
Transient Thermal Loading (Takeoff)
BFG SiC/SiC (3D)
W=12 in.; t_r=.05 in.
$\sigma_{max}/\sigma_{UTS}$
0.5
0.4
0.3
0.2
0.1
0.0
0
10
20
30
40
50
60
70
L (in.)
W
1
2
L
t_f=0.07 in.
t_f=0.10 in.
t_f=0.15 in.
PT31(9/25/94)

Figure 28.

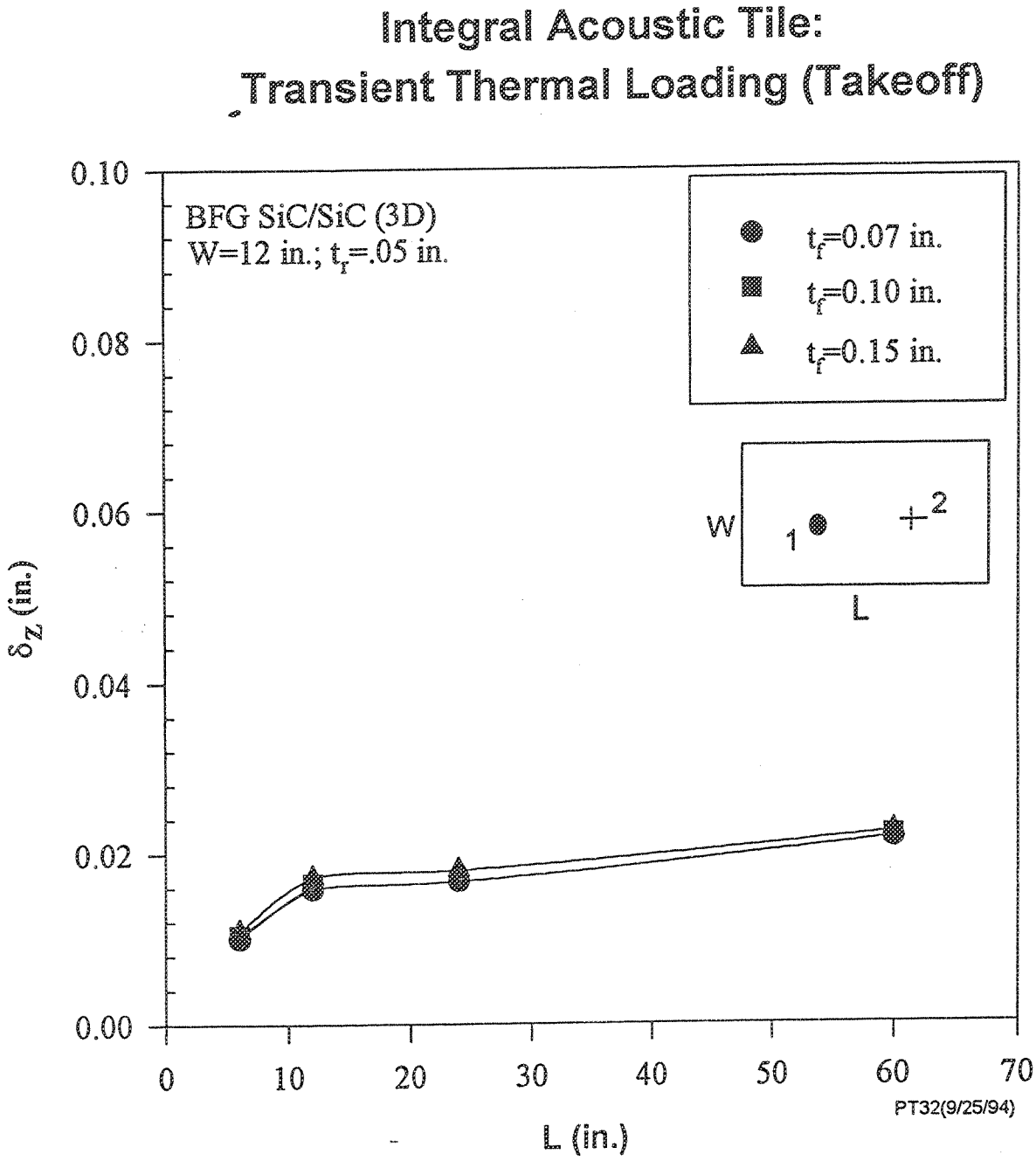
Integral Acoustic Tile:
Transient Thermal Loading (Takeoff)
BFG SiC/SiC (3D)
W=12 in.; t_r=.05 in.
t_f=0.07 in.
t_f=0.10 in.
t_f=0.15 in.
W
1
2
L
δ_Z (in.)
0.10
0.08
0.06
0.04
0.02
0.00
0
10
20
30
40
50
60
70
L (in.)
PT32(9/25/94)

Figure 29.

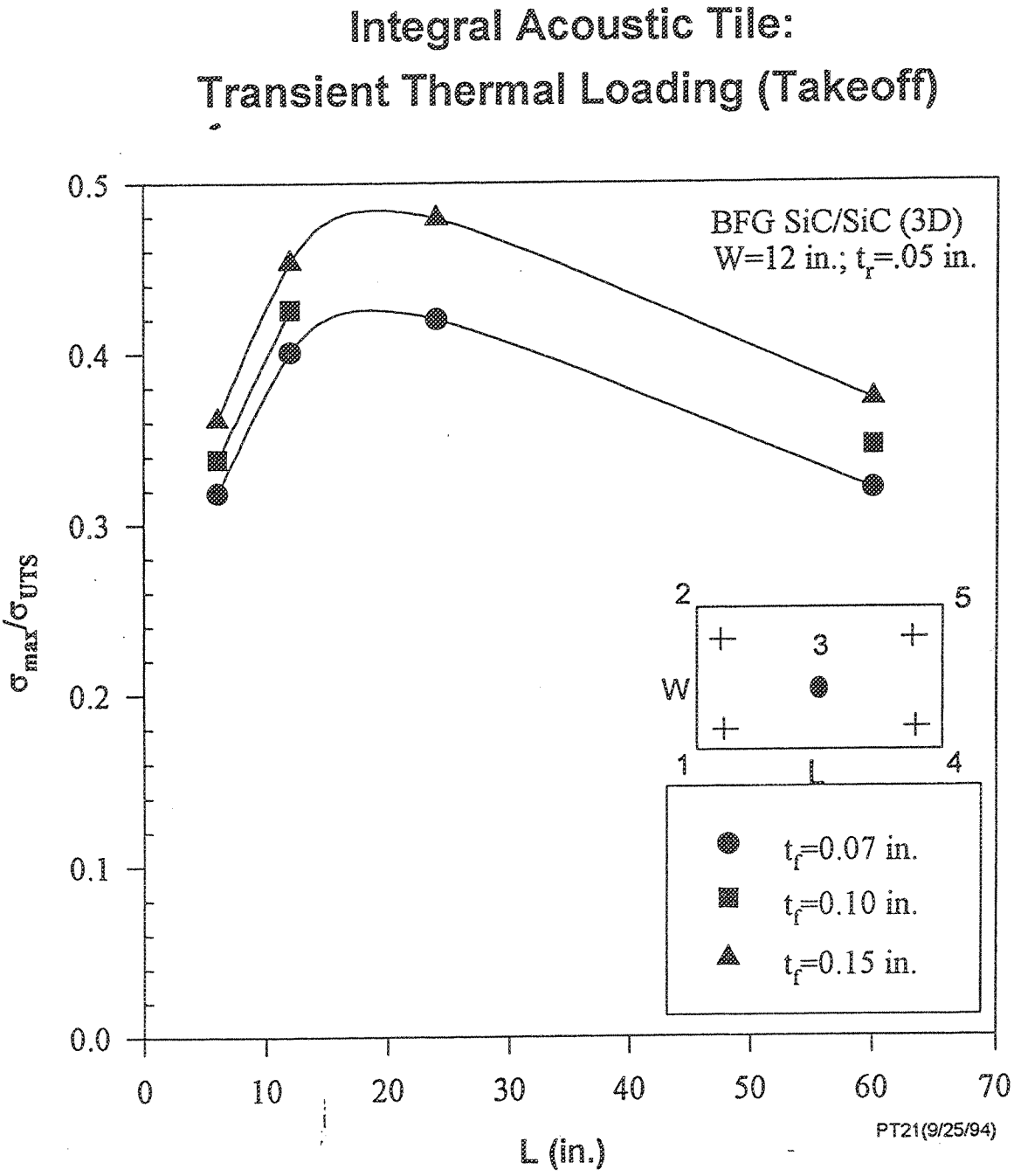
Integral Acoustic Tile:
Transient Thermal Loading (Takeoff)
BFG SiC/SiC (3D)
W=12 in.; t_r=.05 in.
$\sigma_{max}/\sigma_{UTS}$
L (in.)
0.0
0.1
0.2
0.3
0.4
0.5
0
10
20
30
40
50
60
70
1
2
3
4
5
W
L
t_f=0.07 in.
t_f=0.10 in.
t_f=0.15 in.
PT21(9/25/94)

Figure 30.

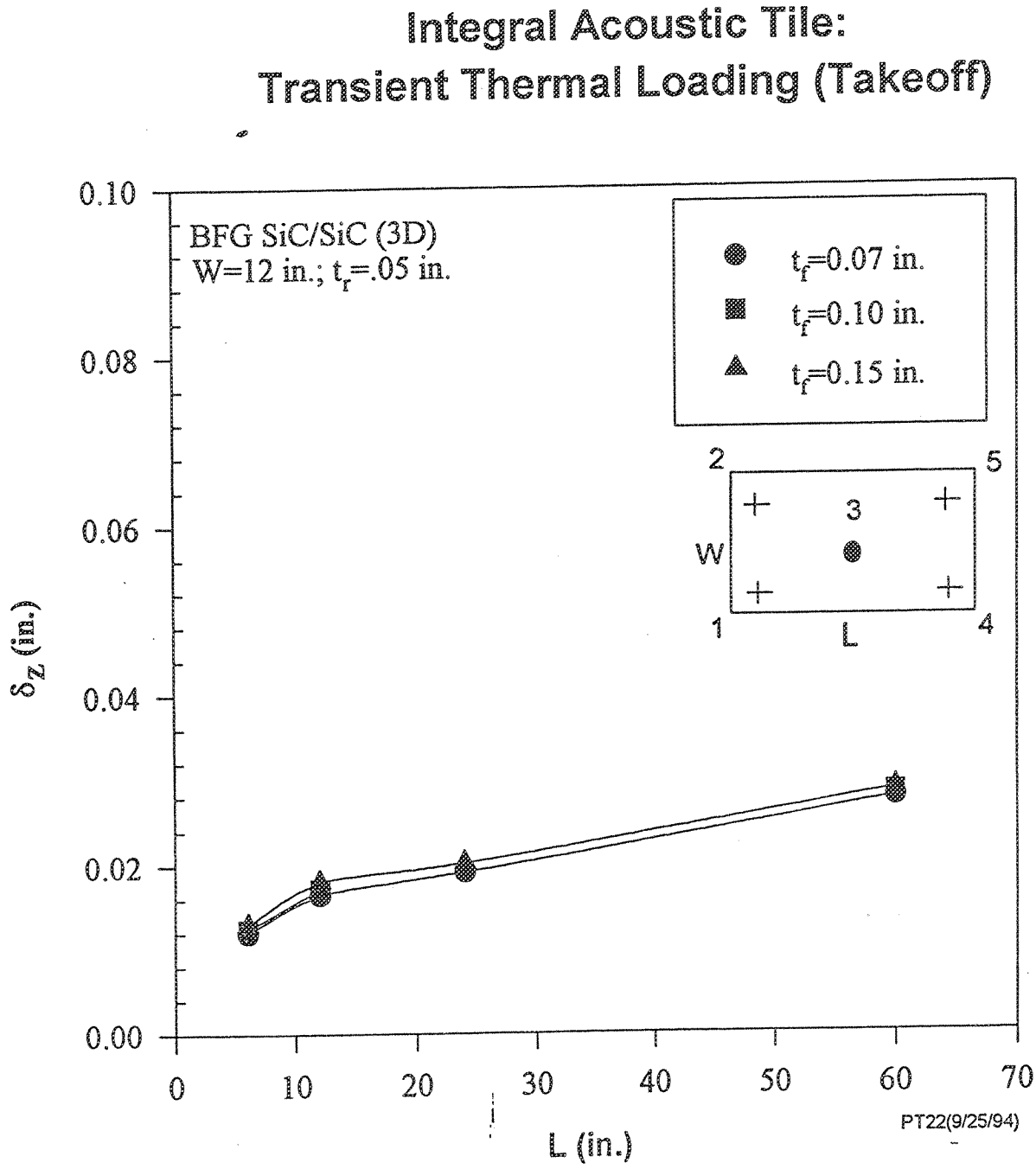
Integral Acoustic Tile:
Transient Thermal Loading (Takeoff)
BFG SiC/SiC (3D)
W=12 in.; t_r=.05 in.
t_f=0.07 in.
t_f=0.10 in.
t_f=0.15 in.
2
5
3
W
1
L
4
δ_z (in.)
0.10
0.08
0.06
0.04
0.02
0.00
0
10
20
30
40
50
60
70
L (in.)
PT22(9/25/94)

Figure 31.

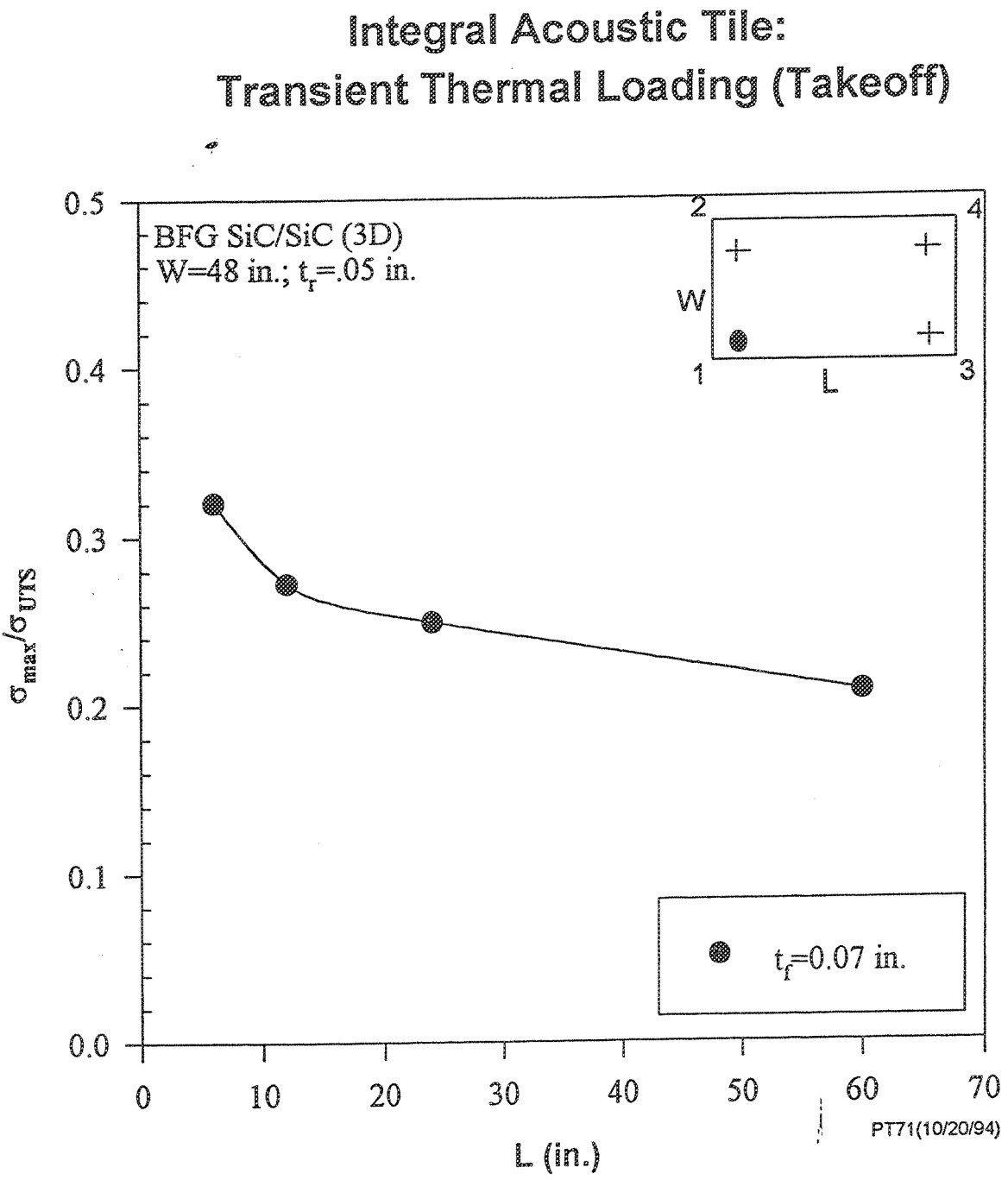
Integral Acoustic Tile:
Transient Thermal Loading (Takeoff)
BFG SiC/SiC (3D)
W=48 in.; t_r=.05 in.
2
4
W
1
L
3
0.5
0.4
0.3
0.2
0.1
0.0
$\sigma_{max}/\sigma_{UTS}$
t_f=0.07 in.
0
10
20
30
40
50
60
70
L (in.)
PT71(10/20/94)

Figure 32.

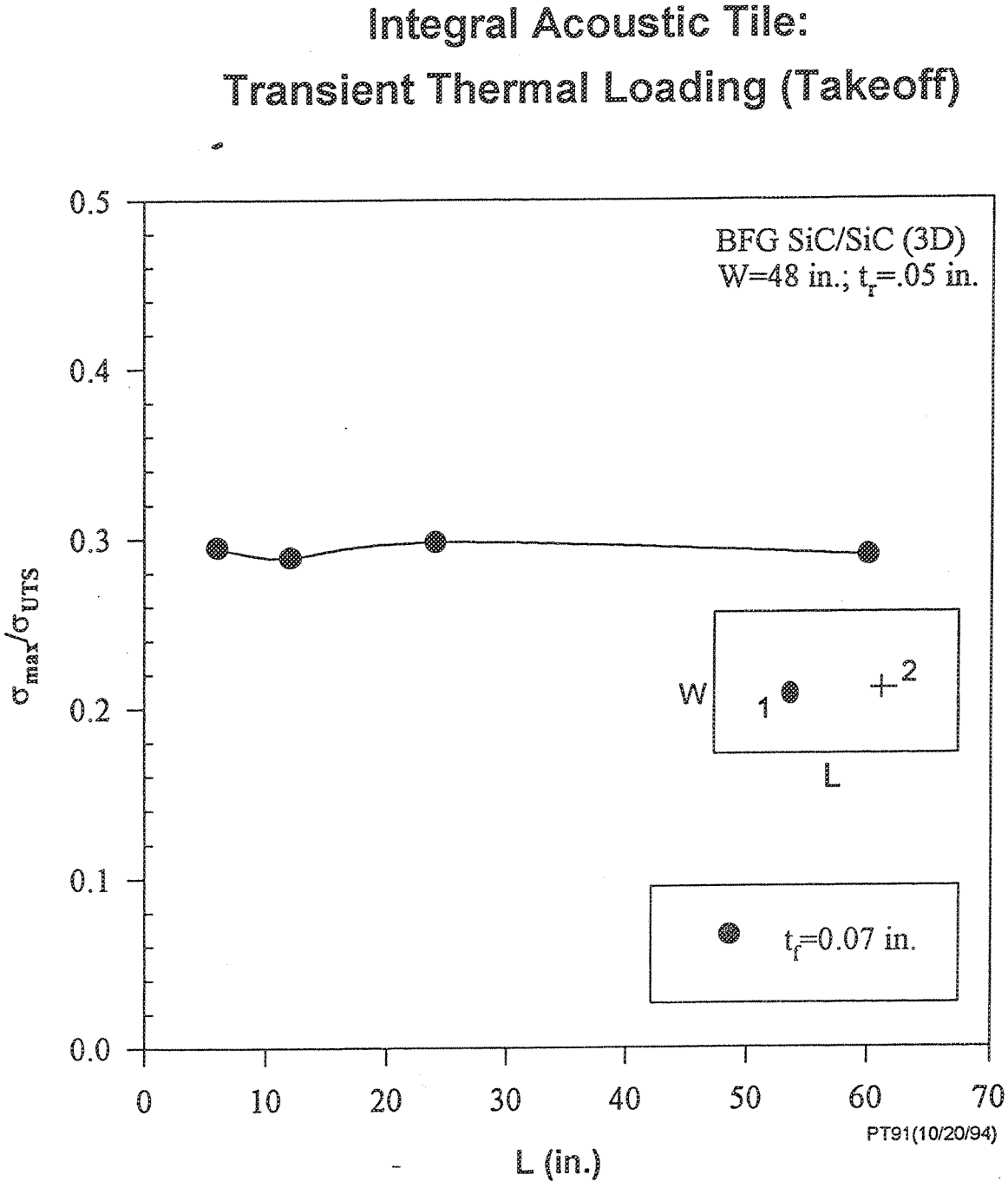
Integral Acoustic Tile:
Transient Thermal Loading (Takeoff)
BFG SiC/SiC (3D)
W=48 in.; t_r=.05 in.
$\sigma_{max}/\sigma_{UTS}$
0.5
0.4
0.3
0.2
0.1
0.0
0
10
20
30
40
50
60
70
L (in.)
W
L
1
2
t_f=0.07 in.
PT91(10/20/94)

Figure 33.

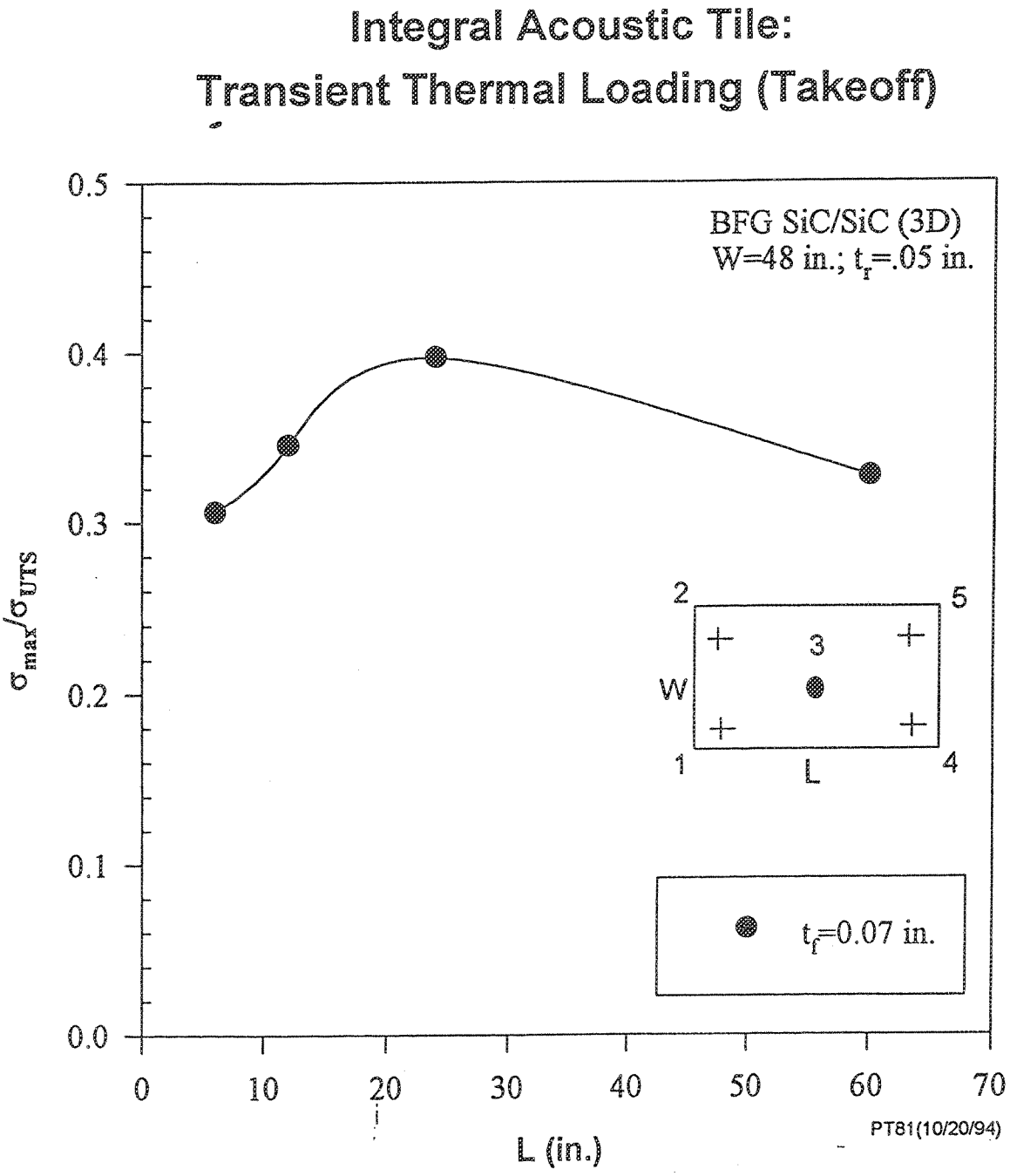
Integral Acoustic Tile:
Transient Thermal Loading (Takeoff)
BFG SiC/SiC (3D)
W=48 in.; t_r=.05 in.
$\sigma_{max}/\sigma_{UTS}$
0.5
0.4
0.3
0.2
0.1
0.0
0
10
20
30
40
50
60
70
L (in.)
2
5
3
W
1
L
4
t_f=0.07 in.
PT81(10/20/94)

Figure 34.

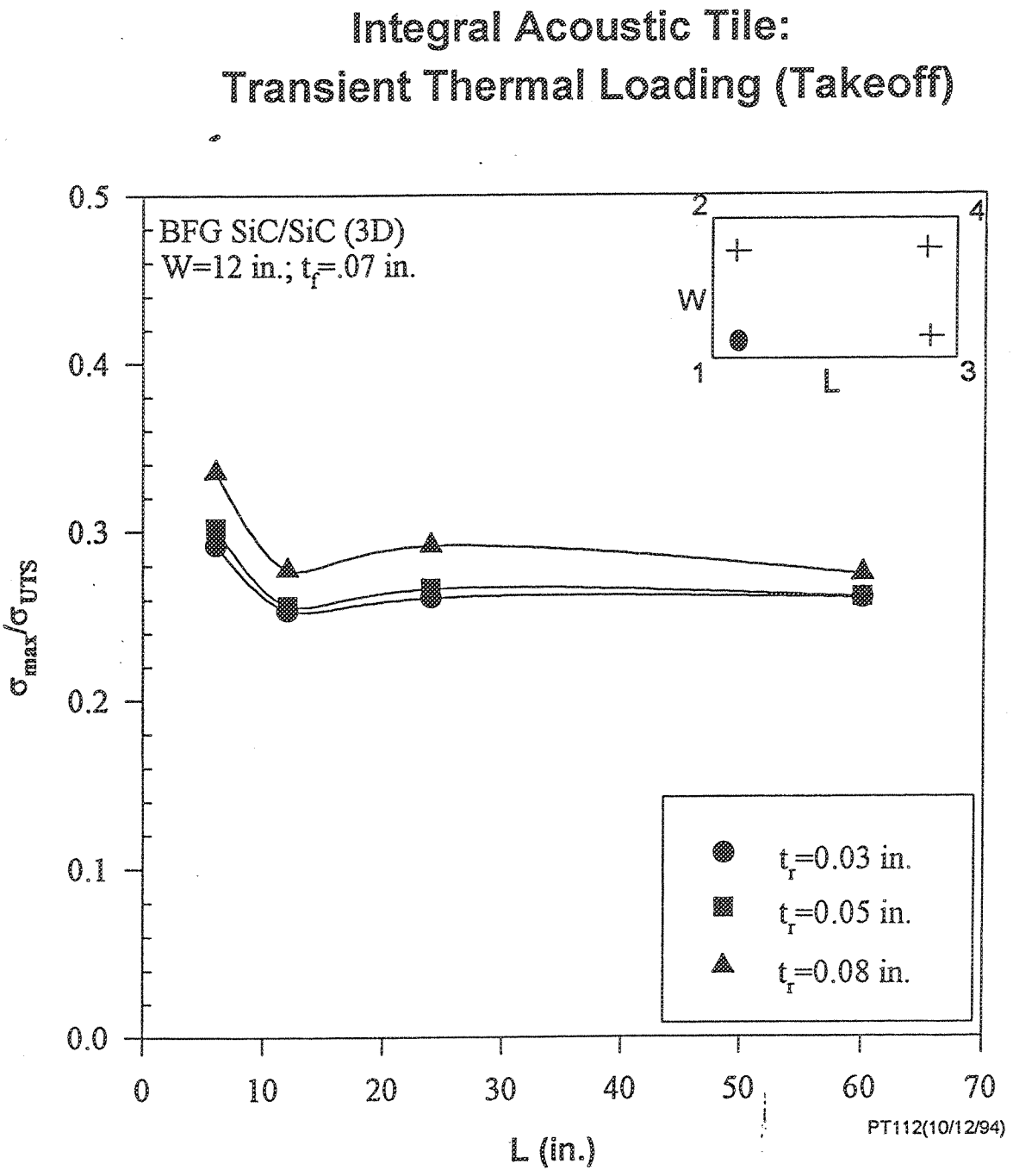
Integral Acoustic Tile:
Transient Thermal Loading (Takeoff)
BFG SiC/SiC (3D)
W=12 in.; t_f=.07 in.
2
4
W
1
L
3
0.5
0.4
0.3
0.2
0.1
0.0
$\sigma_{max}/\sigma_{UTS}$
t_r=0.03 in.
t_r=0.05 in.
t_r=0.08 in.
0
10
20
30
40
50
60
70
L (in.)
PT112(10/12/94)

Figure 35.

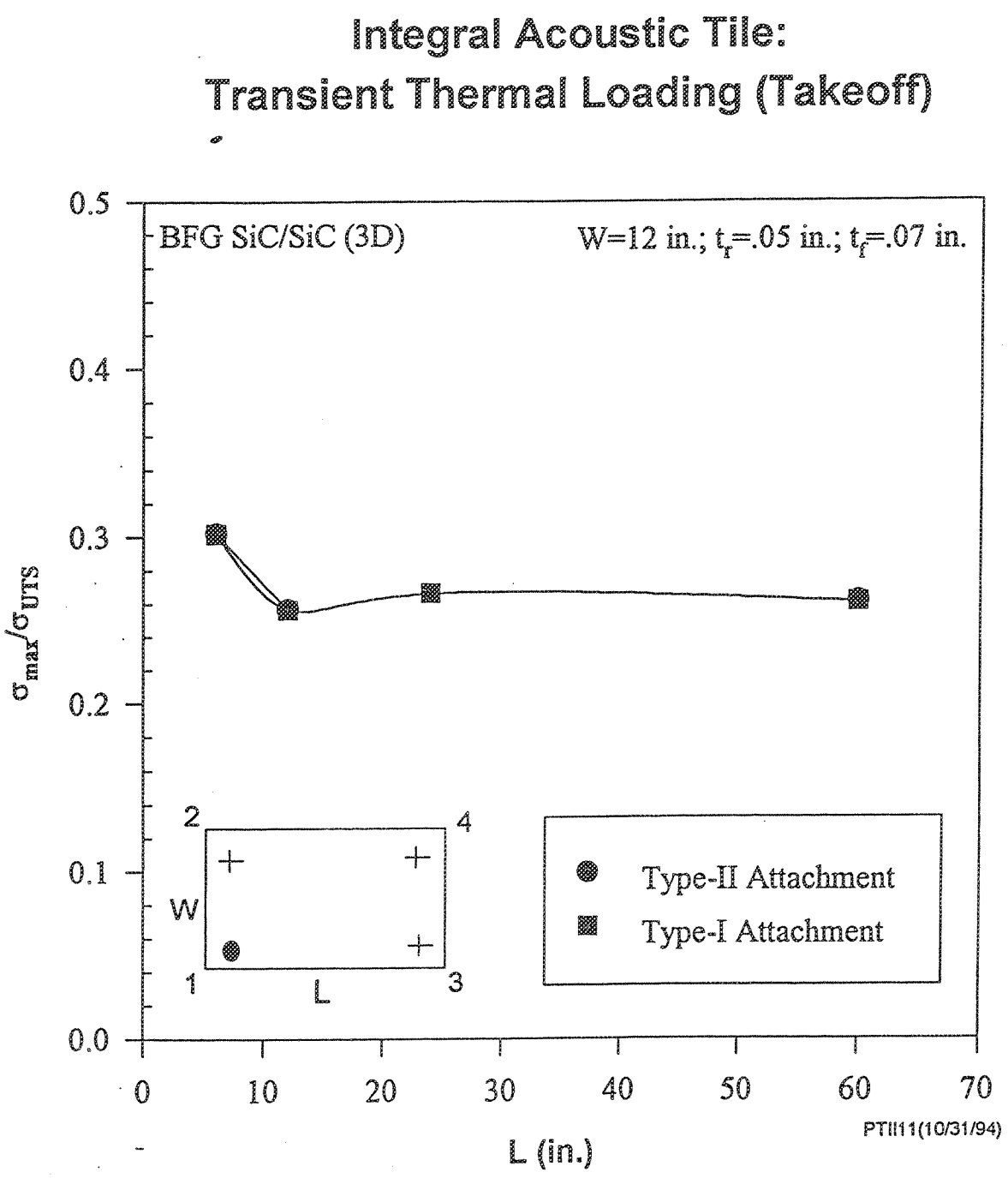
Integral Acoustic Tile:
Transient Thermal Loading (Takeoff)
BFG SiC/SiC (3D)
W=12 in.; t_r=.05 in.; t_f=.07 in.
$\sigma_{max}/\sigma_{UTS}$
0.5
0.4
0.3
0.2
0.1
0.0
0
10
20
30
40
50
60
70
L (in.)
2
4
W
1
L
3
Type-II Attachment
Type-I Attachment
PTII11(10/31/94)

Figure 36.

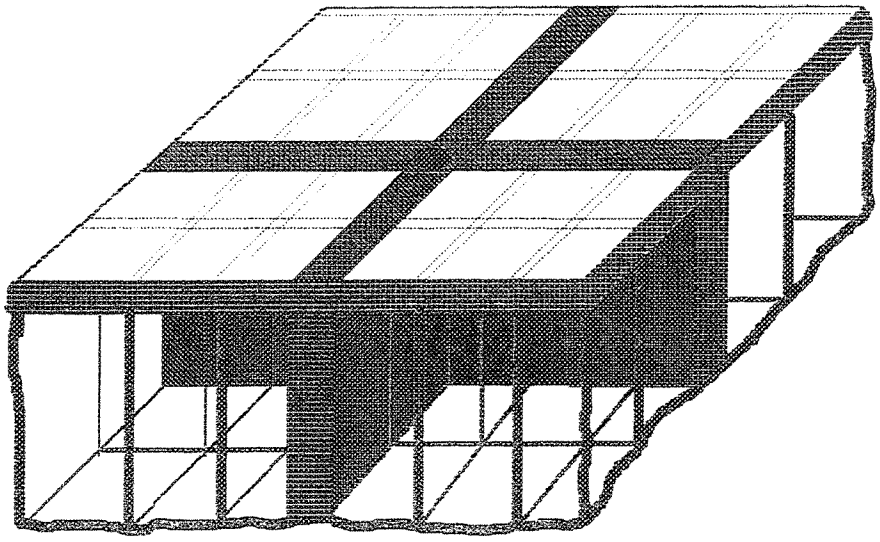

Schematic Cross Sectional View of Rib Stiffened Part-Integral CMC Acoustic Liner Tile Concept

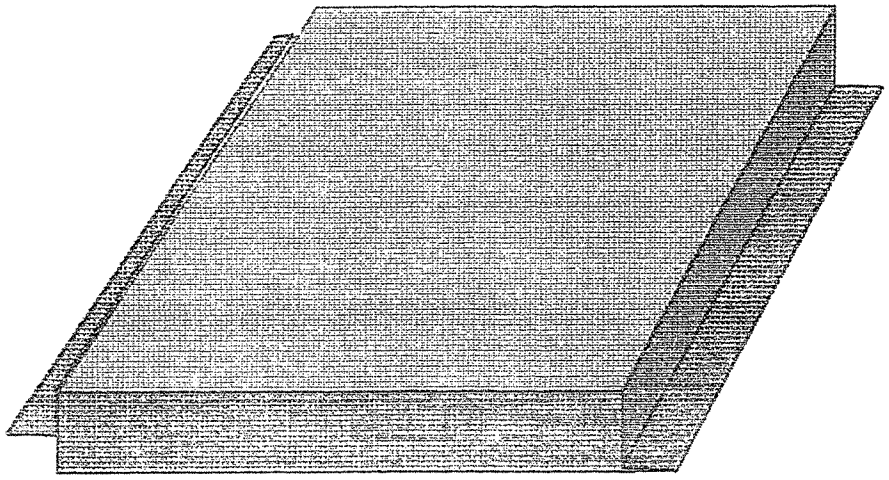

Proposed CMC Tile

Figure 37. Schematic views of a new tile design concept.

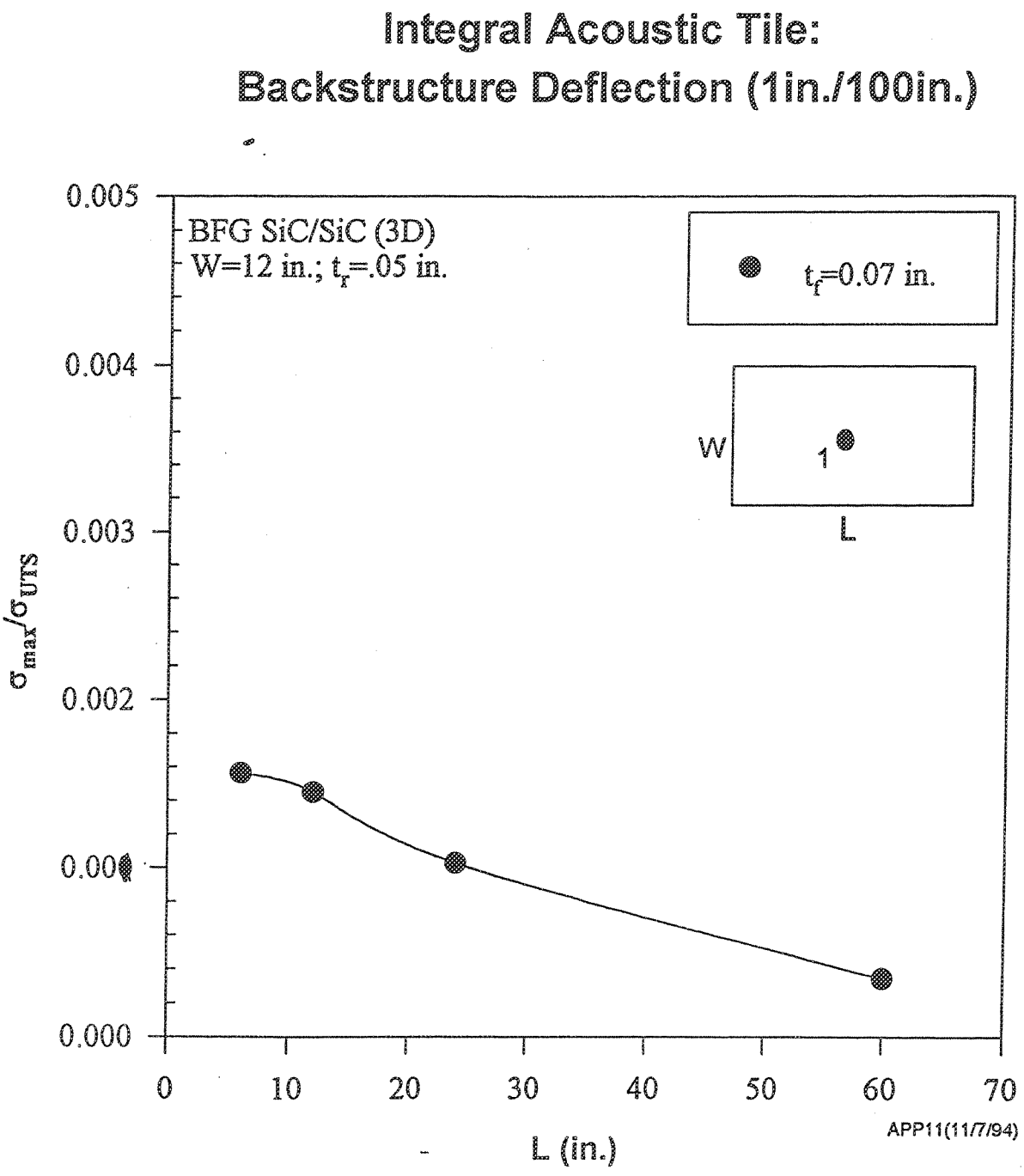
Integral Acoustic Tile:
Backstructure Deflection (1in./100in.)
BFG SiC/SiC (3D)
W=12 in.; t_r=.05 in.
t_f=0.07 in.
W
1
L
$\sigma_{max}/\sigma_{UTS}$
0.005
0.004
0.003
0.002
0.001
0.000
0
10
20
30
40
50
60
70
L (in.)
APP11(11/7/94)

Figure 38.

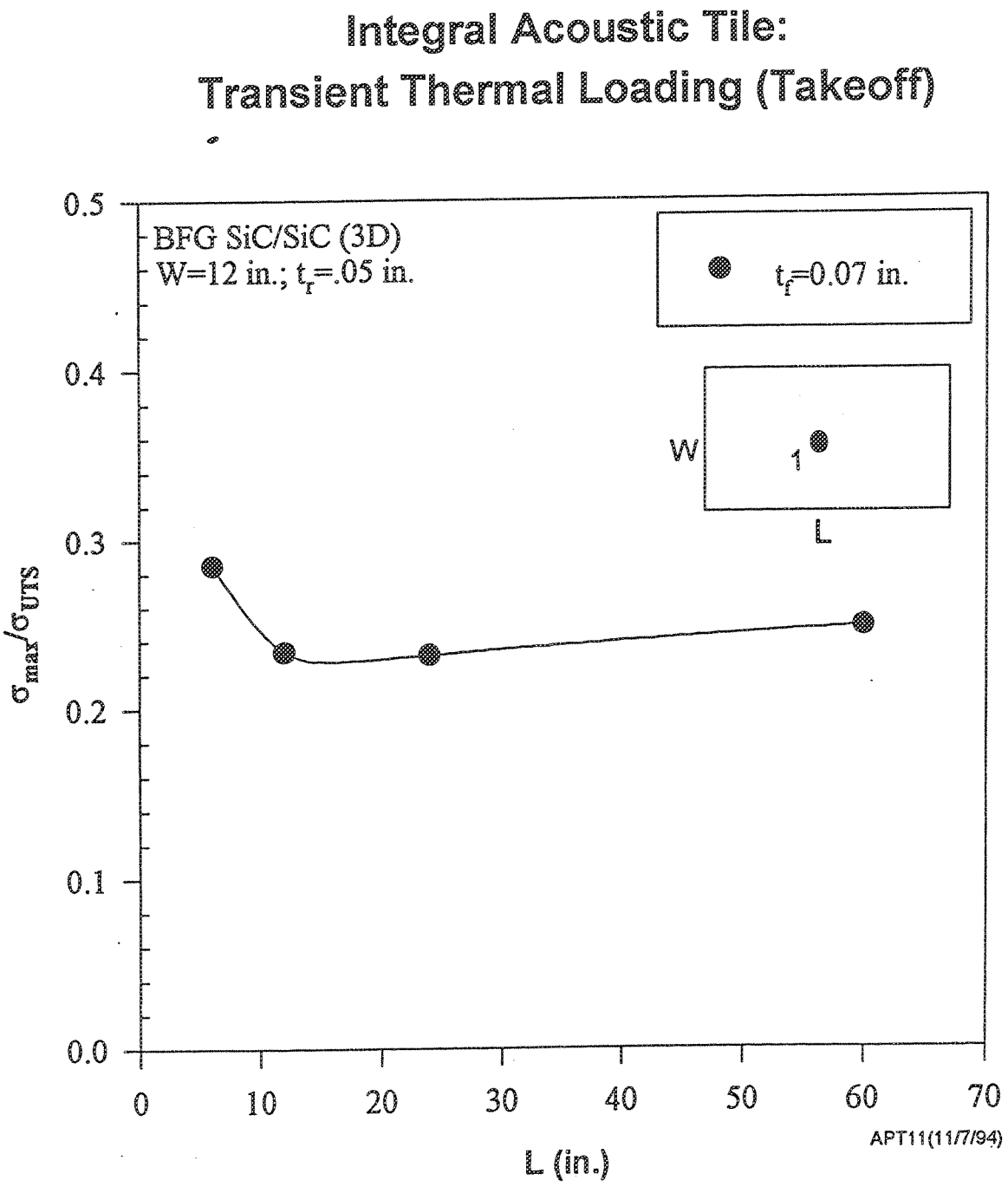
Integral Acoustic Tile:
Transient Thermal Loading (Takeoff)
BFG SiC/SiC (3D)
W=12 in.; t_r=.05 in.
t_f=0.07 in.
W
1
L
$\sigma_{max}/\sigma_{UTS}$
0.5
0.4
0.3
0.2
0.1
0.0
0
10
20
30
40
50
60
70
L (in.)
APT11(11/7/94)

Figure 39.

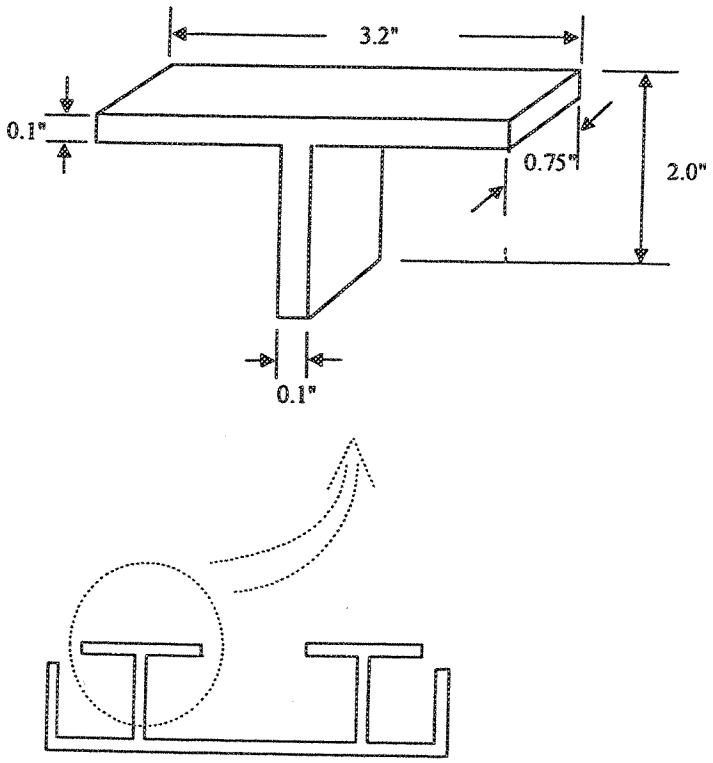

Figure 40. T-shaped joint in a nonintegral design of acoustic liner

Table 5. Four Candidate CMCs for T-Joints and Their Failure Loads

Ceramic Matrix Composite Material		Failure Load (lbs)
B.F. Goodrich 2D SiC/SiC Composite	Consists of ceramic grade (CG) Nicalon fiber, an interface coating, and a CVI SiC matrix; 2D fiber architecture	40.5
B.F. Goodrich 3D SiC/SiC composite	Same as BFG 2D material, except with 3D fiber architecture	58.2
Pratt & Whitney 3D Oxide/Oxide composite	A 3D form of Oxide/Oxide fabricated using a sol-gel process; consists of Nextel 720 fiber (Al_2O_3-SiO_2) and a sol-gel Al_2O_3 matrix	6.3
GE/Hexcel 2D Oxide/Oxide composite	A 2D Oxide/Oxide consisting of Nextel 720 fiber (Al_2O_3-SiO_2) and an aluminosilicate matrix	14.5 (radius=1/4") 13.2 (radius=1/8")

Table 6. Failure loads for various CMC integral T-joints in a tensile-flexural test

CMC Materials	Failure Load (lbs)
SiC/SiC 2D	40.5
SiC/SiC 3D	58.2
Oxide/Oxide 3D	6.3
Oxide/Oxide 2D (Radius=1/4")	14.5
Oxide/Oxide 2D (Radius=1/8")	13.2

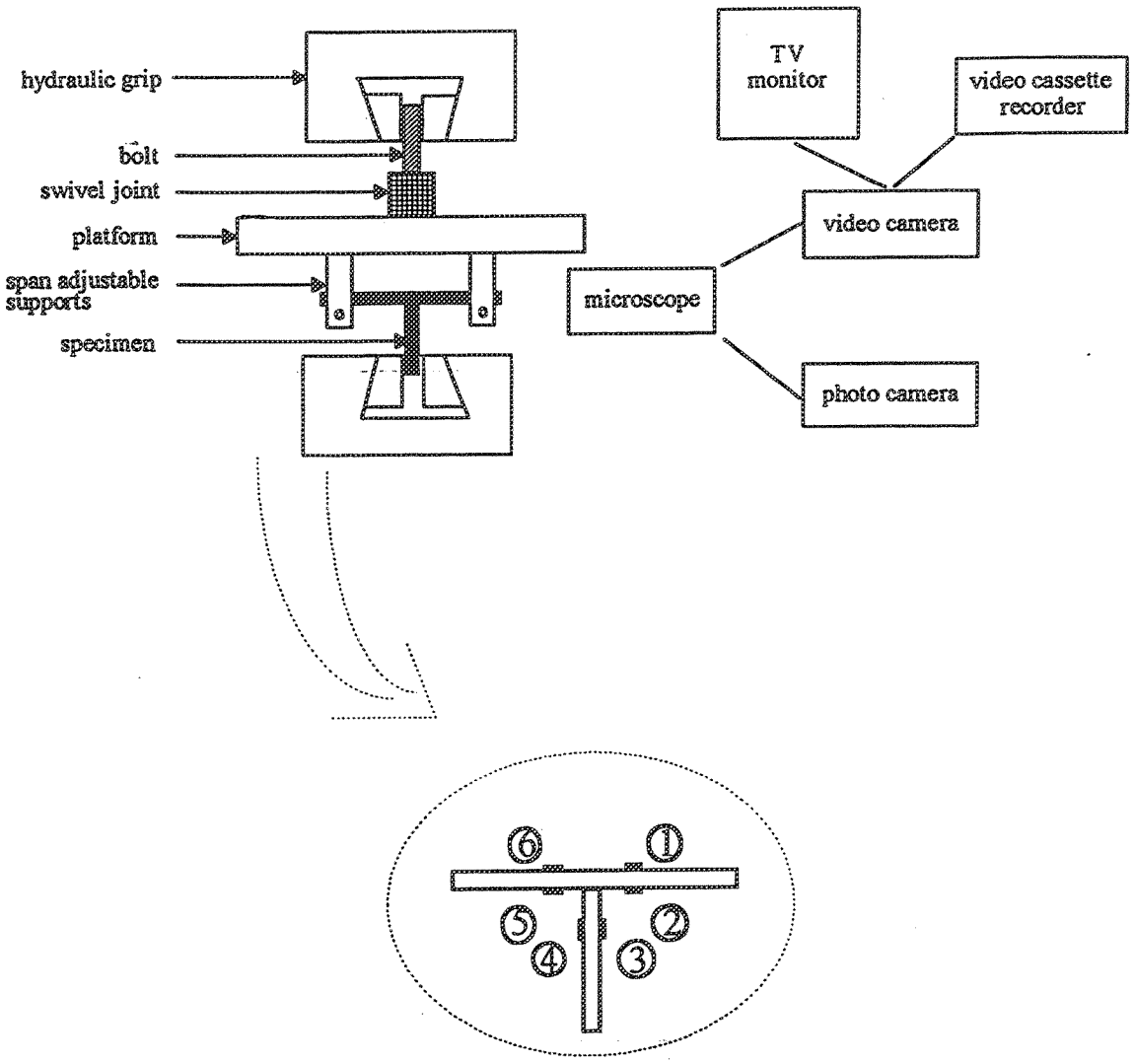

Figure 41. Tensile-flexural test setup for T-joints and the strain gage locations

(a)

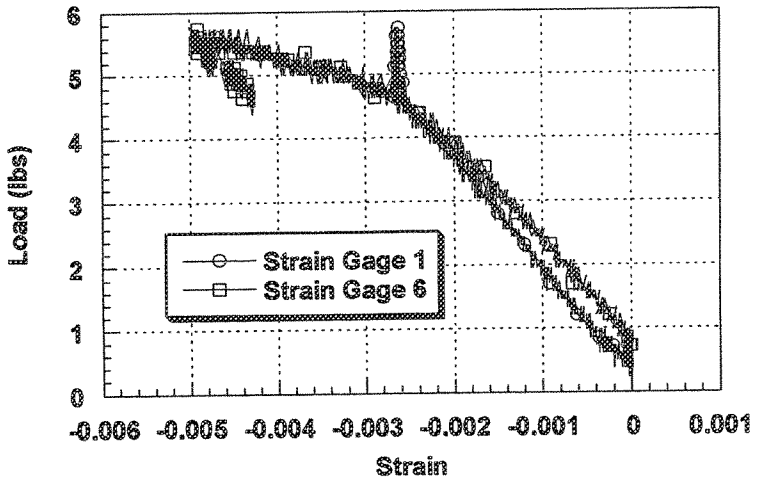

(b)

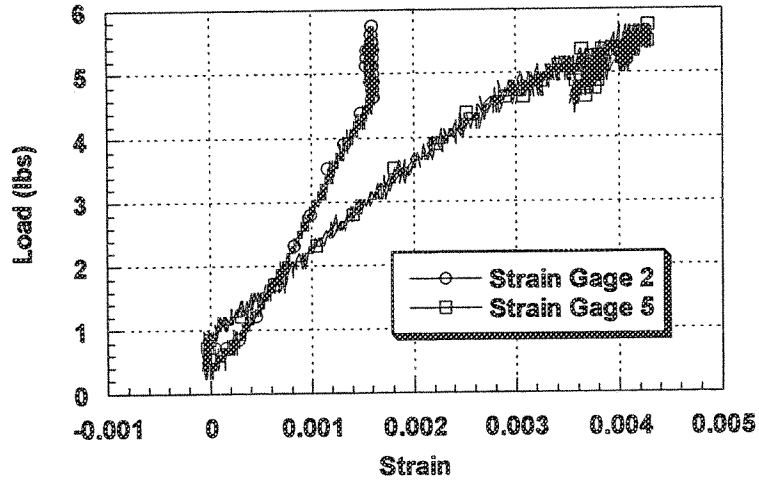

(c)

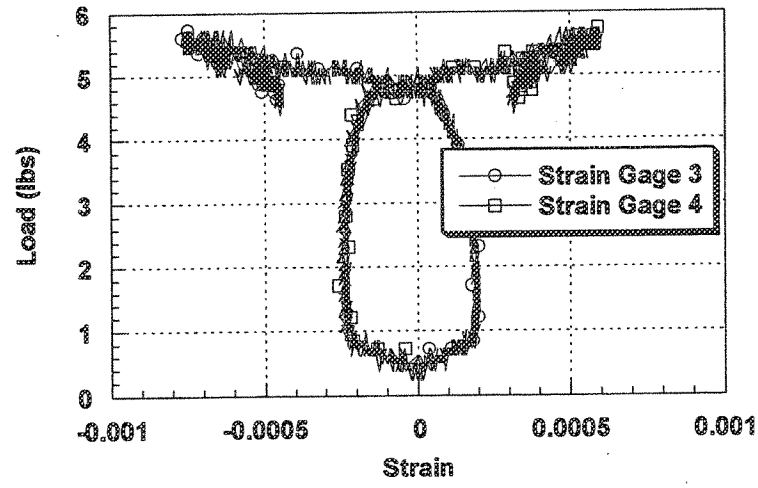

Figure 42. Strain data for an Oxide/Oxide 3D T-joint

(a)

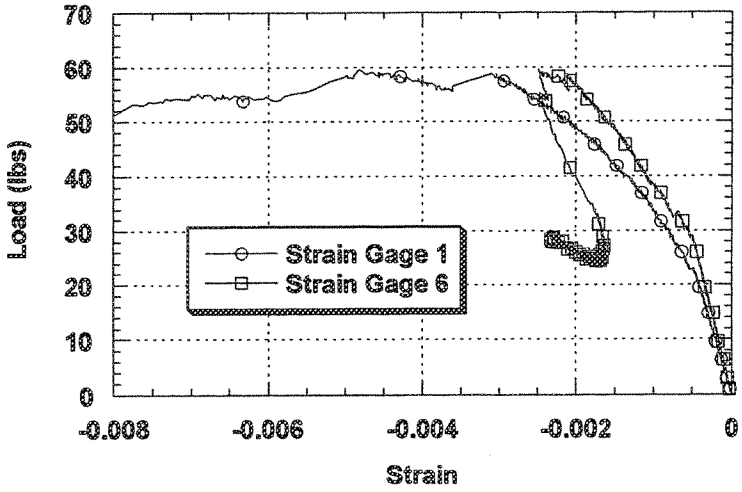

(b)

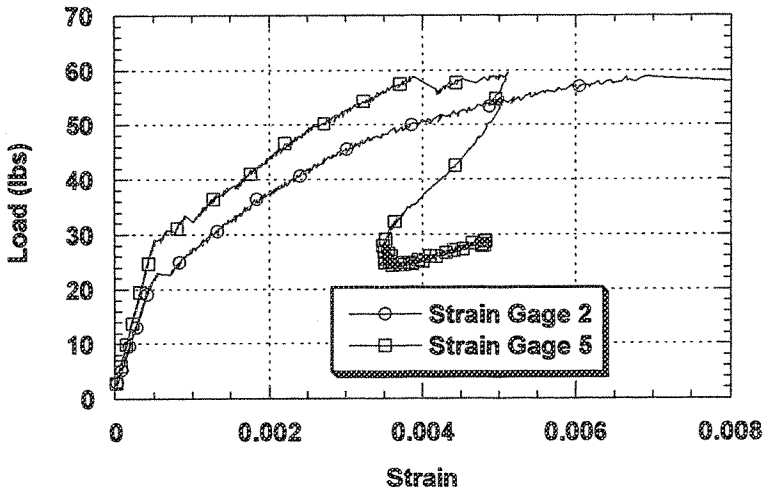

(c)

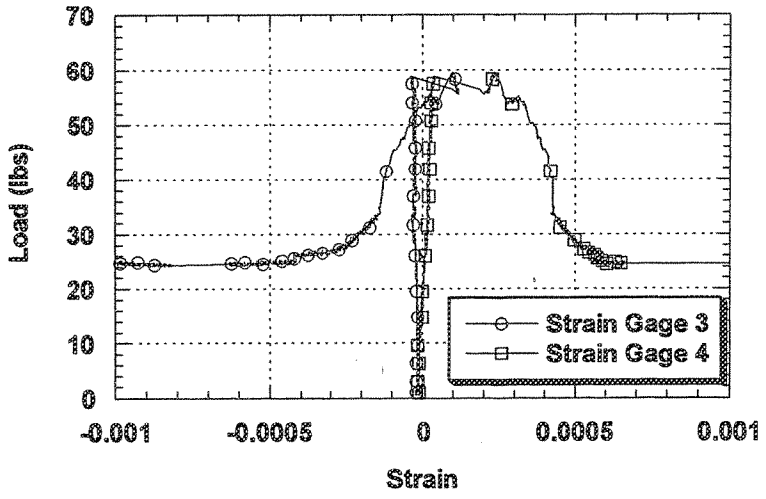

Figure 43. Strain data for a SiC/SiC 3D T-joint

(a)

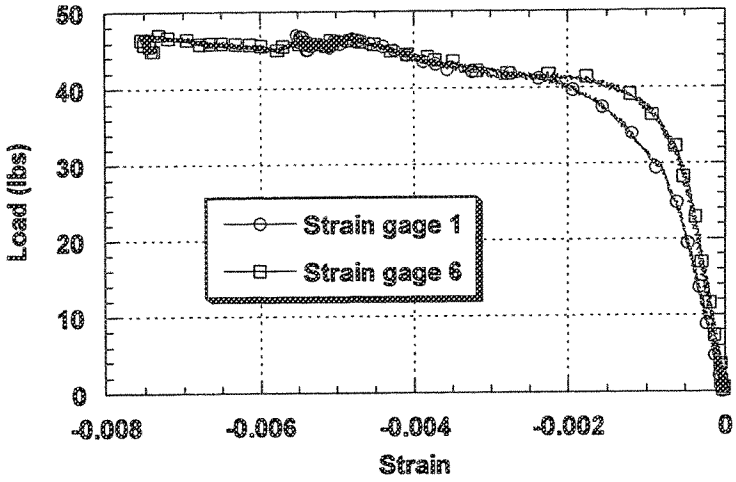

(b)

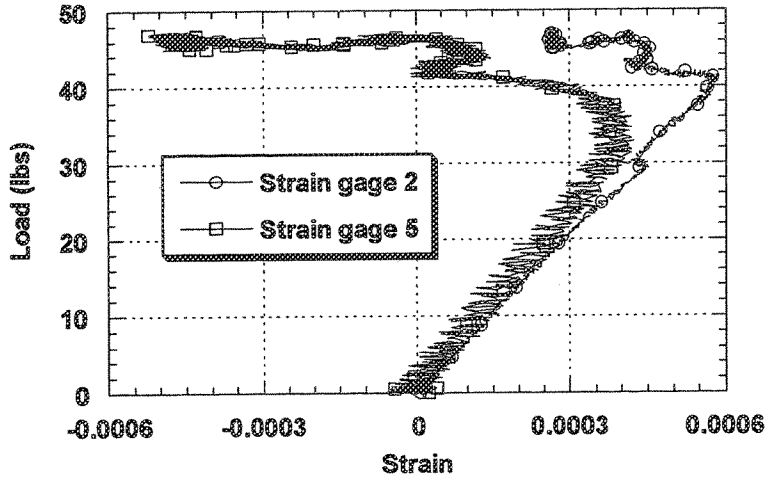

(c)

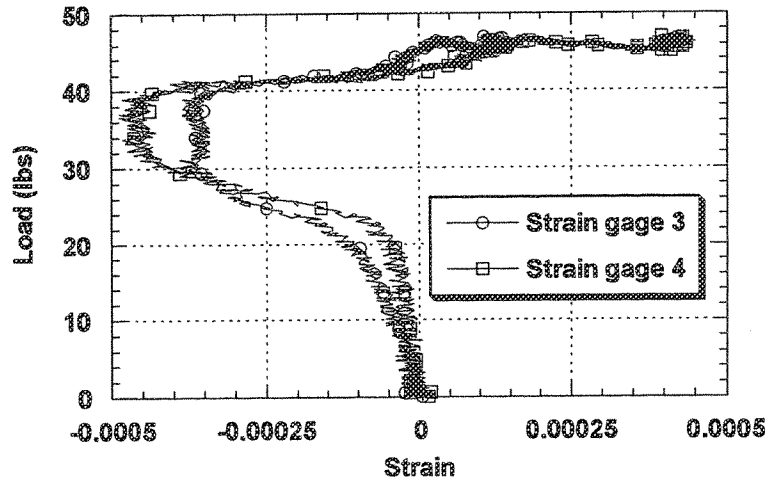

Figure 44. Strain data for a SiC/SiC 2D T-joint

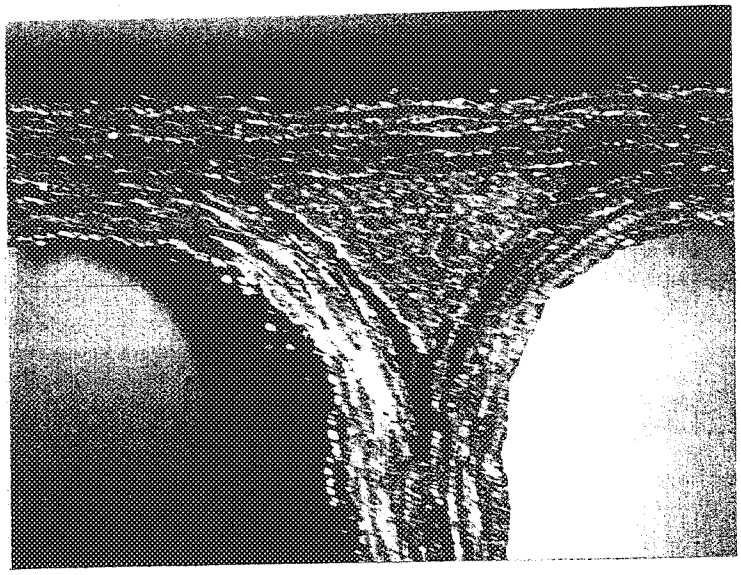

(a)

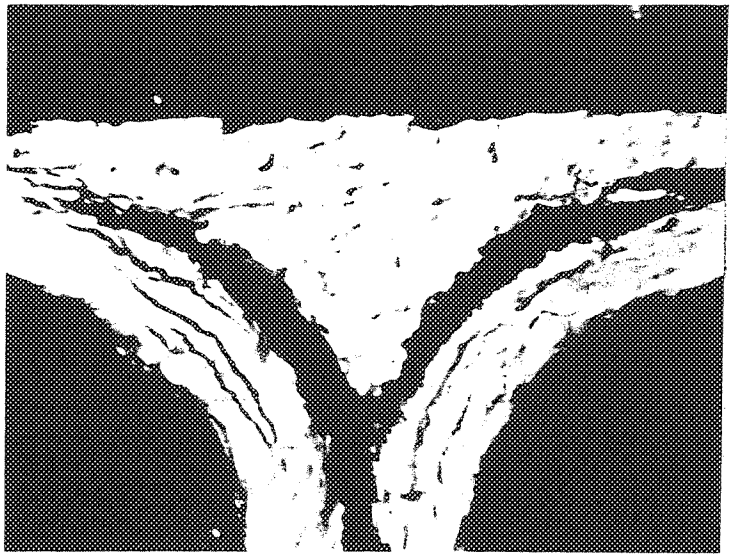

(b)

Figure 45. An imperfect T-joint before (a) and after (b) the tensile-flexural test

(a)

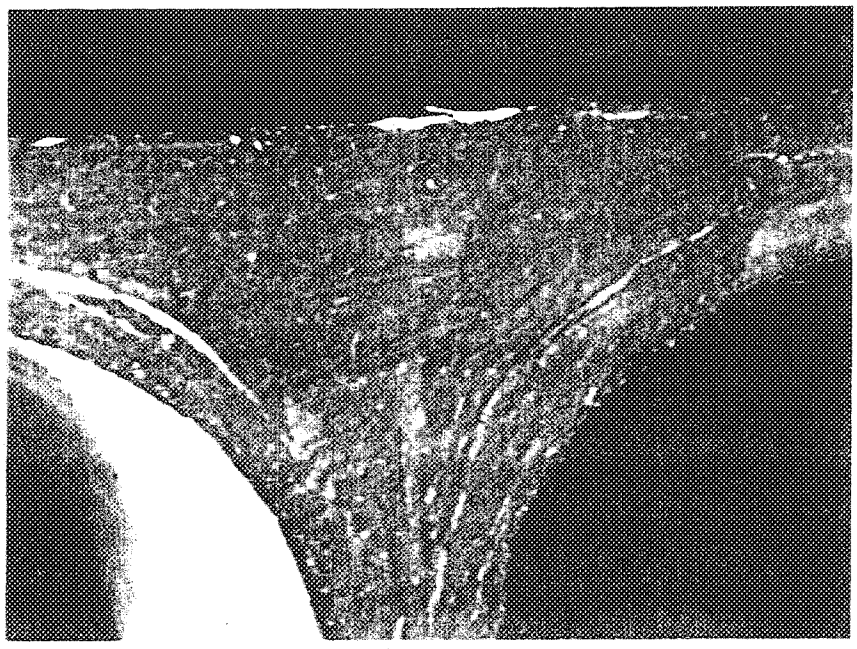

(b)

Figure 46. Delamination propagation at a GE/Hexcel 2D T-joint

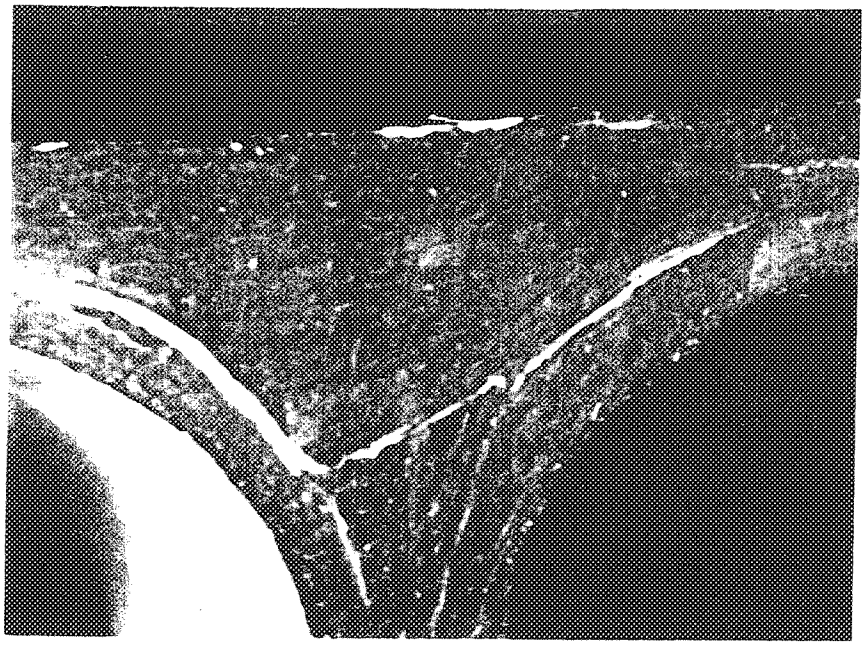

(c)

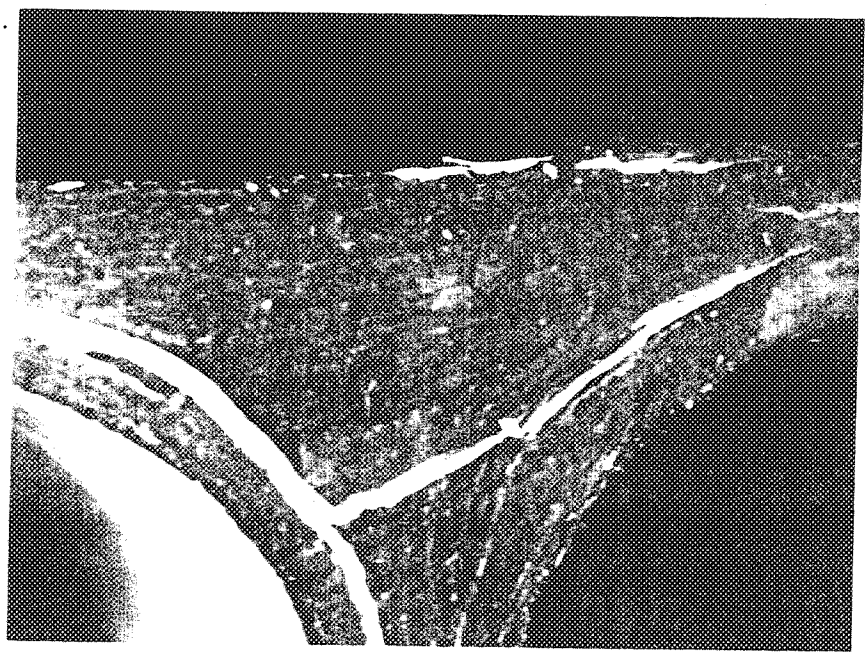

(d)

Figure 46. Delamination propagation at a GE/Hexcel 2D T-joint (continued)

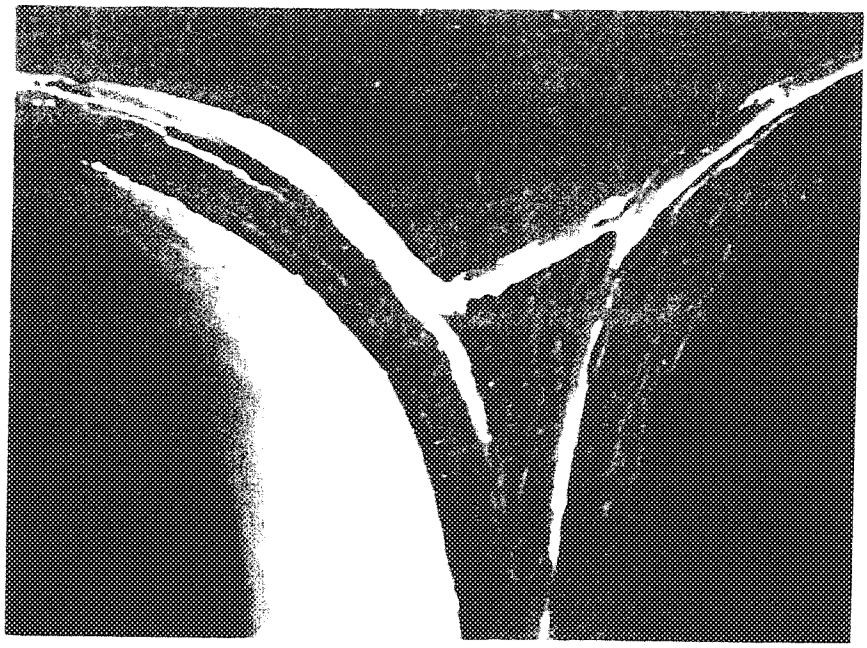

(e)

Figure 46. Delamination propagation at a GE/Hexcel 2D T-joint (continued)

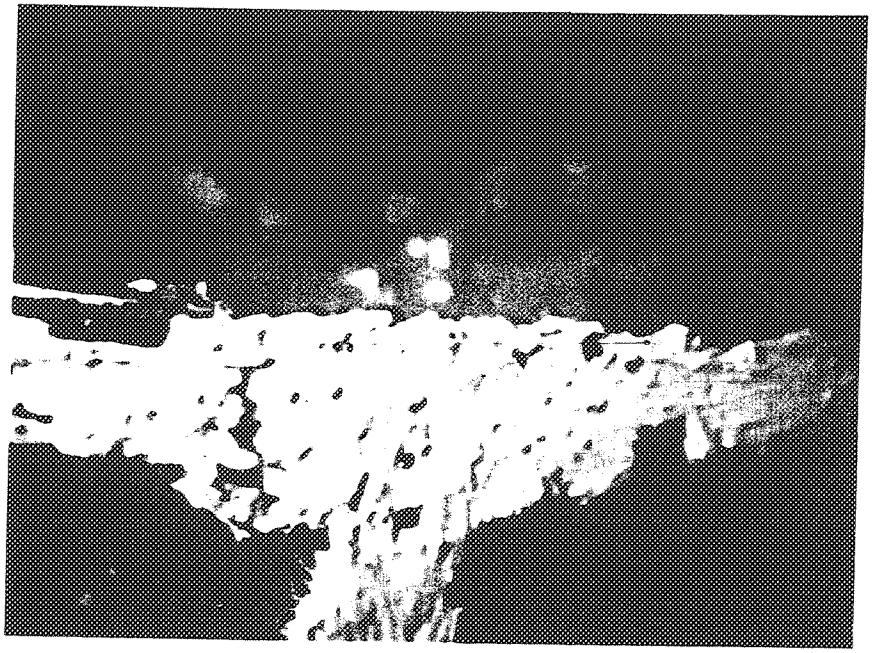

(a)

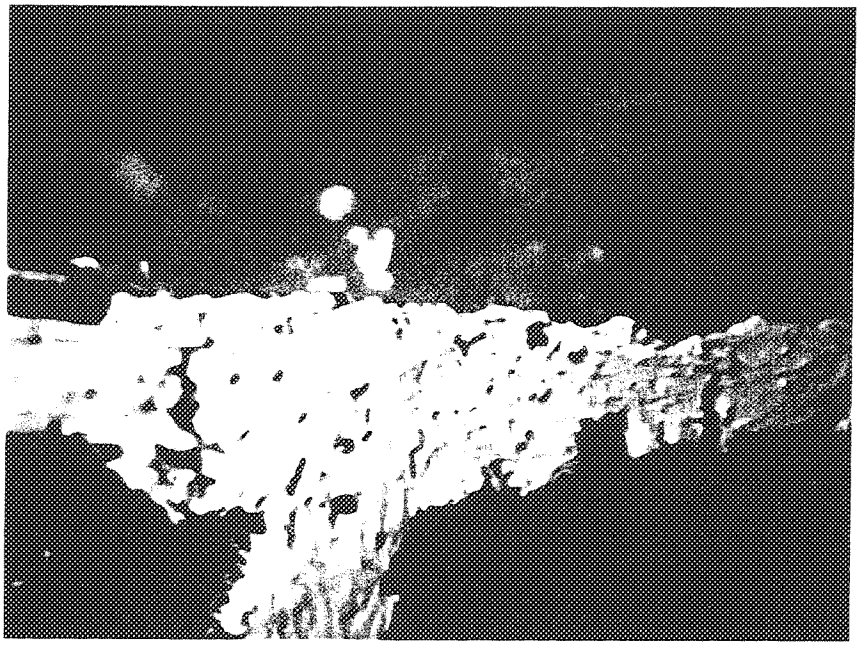

(b)

Figure 47. Bending failure for a B.F. Goodrich 3D SiC/SiC T-joint

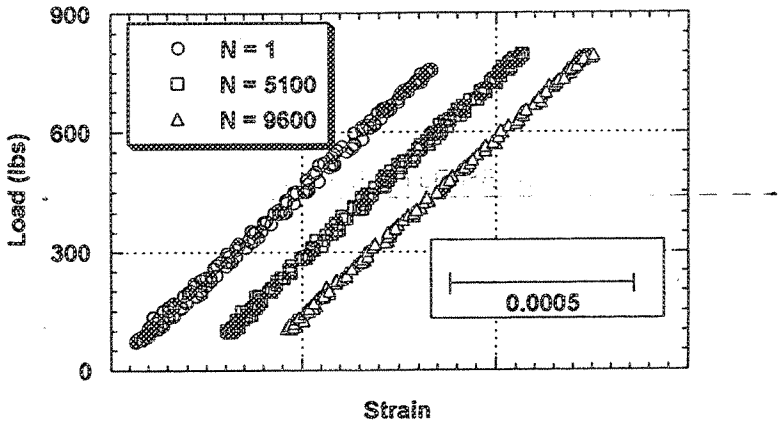

Figure 51. Load vs. strain curves for an Oxide/Oxide-2D notched specimen at various cycles

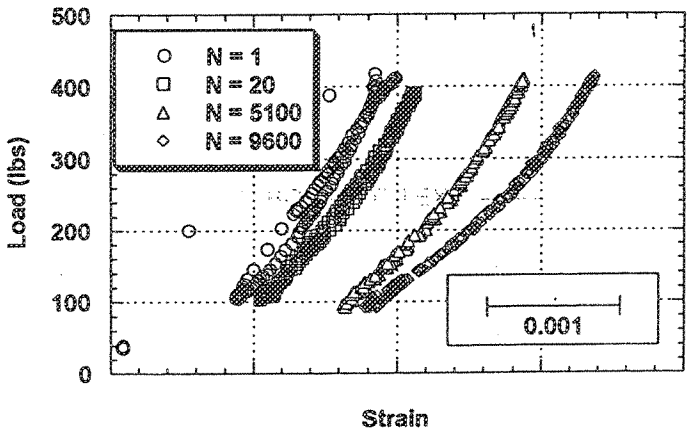

Figure 52. Load vs. strain curves for an Oxide/Oxide-3D notched specimen at various cycles

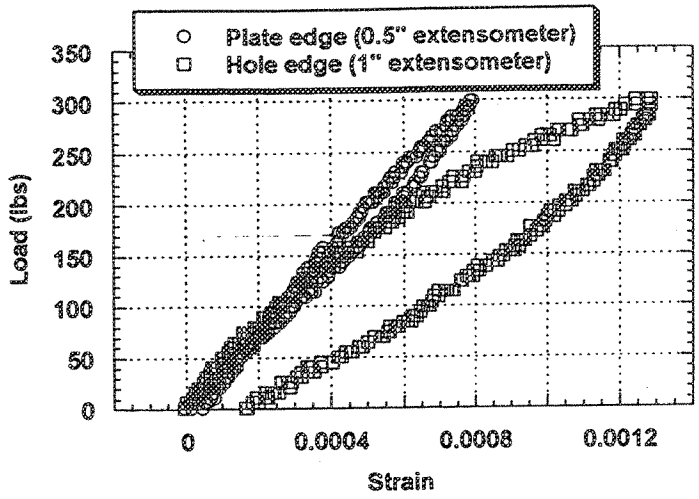

(a)

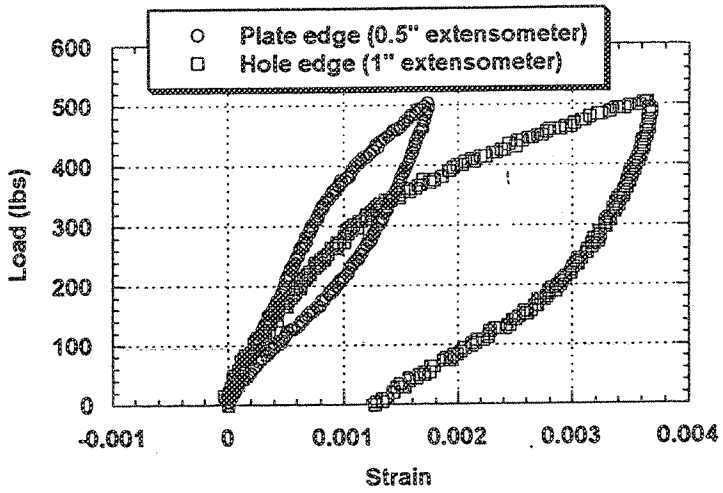

(b)

Figure 53. Load vs. strain curves for an Oxide/Oxide-3D notched specimen
(a) subjected to 300 lbs tensile loading and then unloading
(b) subjected to 500 lbs tensile loading and then unloading

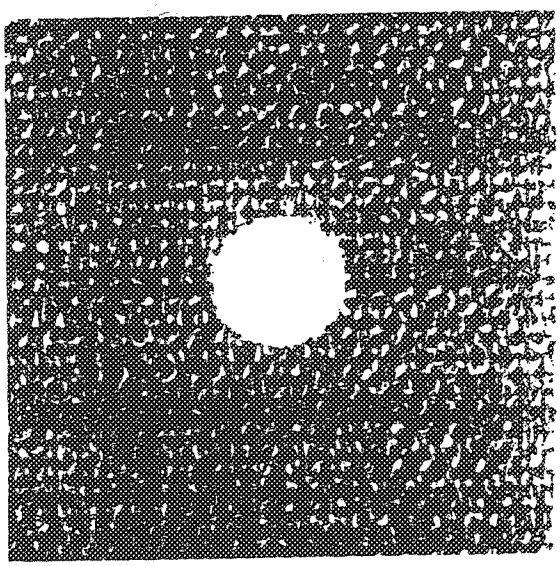

(a)

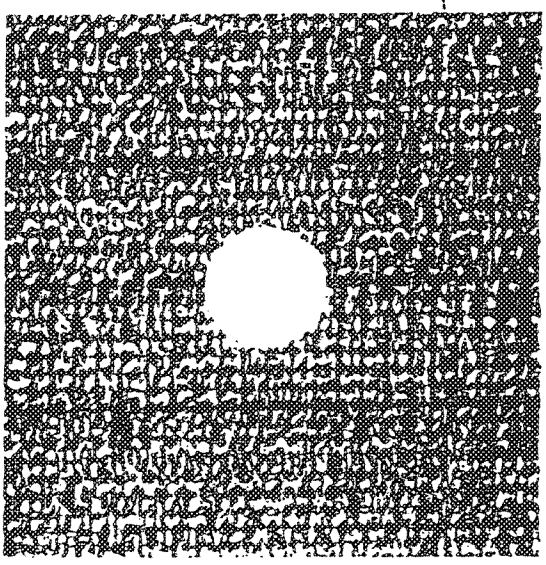

(b)

Figure 54. Penetrant enhanced X-ray photos taken before (a) and after 500 lbs loading (b) for an Oxide/Oxide-3D notched specimen (damage shown as white areas)

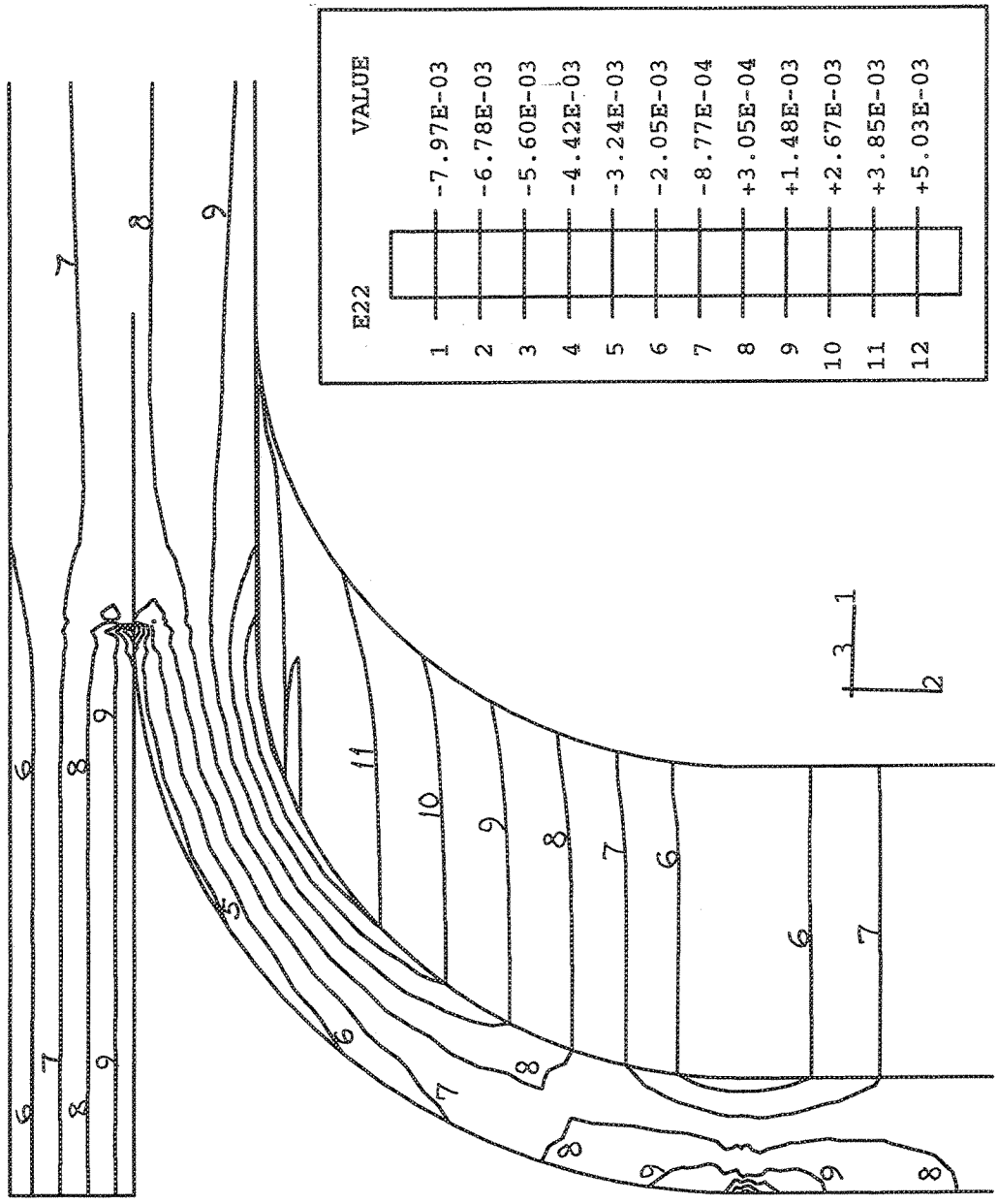

Figure 55. Contour plot of strain distribution in a T-joint without fill-in material when a 0.05 inch vertical displacement was applied to its web section

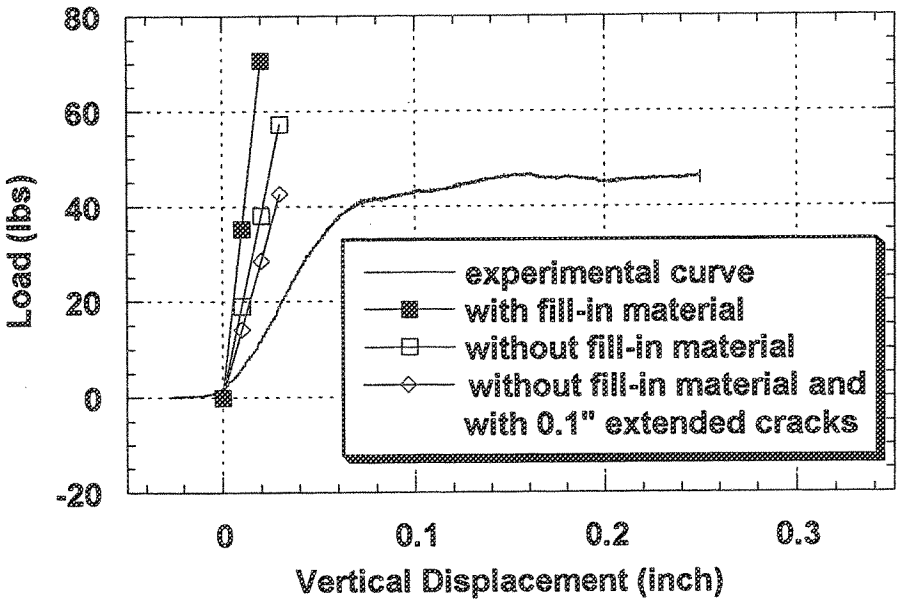

Figure 56. Experimental and numerical results of load-deflection curve for a SiC/SiC 2D T-joint

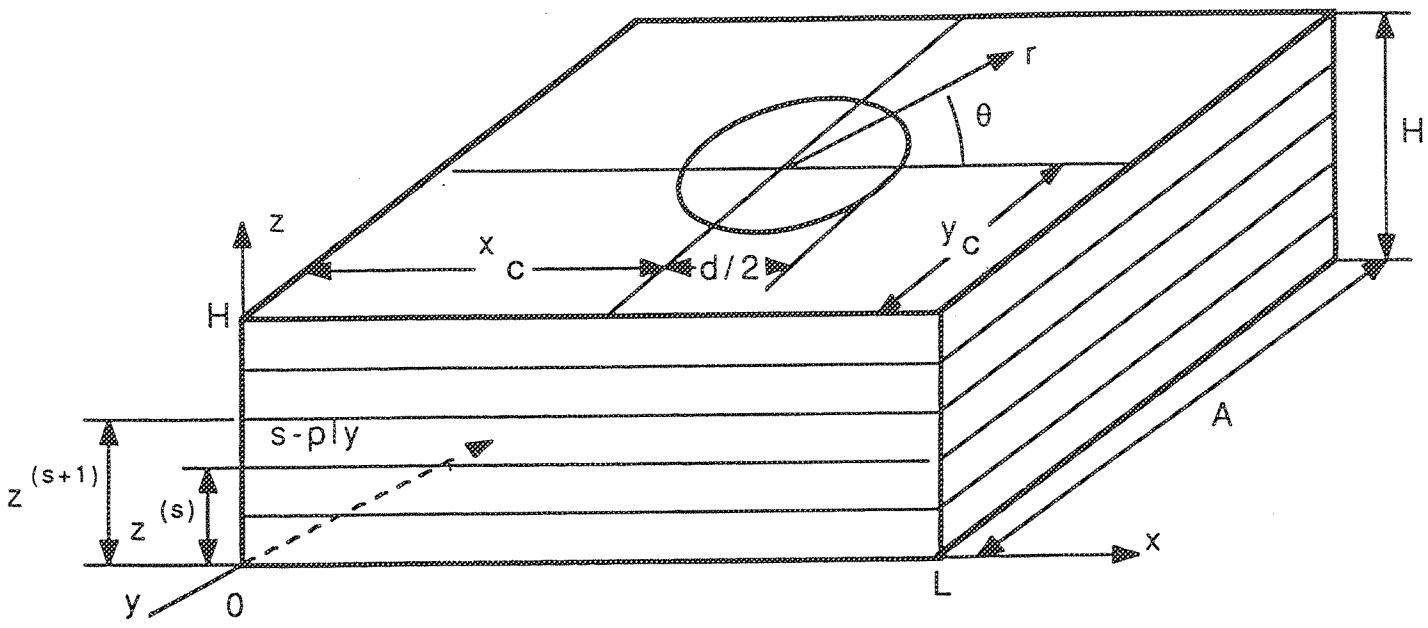

Figure 57. Coordinate axes and laminate notations.

Figure 58. Transformation of coordinates.

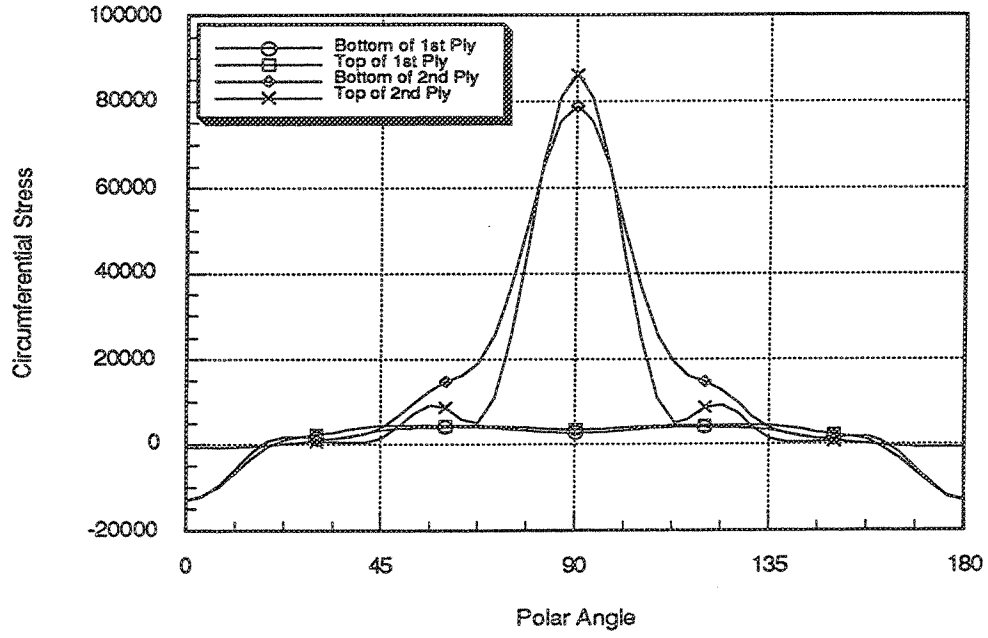

Figure 59. Circumferential Stress $\sigma_{\theta\theta}$ in each ply at the hole of the $[0/90]_s$ laminate.

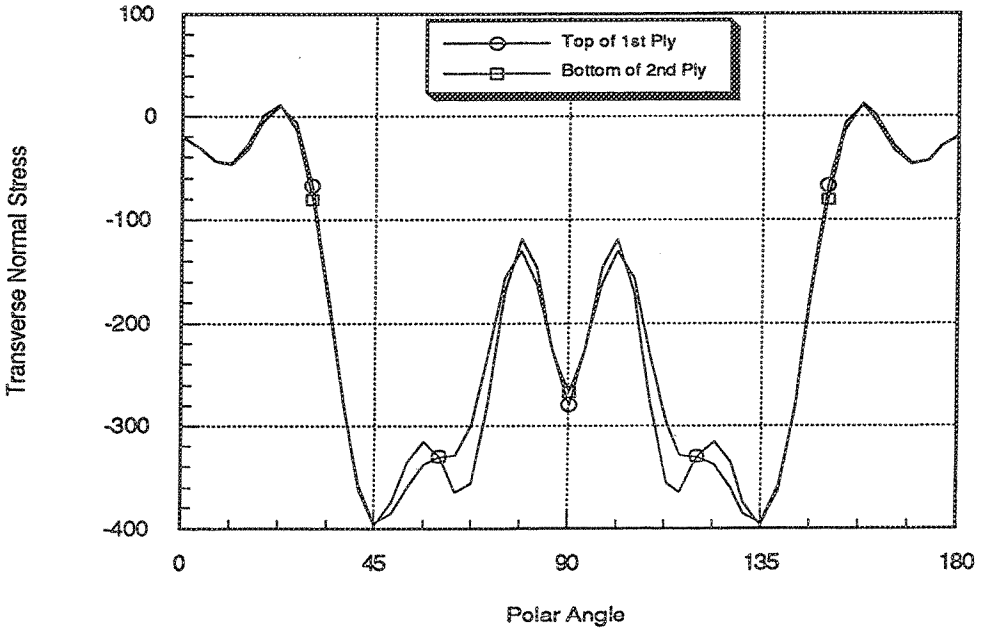

Figure 60. Transverse Normal Stress σ_{zz} at two interfaces of the $[0/90]_s$ laminate at hole boundary.

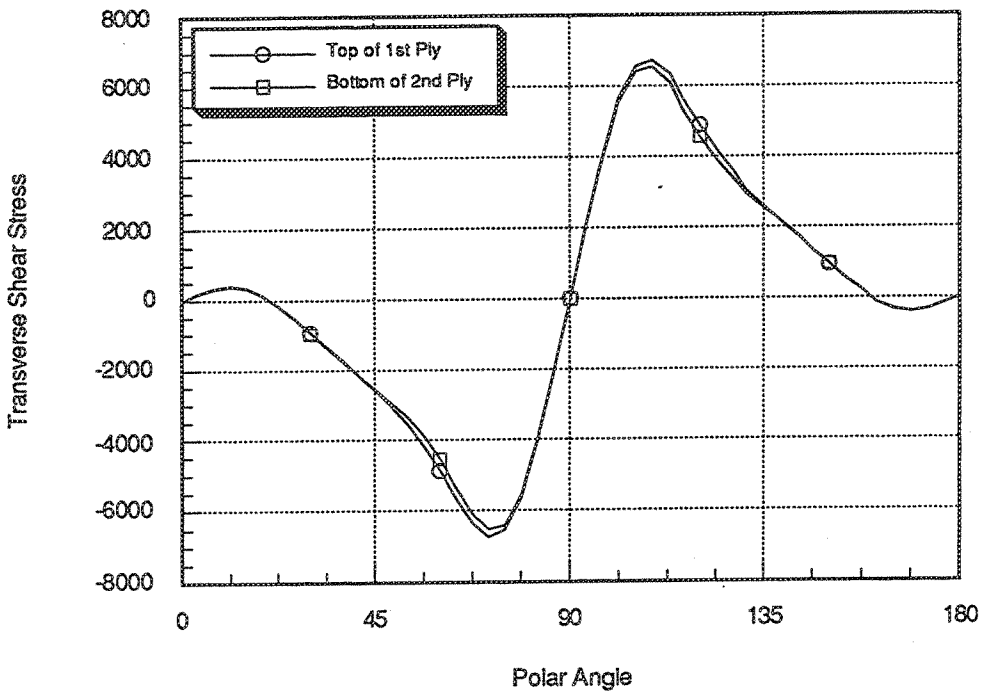

Figure 61. Interlaminar shear stress $\tau_{\theta z}$ at two interfaces of the [0/90]$_s$ laminate.

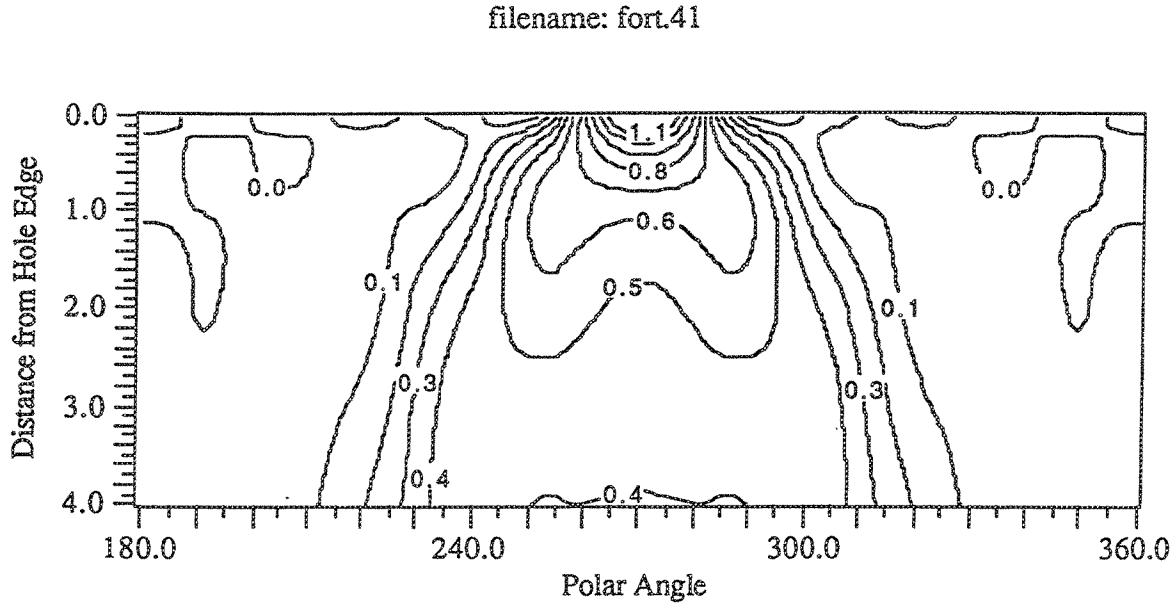

Fig. 62a. Maximum σ_{11}/X , Top of the 2nd layer (0°) of the [0/90]$_s$ laminate. Load value is 200 lb.

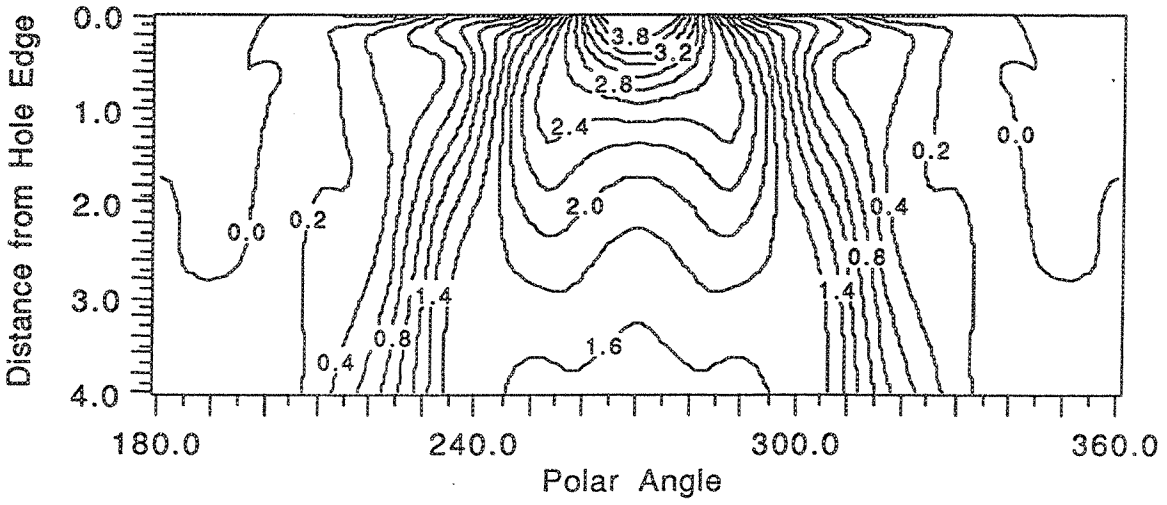

Fig 62b. Maximum σ_{22}/Y , Top of the 1st layer (90°) of the [0/90]$_s$ laminate. Load value is 200 lb.

filename: fort.13

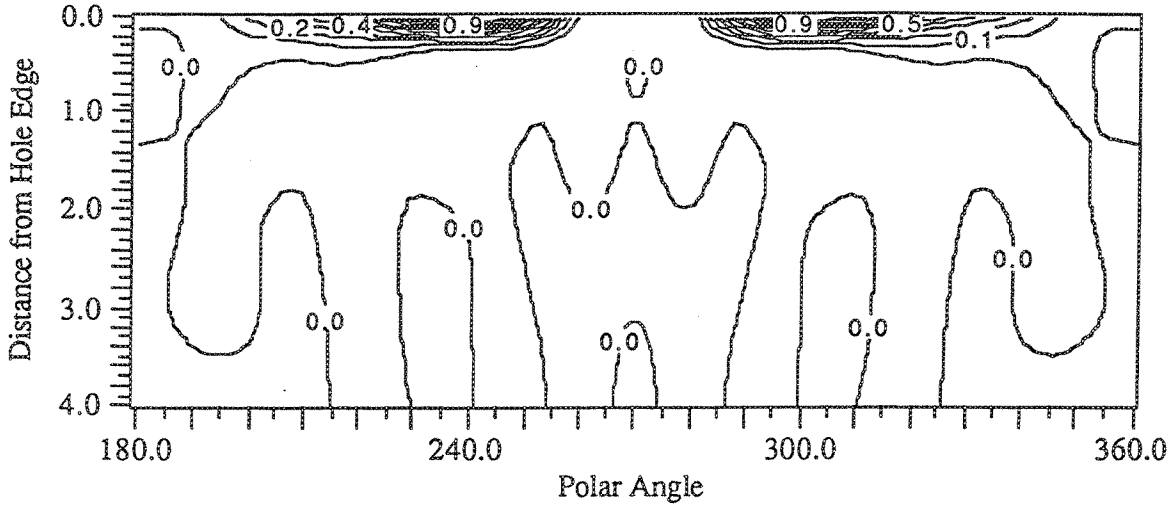

Fig. 63a. Maximum σ_{33}/Y, Bottom of the 1st layer (90°) of the [0/90]$_s$ laminate. Load value is 200 lb.

filename: fort.24

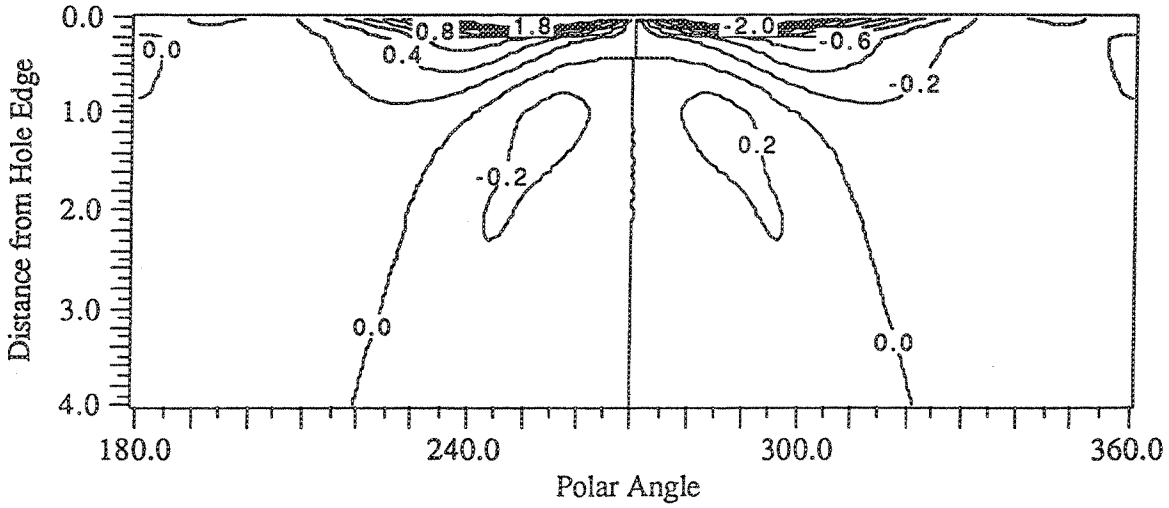

Fig. 63b. Min & Max σ_{23}/S , Top of the 1st layer (90°) of the [0/90]$_s$ laminate. Load value is 200 lb.

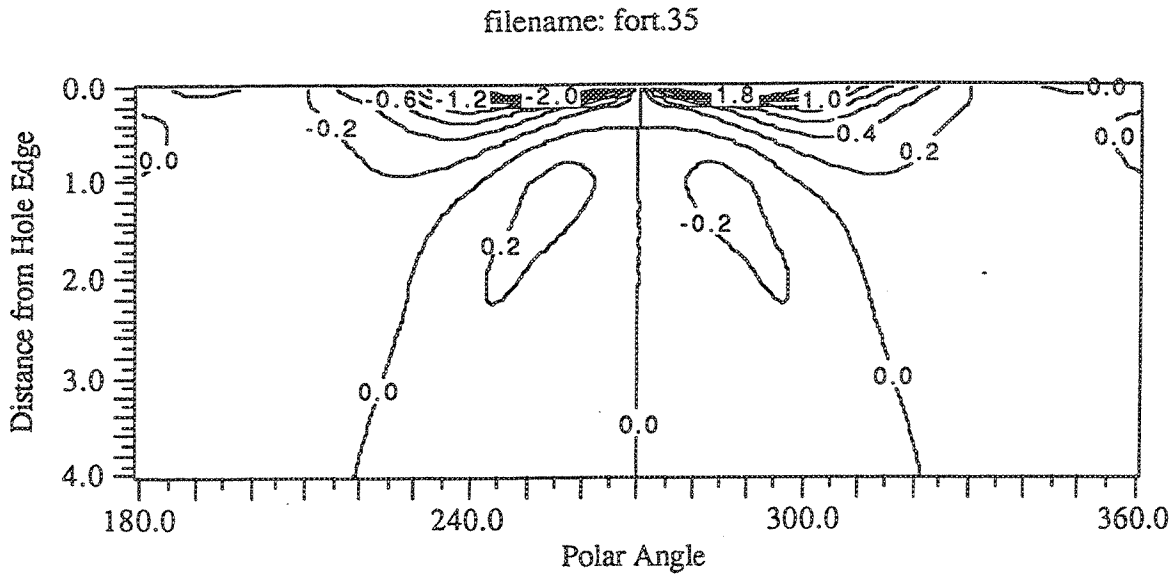

Figure 64a. Min & Max σ_{12}/S, bottom of the second layer (0°) of the $[0/90]_s$ laminate. Load value is 200 lb.

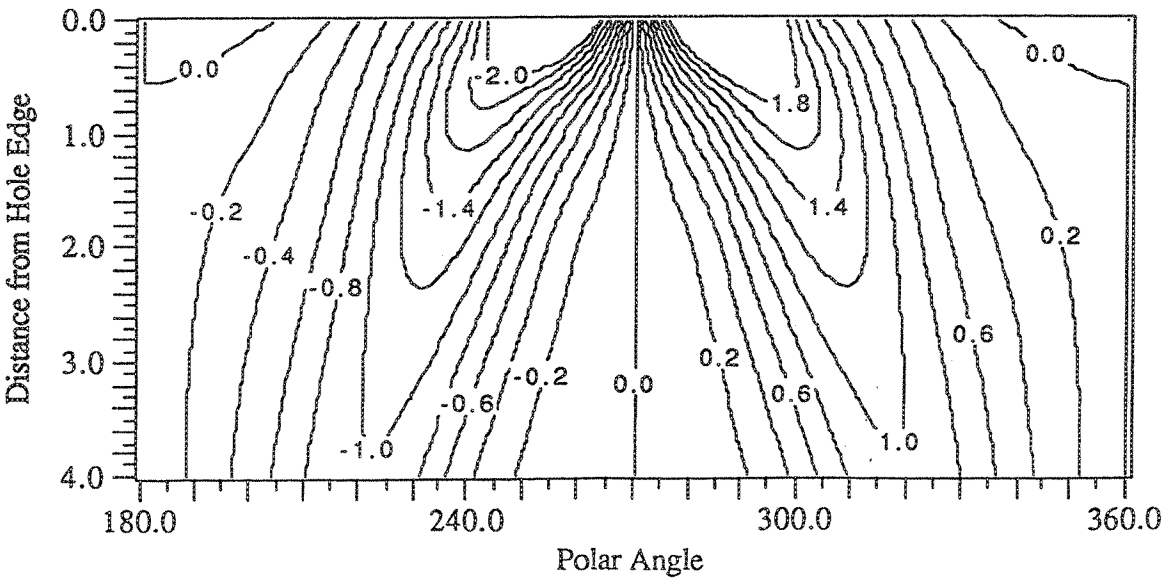

Figure 64b. Minimum σ_{12}/S, top of the second layer (0°) of the $[0/90]_s$ laminate. Load value is 200 lb.

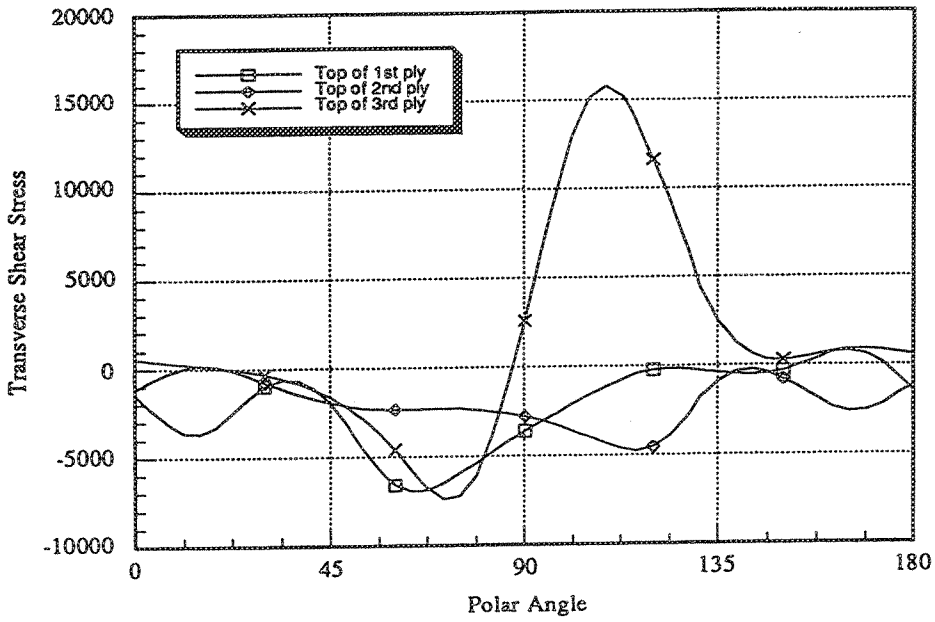

Figure 67. Interlaminar shear stress $\tau_{\theta z}$ at each interfaces of the [0/45/90/-45], laminate.

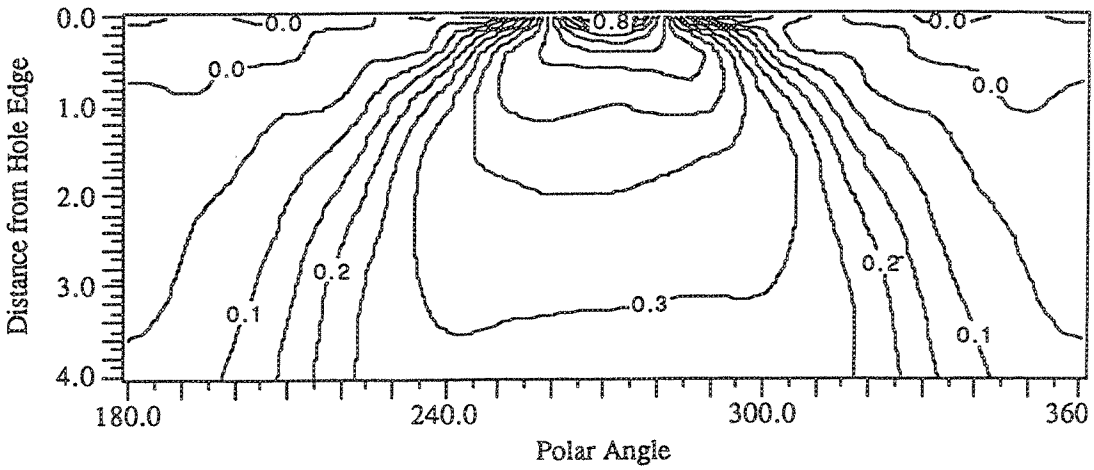

Figure 68a. Maximum σ_{11}/X_t, top of the fourth layer (0°) of the $[0/45/90/-45]_s$ laminate. Load value is 250 lb.

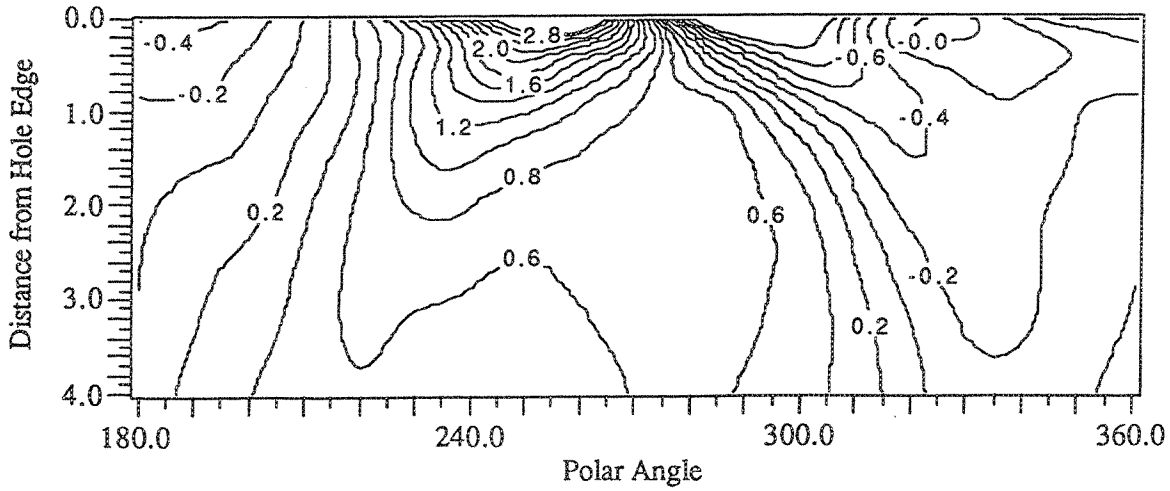

Figure 68b. Maximum σ_{22}/Y_t, top of the third layer (45°) of the $[0/45/90/-45]_s$ laminate. Load value is 250 lb.

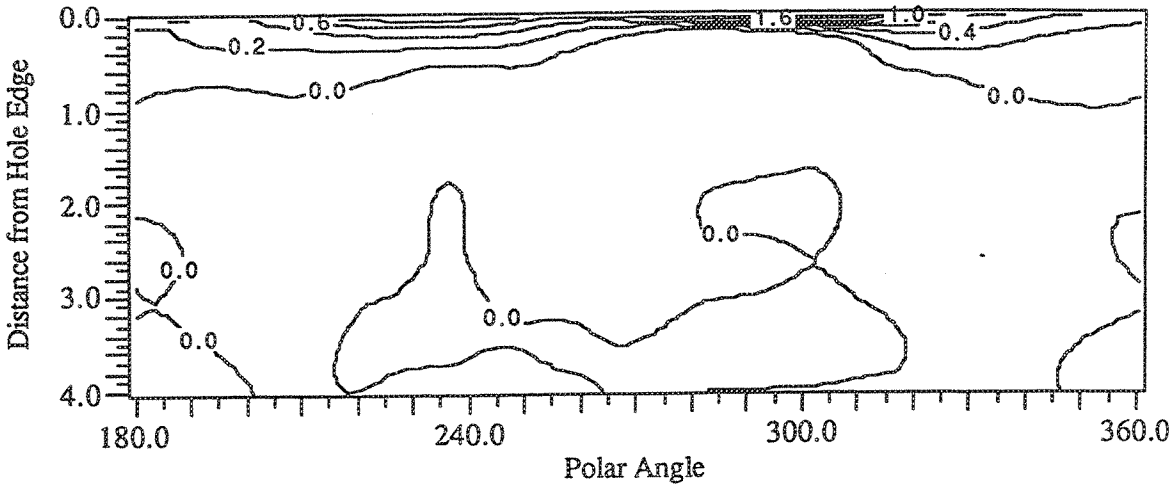

Figure 69a. Maximum σ_{33}/Y_t, top of the second layer (90°) of the $[0/45/90/-45]_s$ laminate. Load value is 250 lb.

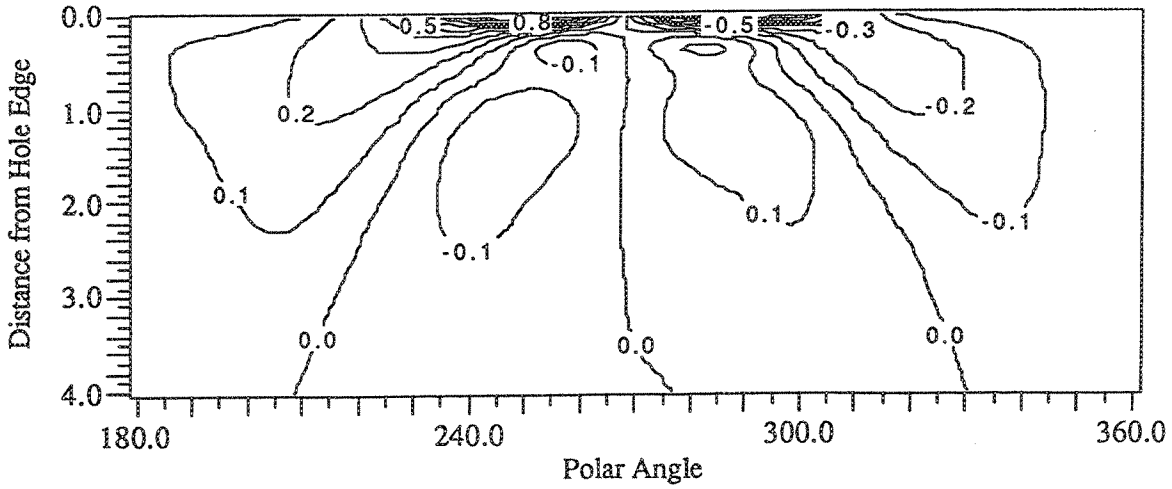

Figure 69b. Minimum σ_{23}/S_t, top of the third layer (45°) of the $[0/45/90/-45]_s$ laminate. 50 lb. Load value is 250 lb.

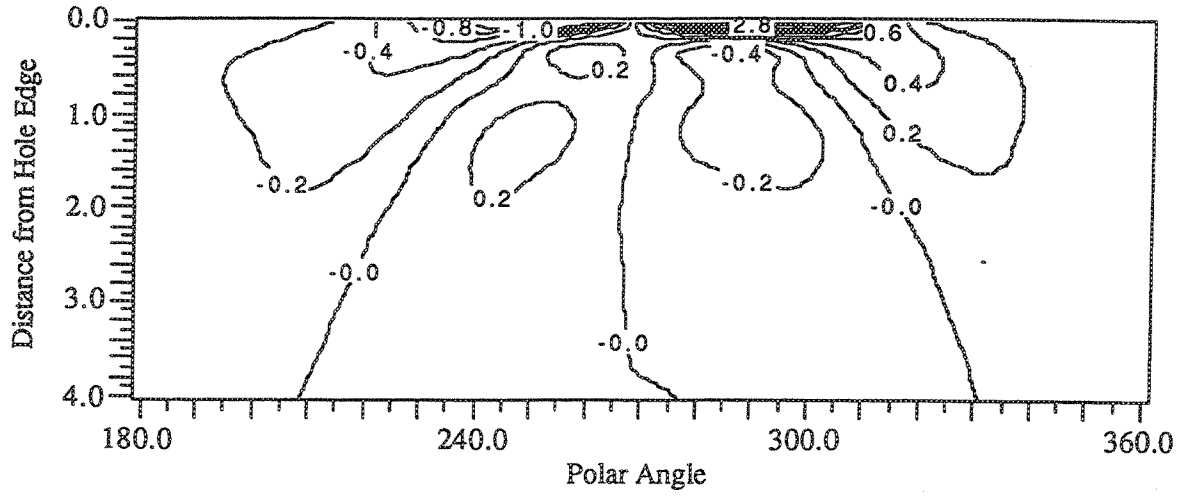

Figure 70a. Maximum σ_{13}/y_t, bottom of the fourth layer (0°) of the $[0/45/90/-45]_s$ laminate. Load value is 250 lb.

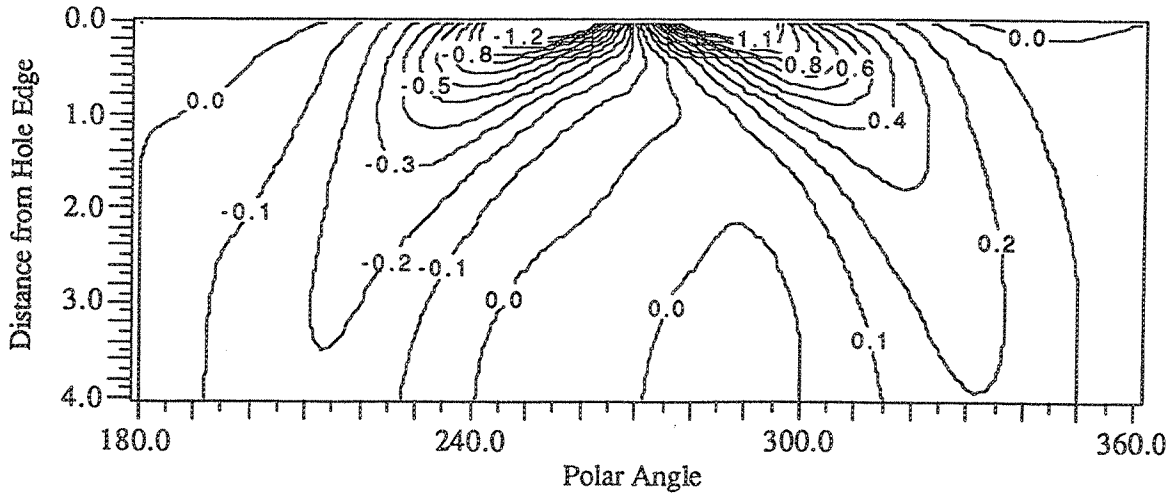

Figure 70b. Min & Max σ_{12}/S_t, top of the fourth layer (0°) of the $[0/45/90/-45]_s$ laminate. Load value is 250 lb.

REPORT DOCUMENTATION PAGE

Form Approved
OMB No. 0704-0188

1. AGENCY USE ONLY (*Leave blank*)	2. REPORT DATE	3. REPORT TYPE AND DATES COVERED
	January 2005	Final Contractor Report

4. TITLE AND SUBTITLE

Damage Prediction Models for Advanced Materials and Composites

5. FUNDING NUMBERS

WBS–22–714–09–46
NAS3–27152

6. AUTHOR(S)

Ming Xie and Jalees Ahmad

7. PERFORMING ORGANIZATION NAME(S) AND ADDRESS(ES)

AdTech Systems Research, Inc.
1342 N. Fairfield Road
Beavercreek, Ohio 45432

8. PERFORMING ORGANIZATION REPORT NUMBER

E–14787

9. SPONSORING/MONITORING AGENCY NAME(S) AND ADDRESS(ES)

National Aeronautics and Space Administration
Washington, DC 20546–0001

10. SPONSORING/MONITORING AGENCY REPORT NUMBER

NASA CR—2005-213327

11. SUPPLEMENTARY NOTES

This research was originally published internally as HSR058 in August 1997. Ming Xie, AdTech Systems Research, Inc., Beavercreek, Ohio 45432–2698; and Jalees Ahmad, Research Applications, Inc., Centerville, Ohio 45459. Project Manager, Joseph E. Grady, Aeronautics Directorate, NASA Glenn Research Center, organization code PRV, 216–433–6728. Responsible person, Diane Chapman, Ultra-Efficient Engine Technology Program Office, NASA Glenn Research Center, organization code PA, 216–433–2309.

12a. DISTRIBUTION/AVAILABILITY STATEMENT

Unclassified - Unlimited
Subject Categories: 01, 05, and 07 Distribution: Nonstandard

Available electronically at http://gltrs.grc.nasa.gov

This publication is available from the NASA Center for AeroSpace Information, 301–621–0390.

12b. DISTRIBUTION CODE

13. ABSTRACT ***(Maximum 200 words)***

In the present study, the assessment and evaluation of various acoustic tile designs were conducted using three-dimensional finite element analysis, which included static analysis, thermal analysis and modal analysis of integral and non-integral tile design options. Various benchmark specimens for acoustic tile designs, including CMC integral T-joint and notched CMC plate, were tested in both room and elevated temperature environment. Various candidate ceramic matrix composite materials were used in the numerical modeling and experimental study. The research effort in this program evolved from numerical modeling and concept design to a combined numerical analysis and experimental study. Many subjects associated with the design and performance of the acoustic tile in jet engine exhaust nozzle have been investigated.

14. SUBJECT TERMS

Ceramic matrix composites; Acoustic tile; Exhaust nozzle

15. NUMBER OF PAGES

99

16. PRICE CODE

17. SECURITY CLASSIFICATION OF REPORT	18. SECURITY CLASSIFICATION OF THIS PAGE	19. SECURITY CLASSIFICATION OF ABSTRACT	20. LIMITATION OF ABSTRACT
Unclassified	Unclassified	Unclassified	